QUANTUM FREQUENCY COMBS AND THEIR APPLICATIONS IN QUANTUM INFORMATION PROCESSING

A Dissertation

Submitted to the Faculty

of

Purdue University

by

Poolad Imany

In Partial Fulfillment of the

Requirements for the Degree

of

Doctor of Philosophy

May 2019

Purdue University

West Lafayette, Indiana

THE PURDUE UNIVERSITY GRADUATE SCHOOL
STATEMENT OF DISSERTATION APPROVAL

Prof. Andrew M. Weiner, Chair
Department of Electrical and Computer Engineering

Prof. Minghao Qi
Department of Electrical and Computer Engineering

Prof. Daniel S. Elliott
Department of Electrical and Computer Engineering

Prof. Peter Bermel
Department of Electrical and Computer Engineering

Approved by:

Dr. Pedro Irazoqui
Head of the School Graduate Program

I dedicate this dissertation to my mother and father, Shohreh and Mohammadtaghi, who dedicated their lives to my happiness.

ACKNOWLEDGMENTS

There are many people I want to thank for making my graduate studies such an outstanding experience:

First and foremost, I want to thank my family for encouraging me every step of the way. My mother, Shohreh, my father, Mohammadtaghi, and my sister, Ara. I would not have been able to focus on chasing my dreams without your full support, care, and everyday phone calls. I would also like to thank my Aunt, Azadeh, and cousin, Raha for always helping me to feel supported.

Shortly after, I would like to thank my advisor, Prof. Andrew Weiner. I have learned many things from you in the past five and a half years. I have learned how to organize my ideas, how to pay attention to every small detail, and how to treat people with respect. I thank you with my whole heart for creating such a healthy and nurturing environment for me to do research in and prosper. One thing I could no learn from you is how you multiply and divide big numbers off the top of your head in a fraction of a second, and I will always envy you for that!

I would also like to thank other group members of the Ultrafast Optics lab. I would like to give a special thanks Dr. Jose Jaramillo-Villegas, Dr. Ogaga Odele, and Dr. Joseph Lukens, for I have learned many valuable things from them. I would also like to thank Dr. Daniel Leaird, Dr. Andrew Metcalf, Dr. Xiaoxiao Xue, Dr. Pei-Hsun Wang, Dr. Yang Liu, Dr. Yihan Li, Dr. Chengying Bao, Dr. Bohao Liu, Oscar Sandoval, Mohammed Alshaykh, Keith McKinzie, Cong Wang, Abdullah Al Noman Ovi, Hsuan-Hao (Peach) Lu, Nathan O'Malley, Navin Lingaraju, Alexandria Moore, and Suparna Seshadri.

I would also like to thank my friends, who never stopped energizing me. I would like to thank Allison Rice, Kia Khezeli, Babak Yazdanpanah, Rouzbeh Kananizadeh, Omid Javidbakht, Kasra Ghaemi, Shiva Piltan, Sina Miran, Hamid Nadjafi, Nima

Darivandpour, Hadi Shagerdi, Amir Sadeghi, Ali Hekmatfar, Mahsa Fardisi, Samaneh Saadat, Siamak Rabiei, Ali Razavieh, Farzin Shamloo and Mohammed Aboelnour.

Last but not least, I would like to thank the members of my Ph.D. committee, Prof. Minghao Qi, Prof. Daniel Elliott, and Prof. Peter Bermel for their valuable comments on my dissertation.

TABLE OF CONTENTS

Page

LIST OF TABLES

LIST OF FIGURES

Figure Page

ABBREVIATIONS

BFC	biphoton frequency comb
BME	Bayesian mean estimation
CAR	coincidence to accidental ratio
CFBG	chirped fiber Bragg grating
CINC	controlled-increment
CW	continuous wave
DoF	degree of freedom
DWDM	dense wavelength division multiplexing
FSR	free spectral range
FWHM	full width at half maximum
FWM	four-wave mixing
HOM	Hong-Ou-Mandel
JSI	joint spectral intensity
MLE	maximum likelihood estimation
MRR	microring resonator
MZI	Mach-Zehnder interferometer
MZM	Mach-Zehnder modulator
OSA	optical spectrum analyzer
PM	phase modulator
PPLN	periodically poled Lithium Niobate
QIP	quantum information processing
QKD	quantum key distribution
rf	radio frequency
SMF	single mode fiber

SPD	single photon detector
SPDC	spontaneous parametric down-conversion
SFWM	spontaneous four-wave mixing
TIA	time interval analyzer

ABSTRACT

Imany, Poolad Ph.D., Purdue University, May 2019. Quantum Frequency Combs and Their Applications in Quantum Information Processing. Major Professor: Andrew M. Weiner.

We experimentally demonstrate time-frequency entangled photons with comb-like spectra via both bulk optical crystals and on-chip microring resonators and explore their characterization in both time and frequency domain using quantum state manipulation techniques. Our characterization of these quantum frequency combs involves the use of unbalanced Mach-Zehnder interferometers and electro-optic modulators for manipulation in time- and frequency-domain, respectively. By creating indistinguishable superposition states using these techniques, we are able to interfere states from various time- and frequency-bins, consequently proving time- and frequency-bin entanglement. Furthermore, our time-domain manipulations reveal pair-wise continuous time-energy entanglement that spans multiple frequency bins, while our utilization of electro-optic modulators to verify high-dimensional frequency-bin entanglement constitutes the proof of this phenomenon for a spontaneous four-wave mixing process. By doing so, we show the potential of these quantum frequency combs for high-dimensional quantum computing with frequency-encoded quantum states, as well as fully secure quantum communications via quantum key distribution by performing a nonlocal dispersion cancellation experiment. To show the potential of our entangled photons source for encoding quantum information in the frequency domain, we carry out a frequency-domain Hong-Ou-Mandel interference experiment by implementing a frequency beam splitter. Lastly, we use the high-dimensionality of our time-frequency entangled source in both time and frequency domain to implement deterministic high-dimensional controlled quantum gates, with the quantum

information encoded in both the time and frequency degrees of freedom of a single photon. This novel demonstration of deterministic high-dimensional quantum gates paves the way for scalable optical quantum computation, as quantum circuits can be implemented with fewer resources and high success probability using this scheme.

1. INTRODUCTION

Quantum information processing (QIP) has gained massive attention in recent years as it promises to solve some exponentially hard problems in polynomial time through quantum computation [1–3], as well as having other unique capabilities such as fully secure communications through quantum key distribution (QKD) [4,5], and enhanced sensing through quantum metrology [6]. To perform these nonclassical operations, quantum entanglement plays a key role. Entangled particles are a pair of particles that show correlations in a way that classical mechanics fails to explain; the states of the particles are joint such that the outcome of a measurement on one of the particles can instantaneously predict the result of a measurement on its partner particle. Amongst many platforms that entanglement can be created in, photonic states draw a great deal of attention due to their ability to maintain coherence over a long time, and their aptitude for communications. In this Thesis, we focus on showing the potential of quantum states of light for these quantum operations.

Typical QIP systems are based on two-level quantum states, also called qubits. To simplify the complexity of quantum circuits [7, 8] and increase the practicality of quantum computation, high-dimensional entangled states (entangled qudits) are strong candidates as a result of their robustness and stronger immunity to noise, compared to two-dimensional systems [9–12]. In photonics, many degrees of freedom have the potential to exhibit high-dimensionality (time, frequency, spatial, orbital angular momentum). Here, we focus on time and frequency degrees of freedom, where the states can easily be generalized to higher dimensions. We use integrated and bulk platforms to create time-frequency (time-energy) entangled photons with a comb-like spectrum and show the potential of these platforms for time and frequency encoding of information. The bulk platform is faced with the drawback of low scalability and high cost; therefore, our main focus is on integrated optical microresonators which

offer a solution that is highly scalable, low cost and compatible with semiconductor foundries. Now, we look at the potential applications of these sources in more detail.

1.1 Quantum Computing

Quantum computing is one of the most important processes that entangled photons can be used in. By using qubits instead of classical bits of information, some exponentially hard algorithms like factoring can be solved in polynomial time [13–15]. Quantum computing can also be of tremendous help in simulating complex quantum-mechanical systems, such as designing drugs and simulating their effects on human body on a molecular level, a task called quantum simulations which is exponentially hard with classical computers [16]. Right now, building a quantum computer that can solve complex problems that classical computers can not is out of reach, since this requires having multiple qubits and many quantum gates, which are very hard to implement. We show that by using a quantum frequency comb, we can extend the two-dimensional qubits to higher dimensions (qudits), which can potentially reduce the number of required quantum gates to simplify quantum computing protocols [10]. We then show the potential of our source for encoding information in multiple high-dimensional degrees of freedom of a photon by demonstrating, for the first time, two-qudit operations [17],necessary for universal quantum computation with qudits.

1.2 Quantum Communications

Quantum communications promise fully secure communications over a quantum channel, where the presence of an eavesdropper can be revealed by the communicating parties [4] . In these protocols, the two entangled particles are sent to two different parties, who can build a secret key based on their measurement choices. One party (Alice) can later use this key to encode her classical data and send it to the other party (Bob) (Fig 1.1). Since Bob is the only other party with the key, he alone can decode this data, a method called Quantum Key Distribution. Since photons

experience close to no decoherence over time, they are excellent candidates for QKD. It has been shown that using time-frequency entangled photons allows the use of QKD protocols in a high-dimensional way, which enables building more complex codes between the two parties in less time [18]. The applications of these biphotons for quantum computation and QKD shows the potential of these sources to be used in a quantum internet protocol.

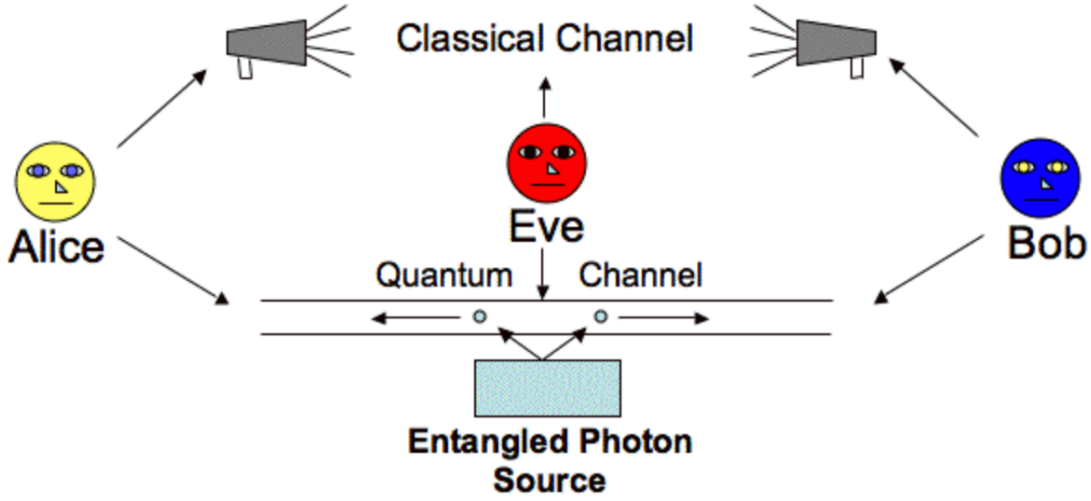

Fig. 1.1. Illustration of quantum key distribution scheme.

1.3 Overview

In this thesis, we first focus on the proof of concept for time and frequency-bin entanglement of the generated biphoton frequency combs [19–21]. Unlike other works done in our laboratory, this work is mainly with quantum frequency combs generated from a silicon nitride microring resonator; a platform that was not explored as a source of entangled photons in our group before these works. We then show the potential of these biphoton frequency combs for quantum information processing in the frequency domain [22]. At last, we demonstrate a scheme for deterministic optical quantum computing using the time and frequency degrees of freedom in a single photon [17].

In chapter 2, we introduce time-frequency entangled photons (biphotons) with a comb-like spectrum along with the different processes and respective platforms we use to generate them in. Chapter 3 focuses on time correlation function of these biphotons that are created in an optical microresonator. In chapter 4, we discuss the time domain manipulation of biphotons through Franson interferometry [19], as well as a dispersion cancellation experiment, showing the potential of our biphotons for large-alphabet QKD [19]. In chapter 5, we show the frequency-bin entanglement of biphotons generated in both integrated and bulk platforms which shows the phase coherence between different comb line pairs and proves their potential for high-dimensional quantum computation [20, 21]. In chapter 6, a fundamental quantum mechanical experiment–namely Hong-Ou-Mandel interference–has been carried out in the frequency domain [22], the first time a frequency-domain Hong-Ou-Mandel has been demonstrated using only linear optical components. In chapter 7, we make use of both the time and frequency degrees of freedom in a single photon to demonstrate elementary high-dimensional deterministic quantum gates [17], the first time high-dimensional controlled quantum gates are demonstrated in not only photonics, but any platform that quantum information processing can take place in.

2. TIME-FREQUENCY ENTANGLED PHOTONS

2.1 Introduction

Time-frequency entangled photons (biphotons) are a pair of photons that are highly correlated with each other in time and energy, namely signal and idler. The signal field is defined as the photon with higher frequency and the idler field is defined as the photon with the lower frequency. Since the creation time of this pair is at the same time, these photons are correlated in time, and because of energy conservation in the creation process, their energies are dependent on each other as well. We use two different processes to create these entangled photons: spontaneous parametric down conversion (SPDC) and spontaneous four-wave mixing (SFWM). In both of these processes, we have a pump beam that shines on a nonlinear material and the photons from the pump beam decay into a pair of entangled photons.

2.2 Spontaneous Parametric Down Conversion

In an SPDC process, one pump photon(∼775 nm) goes through a $\chi^{(2)}$ material [a periodically poled lithium niobate (PPLN) crystal in our case] and decays into a pair of entangled photons(Fig. 2.1) [23]. The setup used to create the biphotons with this process is depicted in Fig. 2.2a, where after the PPLN crystal, free space filters are used to block the pump beam; therefore, only biphotons remain after the filters. The spectrum of the biphoton has a broad bandwidth of ∼40 nm (5 THz), as shown in 2.2b. Since we are interested in biphotons with a comb-like spectrum, we use a commercial pulse shaper as a programmable filter [24] to carve out a frequency comb from this broadband spectrum.

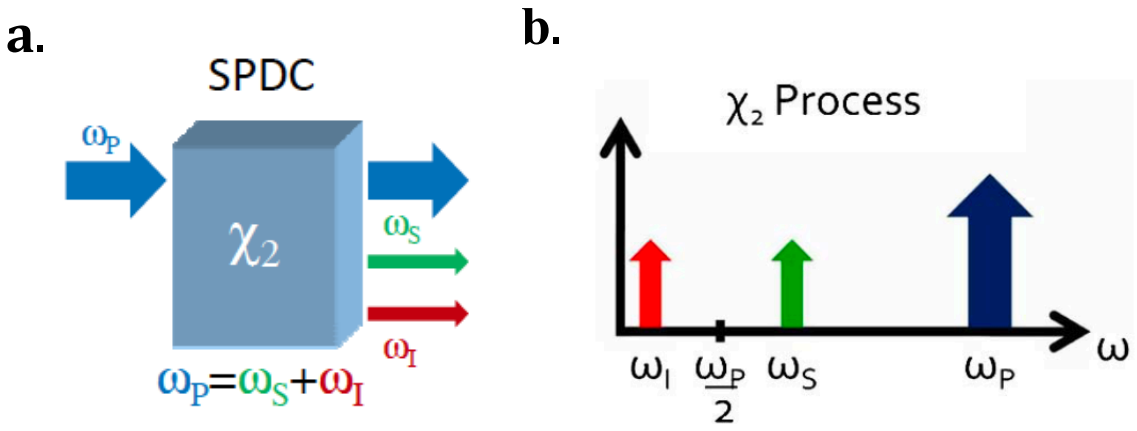

Fig. 2.1. a. SPDC process. b. Illustration of the pump photon and entangled photons in frequency. This figure is adapted from [23].

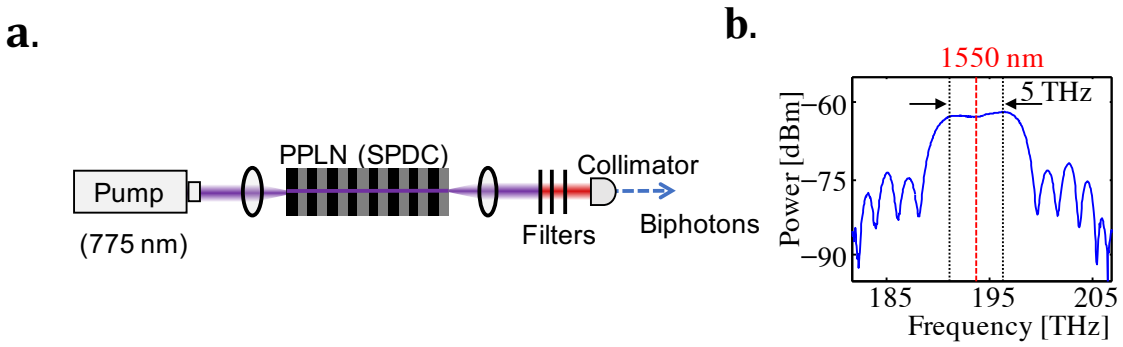

Fig. 2.2. a. Experimental setup for the SPDC process. b. Generated broadband biphoton spectrum for the SPDC process.

2.3 Spontaneous Four-Wave Mixing

In an SFWM process, a $\chi^{(3)}$ material is used [silicon nitride (Si_3N_4) microring resonator in our case], meaning two photons from the pump beam decay into a pair of entangled photons(Fig. 2.3).

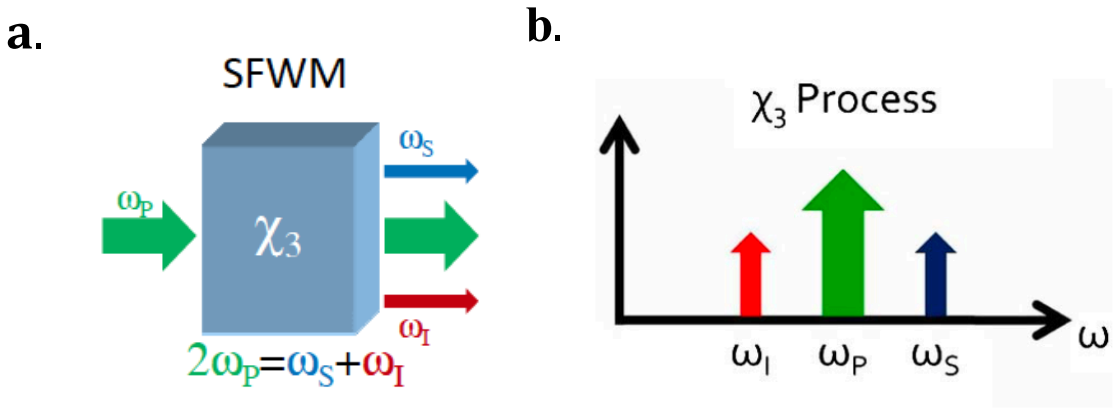

Fig. 2.3. a. SFWM process. b. Illustration of the pump photon and entangled photons in frequency. This figure is adapted from [23].

The simplified setup used to create biphotons from a silicon nitride microring is depicted in 2.4a. Here, we couple a tunable continuous-wave (CW) laser source with a wavelength around 1550 nm to the microring. If the frequency of the CW laser matches with one of the resonances of the microring, it will survive in the ring's cavity and the pump photons will have the chance to decay into entangled photon pairs. Due to the resonant structure of the microring, only certain frequencies spaced by the free spectral range (FSR) survive in the cavity, and due to the photon lifetime in the cavity, each resonance has a linewidth of hundreds of MHz. Hence, this SFWM process leads to the generation of a quantum frequency comb with an FSR and linewidth identical to the properties of the ring (Fig. 2.4b). The comb line in the middle is the pump line, attenuated by ∼60 dB using dense wavelength division multiplexing(DWDM) filters.

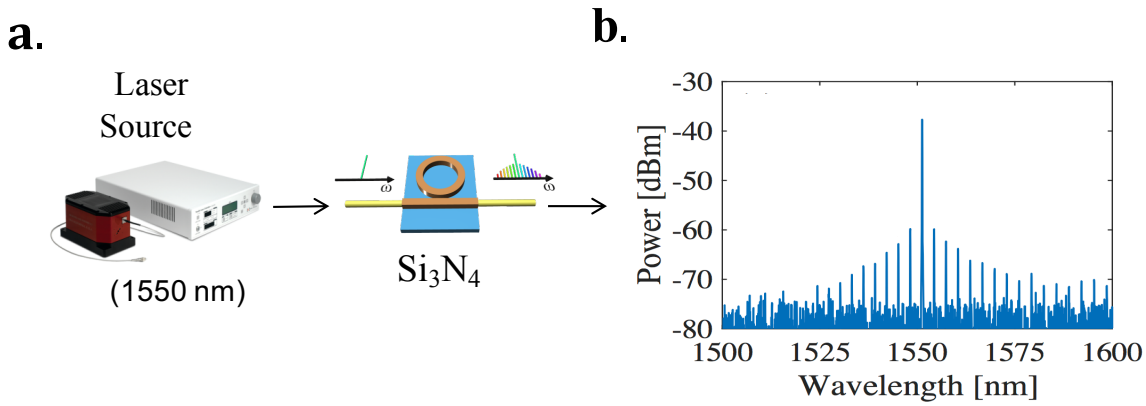

Fig. 2.4. a. Experimental setup for the SFWM process. b. Generated comb-like biphoton spectrum for the SFWM process. This spectrum was measured with the microring with 380 GHz FSR (∼3 nm), which is the spacing between the comb lines in this figure.

2.4 Theory

Throughout both of these processes, energy has to be conserved which for photons, it directly translates into a frequency dependence between the biphoton pair if the frequency of the pump photons are known. The entangled photons with these comb-like spectrums are also called a quantum frequency comb, or biphoton frequency comb (BFC). Generally, a BFC state can be written as:

$$|\Psi\rangle = \sum_{k=1}^{N} \alpha_k \, |k,k\rangle_{SI}, \tag{2.1}$$

with

$$|k,k\rangle_{SI} = \int d\Omega \, \Phi(\Omega - k\Delta\omega) \, |\omega_0 + \Omega, \omega_0 - \Omega\rangle_{SI} \tag{2.2}$$

where $|k,k\rangle_{SI}$ represents the signal and idler photons from the k^{th} comb line pair, α_k is a complex number describing the amplitude and phase of the k^{th} comb line pair and N is the total number of mode pairs, $\Phi(\Omega)$ is the lineshape function and $\Delta\omega$ is the FSR. ω_0 is the pump frequency for a SFWM process and half the pump

frequency for an SPDC process. The coherent superposition of states implied by Eq. 2.1 requires phase coherence between the frequency mode pairs, meaning the relative phases between different comb line pairs are fixed and not random. This phase coherence is identical to frequency-bin entanglement between these comb line pairs.

3. QUANTUM FREQUENCY COMBS IN AN OPTICAL MICRORESONATOR

3.1 Background

To generate a BFC from an optical microresonator, we have to seed it with a laser with low enough power to operate the microresonator under threshold. If the power of the CW laser is higher than a certain threshold, we reach the classical comb generation regime, where each comb line generated from the pump is strong enough to undergo the Four-Wave Mixing (FWM) process again and generate entangled photons of its own. Since we are interested in biphotons that are energy matched with respect to the pump line, we want the FWM process from the other comb lines to be negligible compared to that of the pump. This way, we are also making sure that the power in each comb line is low enough to operate in the entanglement regime, which we talk about in more detail in the next section.

We use two different microring resonators to generate our BFCs for different experiments. The first one, used for the time domain measurements and quantum gating experiments, has a 380 GHz FSR, ∼270 MHz linewidth and a loaded quality factor of $Q_L = 7.2 \times 10^5$ (Fig. 3.1a). The second microresonator is considerably larger, has an FSR of ∼50 GHz, a linewidth of ∼100 MHz and its $Q_L = 2 \times 10^6$ Fig. 3.1b. We use the second microring in the frequency domain processing of the BFC because of the lower frequency spacing between comb lines, thereby making it easier to mix comb lines in frequency using linear-optical techniques. We characterize both of these microrings through measurements of time correlations between different comb line pairs [19, 21].

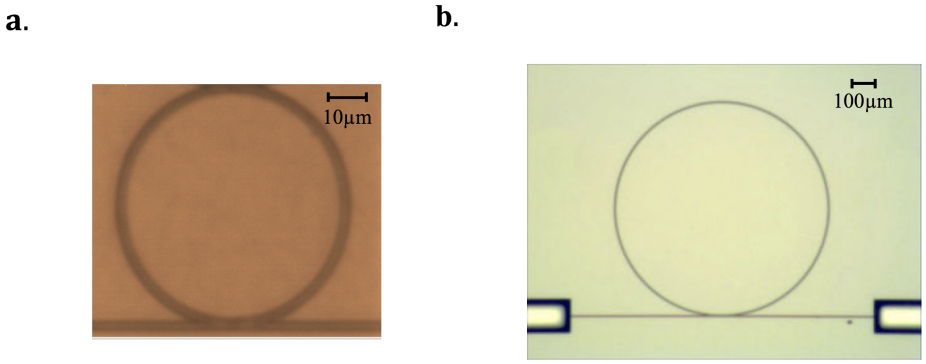

Fig. 3.1. Pictures of the microrings with a. 380 GHz FSR and b. 50 GHz FSR. Since bigger microrings have smaller FSRs, the microring with a 380 GHz FSR has a factor of 7.6 smaller radius than the microring with a 50 GHz FSR.

3.2 Time Correlations

To characterize the BFC's time correlations, we first use the ring with 380 GHz FSR. Using a pump power of 160 mW, we obtain the spectrum shown in Fig. 3.2a for the BFC using an optical spectrum analyzer (OSA). By using these DWDMs, we separate the strong pump from the other comb lines of the BFC and route them to a different fiber output.In Fig. 3.2a, we also observe a roll-off in the power of the sidebands as we move away from the pump frequency. This is due to the dispersion of the microring which causes the FSR to vary throughout the spectrum. This reduces the overlap of the energy-matched resonances as we move away from the central frequency. To measure this dispersion, the microring was characterized through a transmission spectrum measurement. The wavelength of the tunable CW laser was swept over the lightwave C-band, from 1520 to 1570 nm, while a power meter and wavelength meter (HighFinesse WS6-100) recorded the transmitted power and the current wavelength with 10 MHz resolution, respectively. We measured a free spectral range of 380 GHz (equivalent to $\sim$ 3 nm), a dispersion parameter D of $-57ps/(nm.km)$ (indicating normal dispersion), and an intrinsic quality factor Q_i of 1.12×10^6 of the resonance located at 1550.9 nm. Figure 3.2b shows the frequency

differences between the resonances used to generate signal sidebands and the pump resonance (blue curves); the corresponding frequency differences between idlers and pump are shown as the red curves. The progressive frequency mismatch explains the reduction in photon pair flux for resonances farther away from the pump.

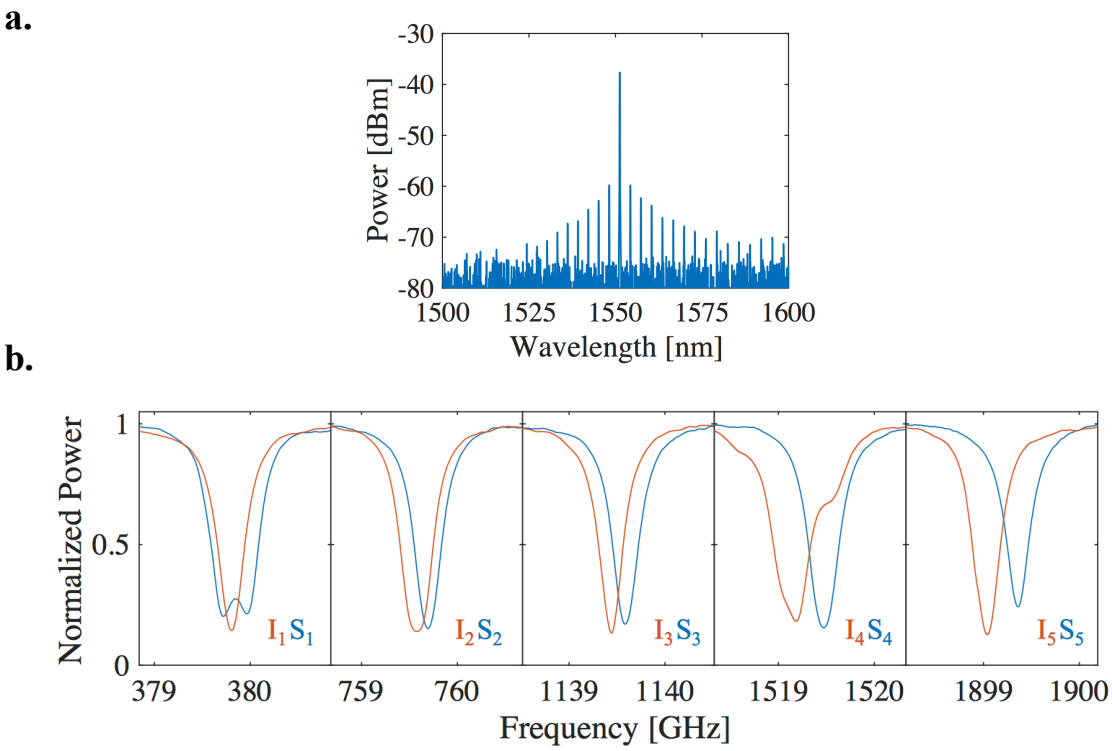

Fig. 3.2. a. BFC spectrum. b. Transmission spectra of resonances corresponding to signal 1 to 5, S_{1-5}, and idler 1 to 5, I_{1-5}. The horizontal axes correspond to the absolute frequency difference between the displayed resonances and the central frequency of the pump resonance.

Now, to verify the correlations of our comb-like photon pairs, we first select the signal and idler photons of the 2nd sideband pair (S_2I_2) with the two DWDM filters (Fig. 3.3). Using a pair of Single-Photon Detectors (SPDs) along with a Time Interval Analyzer (TIA), we record the relative arrival time between signal and idler photons as coincidences.

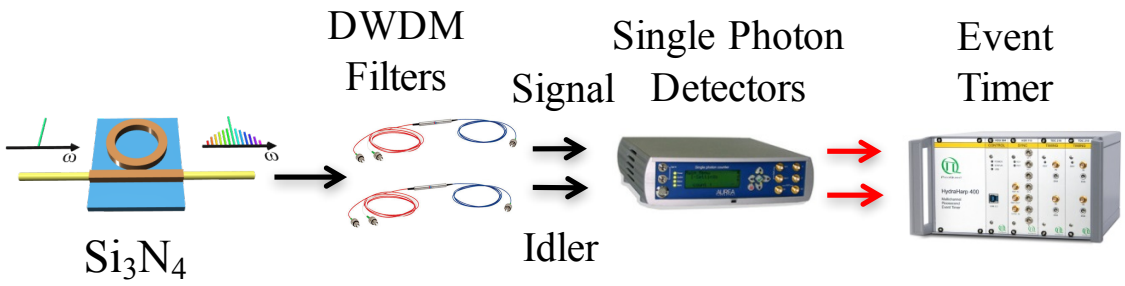

Fig. 3.3. Experimental setup to measure the time correlations between the signal and idler comb lines.

In this process, some accidental events are also registered as a result of detecting background (uncorrelated) photons—any event that is not due to a signal and idler from the same photon-pair is considered an accidental (dark counts, signal and idler from different pairs, or any such combination). Figure 3.4a shows the measured coincidences (accidentals were not subtracted); the sharp peak with a full width at half maximum (FWHM) of ~ 600 ps corresponds to the temporal correlation. This is in agreement with the expected correlation time which is calculated from the inverse of the resonance linewidth ($\sim 2\pi \times 270$ MHz). Furthermore, to show correlations exist only between energy-matched frequencies, we measured the coincidences between the 3$^{\text{rd}}$ signal and 3$^{\text{rd}}$ idler (S_3I_3) (Fig. 3.4b), and the coincidences between the 2$^{\text{nd}}$ signal and 3$^{\text{rd}}$ idler (S_2I_3) (Fig. 3.4c). The absence of a coincidence peak between the 2$^{\text{nd}}$ signal and 3$^{\text{rd}}$ idler reveals a lack of correlation between mismatched frequencies. In addition, we were able to obtain a high coincidence to accidental ratio (CAR) of 52 for the 3$^{\text{rd}}$ sideband pair, without compensating for the losses in our setup; if we take into account the losses from the biphoton generation stage up till detection, the corrected CAR would be 655.

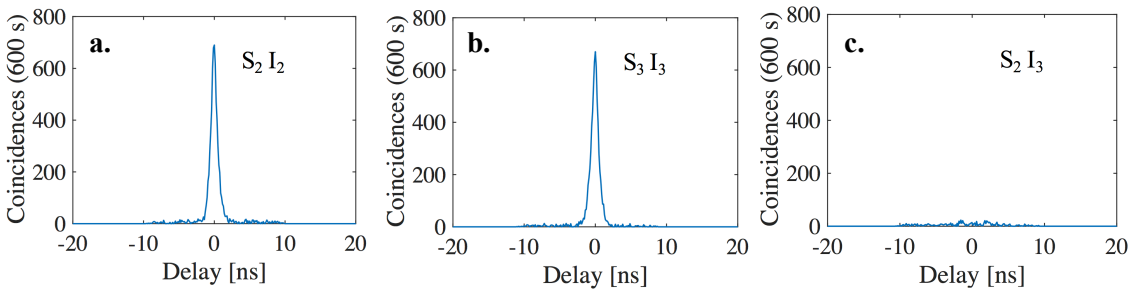

Fig. 3.4. Time correlations for a. S_2I_2, b. S_3I_3 and c. S_2I_3.

3.3 Joint Spectral Intensity

In order to show the spectro-temporal correlations across the photon-pair spectrum, we measured the Joint Spectral Intensity (JSI) by using the pulse shaper as a programmable frequency filter to route different sidebands to the pair of detectors (Fig. 3.5). The time correlation measurement was repeated between all combinations of the sideband pairs from 2 to 7 ($S_{2-7}I_{2-7}$). Figure 3.6a shows the measured JSI, which provides a strong confirmation that time correlations only appear in the energy matched sidebands. Following the same procedure to measure the JSI for the 50-GHz-FSR ring, we obtain Fig. 3.6b, which shows the tight diagonal correlations between diagonal modes up to the 40^{th} mode. We note that JSI does not have any phase information, and does not show the phase coherence between different modes. These JSIs show the potential of these microrings for high-dimensional frequency-bin entanglement— if the phase coherence between frequency bins is proven.

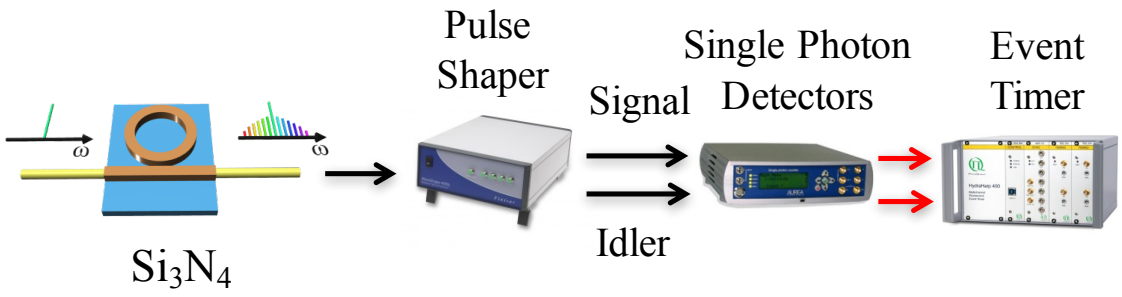

Fig. 3.5. Experimental setup to measure the JSI.

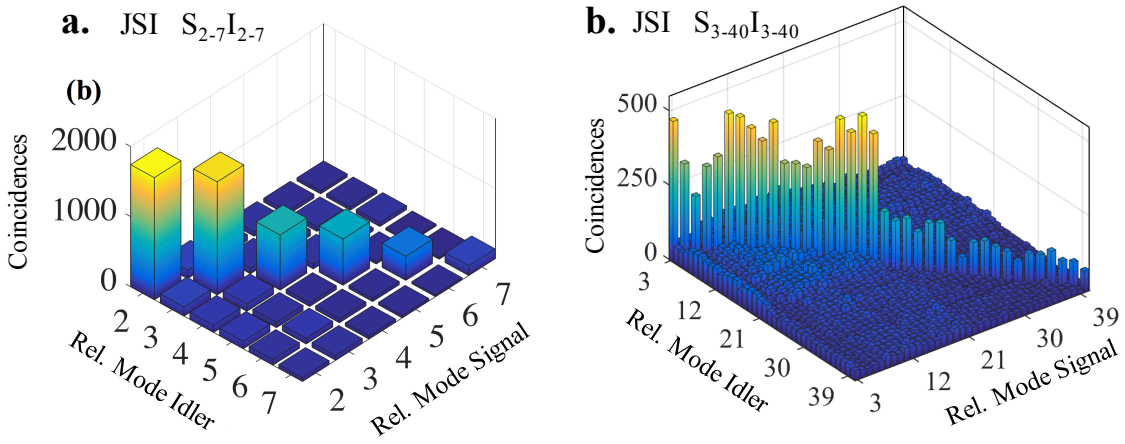

Fig. 3.6. JSI of the microring with a. 380 GHz FSR. b. 50 GHz FSR.

4. TIME-DOMAIN MANIPULATION

4.1 Introduction

In this chapter, we investigate the time-frequency signatures of the BFC generated from the microring with the FSR of 380 GHz [19]. Using a Franson interferometer, we examine the multifrequency nature of the photon pair source in a time entanglement measurement scheme; having multiple frequency modes from the BFC results in a modulation of the interference pattern. This measurement together with a Schmidt mode decomposition shows that the generated continuous variable energy-time entangled state spans multiple pair-wise modes.

For this experiment, a Franson interferometer–two unbalanced Mach-Zehnder interferometers (MZIs)–is placed in the signal and idler paths (Fig. 4.1). The relative delays between long and short arms in the signal and idler interferometers, defined as τ_{s} and τ_{i}, respectively, are approximately 6 ns. This value is much less than the coherence time of the pump ($\sim 1\ \mu$s) but greater than the coherence time of a single photon (~ 1 ns) to avoid self-interference. Here, the difference between τ_{s} and τ_{i} is defined as τ_{d}. When τ_{d} is near to 0, the arrival time difference between signal and idler photons traveling through the long arms is approximately the same as when they both travel through the short arms. In consequence, we have path indistinguishability in this detection scheme using gated detection to only register the mentioned events ($|SS\rangle$ and $|LL\rangle$), discarding the events in which the signal photon travels the long path and the idler photon travels the short path and vice versa ($|SL\rangle$ and $|LS\rangle$). This indistinguishability between the quantum states gives us the ability to interfere them and show a non-classical behavior called time-bin entanglement.

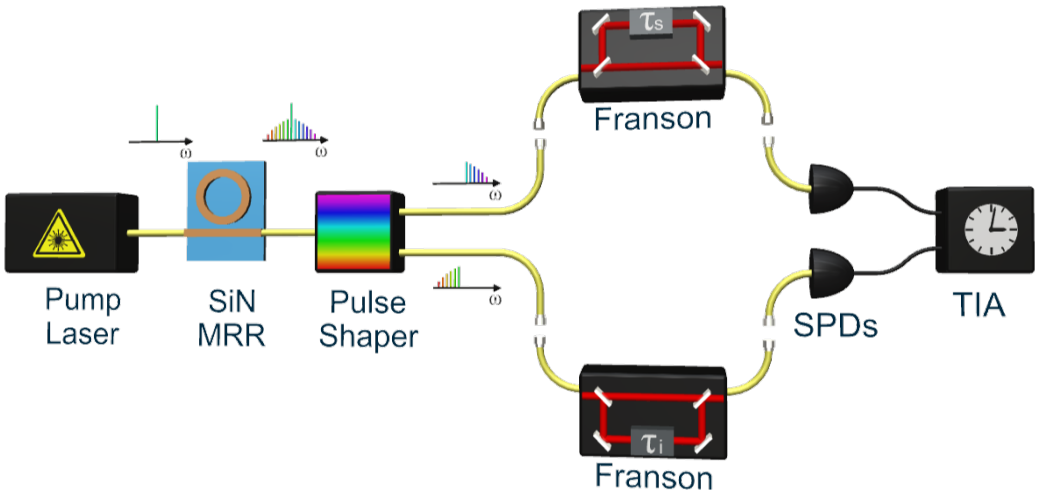

Fig. 4.1. Experimental setup for Franson interferometry.

4.2 Theory

We verify the time entanglement between photon pairs from the biphoton frequency comb (BFC) by separating signal and idler photons and sending each into an unbalanced Mach-Zehnder interferometer [25]. The probability distribution of detecting a signal photon at time $t + \tau$ and its corresponding idler photon at time t is given by the Glauber second order correlation function [26],

$$G^{(2)}(\tau) = |\phi(\tau)|^2 \tag{4.1}$$

and $\phi(\tau)$ is the biphoton wavepacket given by

$$\phi(\tau) \sim \int d\Omega \Phi(\Omega) e^{-i\Omega\tau} \tag{4.2}$$

where $\Phi(\Omega)$ is the spectrum of the biphoton frequency comb. First, we consider a signal-idler photon pair generated in a superposition of two frequency-bin pairs, $|n, n\rangle_{SI}$ and $|n+1, n+1\rangle_{SI}$, generated with equal amplitudes in two contiguous resonances. The temporal wavefunction of this biphoton state is denoted by:

$$|\psi(\tau)\rangle = \phi(\tau)\left(|n,n\rangle_{SI} + e^{i\Delta\omega\tau}\,|n+1,n+1\rangle_{SI}\right) \tag{4.3}$$

Here, $\phi(\tau)$ is assumed the same for both sideband pairs, and the second order correlation function can be expressed as $\langle\psi(\tau)|\,\psi(\tau)\rangle$. In addition, there exists a phase term ($e^{i\Delta\omega\tau}$) multiplying the contributions of the two sideband pairs which is dependent on the frequency spacing between them or FSR, $\Delta\omega$. A measurement of the coincidences between photon pairs would yield a correlation function $G^{(2)}(\tau)$; as a result of the phase term, the correlation peak will contain fast fringes with oscillation period $2\pi/\Delta\omega$ under an envelope of duration proportional to the inverse of the linewidth (see Fig. 4.2). However, using our single-photon detectors, we are only able to observe the envelope of the correlation function; the inability to resolve the fast fringes stems from the large timing-jitter of our single-photon detectors (300 ps).

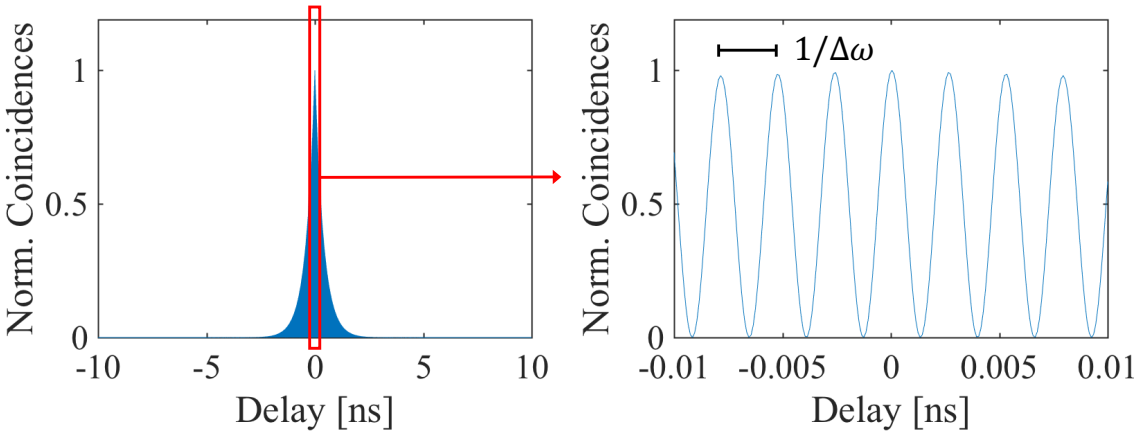

Fig. 4.2. Theoretical correlation function for two sideband pairs of the BFC. The zoomed in plot shows the fast fringes inside the correlation envelope.

Now, we add the unbalanced interferometers in the paths of the signal and idler, with the long paths having an extra relative delay of τ_s and τ_i for each interferometer, respectively. The wavefunctions for the n^{th} and $(n+1)^{th}$ sideband pairs are described

in Eqs. 4.4 and 4.5, respectively, as the interferometers result in path indistinguishability between the short and long paths.

$$|\psi(\tau)\rangle_n = \phi(\tau)\left(|SS\rangle_n + e^{i(\omega_{s_n}\tau_s+\omega_{i_n}\tau_i)}|LL\rangle_n\right) \tag{4.4}$$

$$|\psi(\tau)\rangle_{n+1} = \phi(\tau)\left(|SS\rangle_{n+1} + e^{i(\omega_{s_{n+1}}\tau_s+\omega_{i_{n+1}}\tau_i)}|LL\rangle_{n+1}\right) \tag{4.5}$$

Here, $|SS\rangle_n$ represents the state when signal and idler photons of the n^{th} sideband pair take the short path in their corresponding interferometers. Likewise, $|LL\rangle_n$ represents the state when both photons take the long path. ω_{s_n} and ω_{i_n} are the central frequencies of the signal and idler resonances of the n^{th} sideband pair. Using the energy matching and cavity resonance conditions,

$$2\omega_p = \omega_{s_n} + \omega_{i_n} \tag{4.6}$$

$$\Delta\omega = \omega_{i_n} - \omega_{i_{n+1}} = \omega_{s_{n+1}} - \omega_{s_n} \tag{4.7}$$

and defining:

$$\tau_d = \tau_i - \tau_s \tag{4.8}$$

We can rewrite Eqs. 4.4 and 4.5 as

$$|\psi(\tau)\rangle_n = \phi(\tau)\left(|SS\rangle_n + e^{i(2\omega_p\tau_s+\omega_{i_n}\tau_d)}|LL\rangle_n\right) \tag{4.9}$$

$$|\psi(\tau)\rangle_{n+1} = \phi(\tau)\Big(|SS\rangle_{n+1} + e^{i(2\omega_p\tau_s+\omega_{i_n}\tau_d+\Delta\omega\,\tau_d)}|LL\rangle_{n+1}\Big) \tag{4.10}$$

If τ_d is set to zero ($\tau_i = \tau_s$), the wave function for the n^{th} sideband is

$$|\psi(\tau)\rangle_n = \phi(\tau)\Big(|SS\rangle_n + e^{i2\omega_p\tau_s}|LL\rangle_n\Big) \tag{4.11}$$

which is consistent for all the sidebands. As Eq. 4.11 suggests, in this case, both comb line pairs show a similar effect and interference pattern. To prove this, we go even further and use three signal and idler frequency-bin pairs $S_{2-4}I_{2-4}$. If tau_s and τ_i are both swept together, it is as if the signal and idler photons are both sent through the same interferometer, therefore, for this experiment, we send both photons through the same interferometer and were split after using a pulse shaper.

By sweeping the delay of the interferometer, we retrieve a sinusoidal coincidence pattern with a period of ~ 2.5 fs (half the period of the pump laser) and a visibility of $80\% \pm 5\%$ for all signal and idler sidebands (Fig. 4.3). The interference pattern is similar to those reported in previous microcavity BFC experiments that examined only a single signal-idler pair [27–29]. The visibility higher than 71% [30] shows evidence of energy-time entanglement for biphotons consisting of a multiplicity of sideband mode pairs.

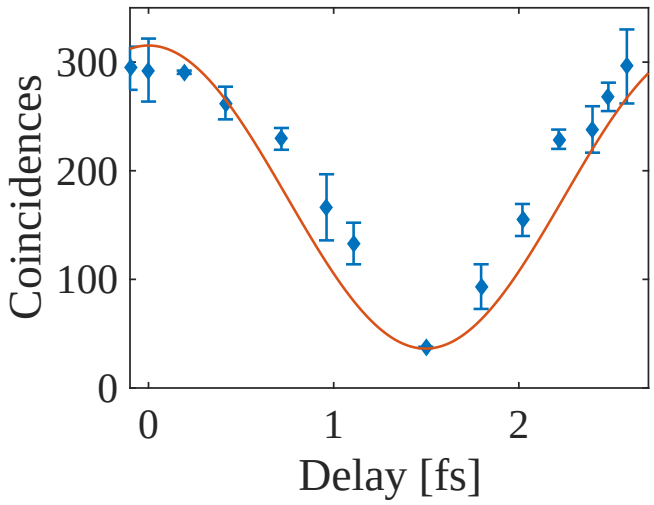

Fig. 4.3. Measured coincidences while simultaneously sweeping the interferometer delay for signal and idler.

If τ_{d} is not equal to 0, and we consider sidebands n and $n+1$, the overall wavefunction can now be written as:

$$\begin{aligned} |\psi(\tau)\rangle_{n,n+1} = \phi(\tau)\left(|SS\rangle_n + e^{i(2\omega_p\tau_{\mathrm{s}}+\omega_{\mathrm{i}_n}\tau_{\mathrm{d}})}|LL\rangle_n\right) \\ +e^{i\Delta\omega\tau}\phi(\tau)\left(|SS\rangle_{n+1} + e^{i(2\omega_p\tau_{\mathrm{s}}+\omega_{\mathrm{i}_n}\tau_{\mathrm{d}}+\Delta\omega\tau_{\mathrm{d}})}|LL\rangle_{n+1}\right) \end{aligned} \tag{4.12}$$

The assumed indistinguishability in the arrival times of the states $|SS\rangle$ and $|LL\rangle$ results in a coincidence rate that is given by the squared magnitude of the sum of the contributions of the probability amplitudes described in Eq. 4.12. This coincidence rate as a function of τ is:

$$c(\tau) = \left|\phi(\tau)\left(1 + e^{i(2\omega_p\tau_{\mathrm{s}}+\omega_{\mathrm{i}_n}\tau_{\mathrm{d}})} + e^{i\Delta\omega\tau}\left(1 + e^{i(2\omega_p\tau_{\mathrm{s}}+\omega_{\mathrm{i}_n}\tau_{\mathrm{d}}+\Delta\omega\tau_{\mathrm{d}})}\right)\right)\right|^2 \tag{4.13}$$

In the limit of slow detection, the coincidence rate is integrated over a long range of delays and expressed as

$$C = \int_{-\Delta}^{\Delta} c(\tau)d\tau \tag{4.14}$$

We used $\Delta = 500$ ps as our delay range in simulations. Eq. 4.14 can be solved to obtain the following expression for the two sideband pair coincidences

$$C_{2\mathrm{SB}} \propto 1 + \cos\left(2\omega_p\tau_{\mathrm{s}} + \frac{\omega_{\mathrm{i}_n} + \omega_{\mathrm{i}_{n+1}}}{2}\tau_{\mathrm{d}}\right)\cos\left(\frac{\Delta\omega}{2}\tau_{\mathrm{d}}\right) \tag{4.15}$$

If we adopt the same procedure for three adjacent sideband pairs (n,$n+1$,$n+2$), we obtain Eq. 4.16.

$$C_{3\mathrm{SB}} \propto 3 + \cos\left(2\omega_p\tau_{\mathrm{s}} + \omega_{\mathrm{i}_{n+1}}\tau_{\mathrm{d}}\right)\left(1 + 2\cos\left(\Delta\omega\tau_{\mathrm{d}}\right)\right) \tag{4.16}$$

We define the visibility as:

$$V = \frac{C_{\max} - C_{\min}}{C_{\max} + C_{\min}} \tag{4.17}$$

where $C_{\max}$ and $C_{\min}$ are the maximum and minimum of the coincidences over a fast variation of delay as shown in Fig 4a. Given this expression, the visibilities of this experiment for 2 and 3 sideband pairs are:

$$V_{2\mathrm{SB}} = \left|\cos\left(\frac{\Delta\omega}{2}\tau_{\mathrm{d}}\right)\right| \tag{4.18}$$

$$V_{3\mathrm{SB}} = \frac{1}{3}\left|1 + 2\cos\left(\Delta\omega\,\tau_{\mathrm{d}}\right)\right| \tag{4.19}$$

4.3 Experimental Results

To see the multifrequency signature, we fix τ_{s} and vary τ_{i} (hence varying τ_{d}) in the two interferometer experiment. Sweeping τ_{d} over a small range results in a sinusoidal interference pattern in the registered coincidences, as shown in Figs. 4.4a,d. The period of ∼5 fs corresponds to the average optical carrier frequency. For Figs. 4.4a-c we use two pairs of sidebands ($S_{2-3}I_{2-3}$). By varying τ_{d} over a larger range, we observe modulation and revival of the envelope of the two-photon fringes with a period of 2.6 ps, corresponding to the inverse of the FSR. In contrast, the fringe envelope for an individual signal-idler pair should decay smoothly on the sub-ns time scale of Fig. 3.6 [27, 28]; the observation of picosecond scale modulation arises from the superimposed contributions of multiple signal-idler frequency bins.The envelope and visibility of the coincidences agree with the quantum mechanical model, eq. 4.15. We repeated this experiment for 3 sideband pairs ($S_{2-4}I_{2-4}$)—the intensities of these sidebands were equalized with the pulse shaper in order to have almost equal contribution in the interference experiment. With increased number of sideband pairs, the visibility vs. delay curve becomes sharper (Fig. 4.4d-f), again in agreement with theory (Eq. 4.16). The visibility of the fringes in Fig. 4.4 is as high as 92% ± 13%. The modulation in the fringe envelope, down to 14% ± 2%, gives us clear evidence of equal contribution of these sidebands in the coincidence pattern.

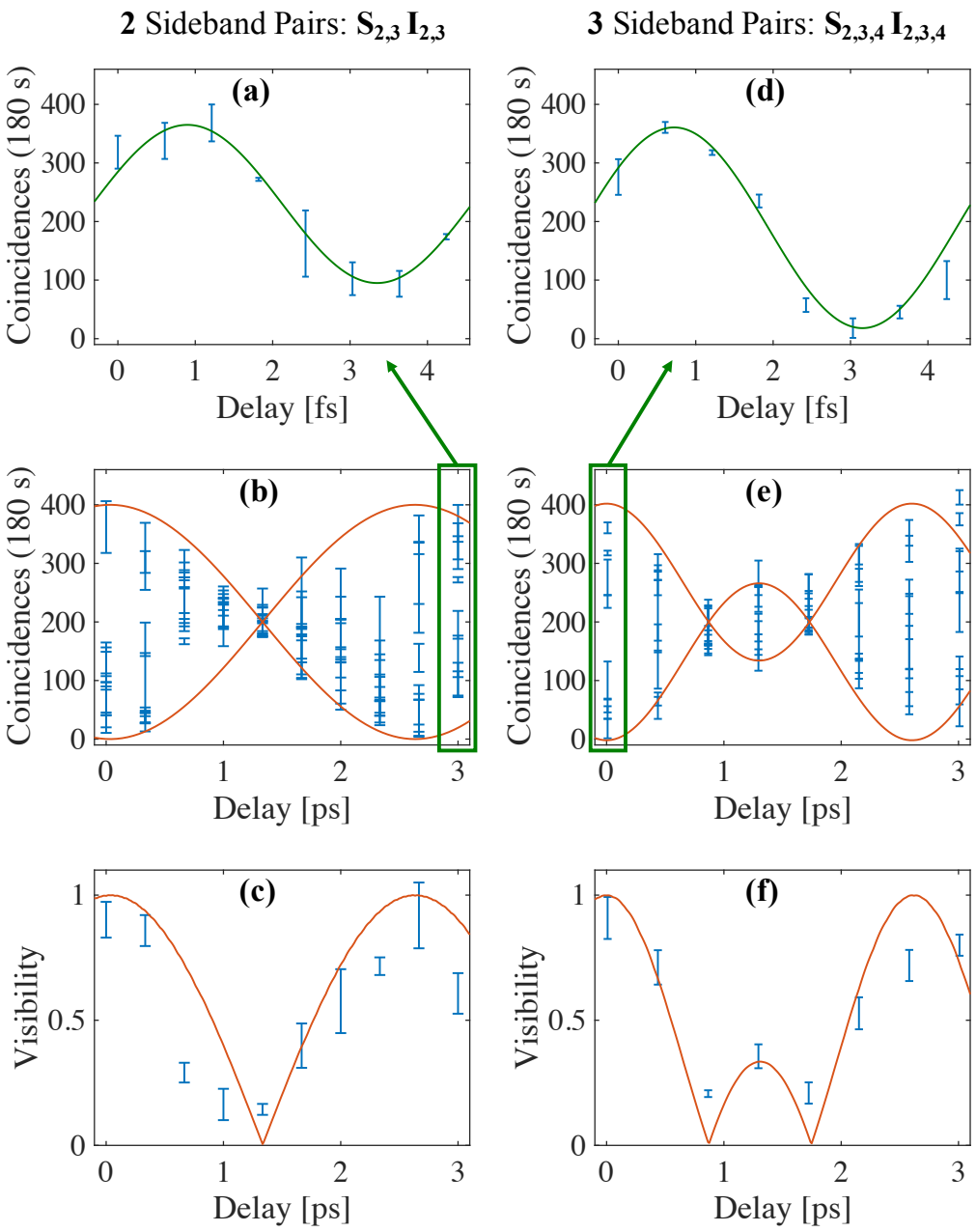

Fig. 4.4. Two-photon interference experiment of the BFC. Interference fringes measured with a Franson interferometer for a. small and b. large τ_d ranges with two sideband pairs. c. The visibility of the sinusoidal fringes in b. Registered coincidences using three sideband pairs for d. small and e. large τ_d ranges. f. The visibility of the sinusoidal fringes in e. The blue error bars are the experimental results, the red curves in b., c., e. and f. are theoretical predictions, and the green curves in a. and d. are sinusoids fitted to the experimental data.

4.4 Schmidt Decomposition

After examining pairwise time-entanglement, we use a Schmidt mode decomposition technique to measure the degree of correlations between our biphotons [31]. Any spectrally entangled biphoton state can be written as a superposition of separable biphoton states via Schmidt decomposition, where the JSI can be written as [32]:

$$F(\omega_S, \omega_I) = \sum_p \sqrt{\lambda_p} f_p(\omega_S) g_p(\omega_I) \tag{4.20}$$

where $F(\omega_S, \omega_I)$ denotes the JSI function, $f_p(\omega_S)$ and $g_p(\omega_I)$–Schmidt functions–are each complete sets of orthonormal functions and λ_p are the Schmidt magnitudes normalized such that $\sum_p \lambda_p = 1$. Using singular value decomposition, $F(\omega_S, \omega_I)$ can get decomposed to a diagonal matrix with strictly positive values λ_p along the diagonals. The Schmidt decomposition of the JSI can now be used as a measure of the degree of accessible correlations in the state via a Schmidt number [33]:

$$K = \frac{1}{\sum_p \lambda_p^2} \tag{4.21}$$

Note that since the JSI does not contain any phase information of the state, the aforementioned Schmidt number in Eq. 4.21 gives us a lower bound on the degree of correlations. A Schmidt number lower-bound ($K_{\min}$) of 4.0 is measured for the JSI shown in Fig. 3.6a. Therefore, we are able to corroborate a high frequency correlation of our photons, since $K_{\min}$ is greater than one. If the off-diagonal terms are all set to zero in our measured JSI (Fig. 3.6a), we obtain a Schmidt number of 4.08, which confirms that we have a very low number of accidentals in our measurements. This Schmidt number can also be interpreted as the number of bits ($\log_2(K_{\min}) = 2$) that each photon carries and can be shared between two parties when a photon pair is detected, each by one party. We note that while we have large continuous variable energy-time entanglement under pairs of resonance modes as suggested by $\Phi(\Omega)$ in Eq. 2.2—which would result in a very high Schmidt number—our measurement technique does not allow access to the fine structure under each resonance. Thus, the Schmidt

analysis is done on different k modes but time-energy entanglement is on each $|k,k\rangle_{SI}$'s fine structure. Therefore, our Schmidt number bound indicates that the continuous variable energy-time entangled state spans 4 effective modes. The same technique have been used to calculate the Schmidt number of the JSI measured for the 50 GHz FSR microring (3.6b), ($K_{\min} = 20$), showing higher frequency correlations in this case compared to the Schmidt number calculated for the 380 GHz FSR microring.

4.5 Nonlocal Dispersion Cancellation

We proceed to examine the potential of the BFC for QKD by demonstrating a nonlocal dispersion cancellation measurement [34], wherein the correlation peak maintains its undispersed form even though the signal and idler photons are dispersed. This nonlocal dispersion cancellation effect can enhance security in QKD by serving as a non-orthogonal basis to direct time-correlation measurements [18, 35].

If we apply a quadratic spectral phase to the biphotons, the biphoton wavepacket will be modified as follows:

$$\phi(\tau) \sim \int d\Omega \Phi(\Omega) e^{\frac{iD\Omega^2}{2}} e^{-i\Omega\tau} \tag{4.22}$$

where

$$D = D_{\mathrm{s}} + D_{\mathrm{i}} \left[\text{units ps}^2\right] \tag{4.23}$$

D_{s} and D_{i} are the dispersions applied to the signal and idler photons, respectively. Thus, as Franson pointed out [34], the undispersed form of $G^{(2)}$ is reproduced when $D_{\mathrm{s}} = -D_{\mathrm{i}}$. This is the condition for nonlocal dispersion cancellation.

We use the experimental setup illustrated in Fig. 4.5 for this part. First, we use four sideband pairs ($S_{2-5}I_{2-5}$) and measure the correlation function in the absence of dispersion (Fig. 4.6a). Next, we apply dispersion of 2 ns/nm [using a chirped fiber bragg grating (CFBG), which provides a dispersion equivalent to that of $\sim$ 120 km of standard single mode fiber, but with a loss of only 3 dB] to only the signal sidebands

of the BFC; this results in a measurement of four correlation peaks corresponding to the four different sideband pairs. The peaks are spaced by 6 ns, an expected outcome since different frequencies travel at different speeds in a dispersive medium (Fig. 4.6c). Applying the opposite dispersion to only the idler sidebands will result in a similar outcome but with opposite sign of delay variation (Fig 4.6d). These measurements with the separated correlation peaks are equivalent to a frequency-to-time mapping of our BFC, thus enabling us to resolve the JSI in the temporal basis [36]. To emphasize this equivalence, the diagonal terms of the JSI for sideband pairs (S_{2-5}, I_{2-5}) are normalized to the maximum of Fig. 4.6c and plotted as red squares; the good agreement with the correlation peaks in time provides a quantitative confirmation of frequency-to-time mapping. When we apply both dispersive media (positive dispersion on the signals and negative dispersion on the idlers), we expect nonlocal cancellation of the dispersion. As shown in Fig. 4.6b, this behavior is clearly observed: the coincidence plot collapses back into a single peak, with an improvement in the peak-to-background ratio evident despite the extra loss incurred through the introduction of a second CFBG.

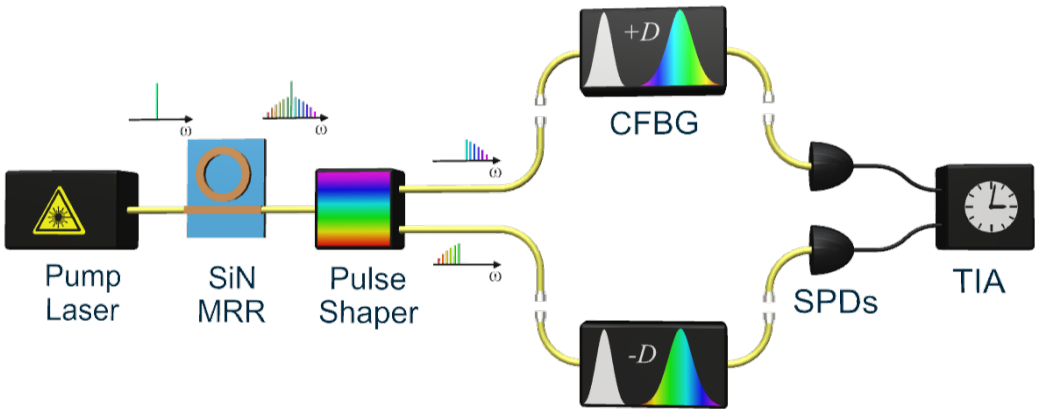

Fig. 4.5. Experimental setup for nonlocal dispersion cancellation.

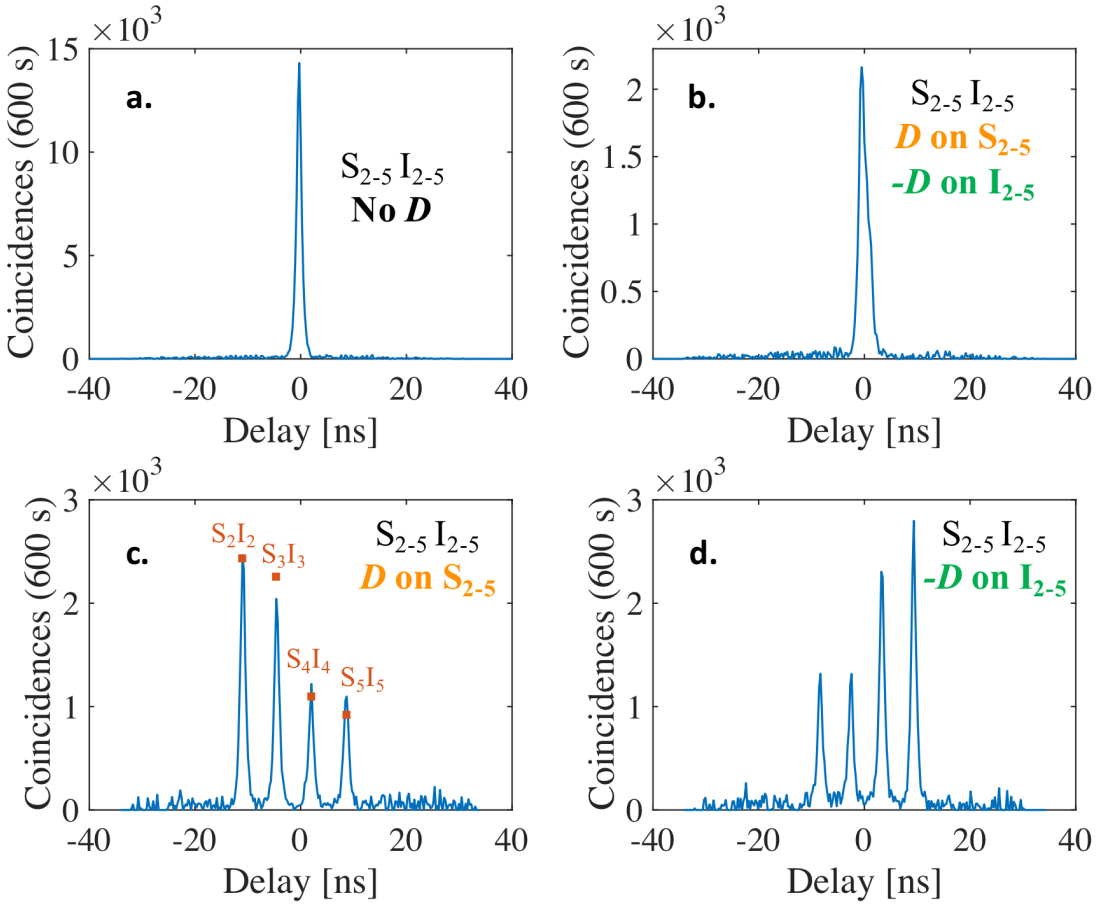

Fig. 4.6. Nonlocal dispersion cancellation experiment. Time correlation of four sideband pairs $S_{2-5}I_{2-5}$ a. without dispersion, c. with positive dispersion of $D = 2$ ns/nm applied on signal photons S_{2-5}, d. with negative dispersion of $D = -2$ ns/nm applied on idler photons I_{2-5}, and b. with both dispersions applied at the same time as shown in Fig. 4.5 for nonlocal dispersion cancellation. In these plots, accidentals were subtracted and the effect of a finite detection-gate width (which results in a roll-off in coincidences as one moves away from zero delay) was compensated. The red squares in b. represent the diagonal of the JSI in Fig 3.6b for the sideband pairs $S_{2-5}I_{2-5}$, normalized to the maximum of the blue plot for ease of visualization.

5. FREQUENCY-DOMAIN MANIPULATION

5.1 Introduction

In photonics, amongst different degrees of freedom capable of high-dimensionality, the frequency domain–using single or entangled photons in a coherent superposition of multiple frequency bins–offers more robust and scalable systems because it does not require stabilization of interferometers or complex beam shaping [11, 37]. Frequency-bin entangled photons have already been explored through SPDC together with cavity and programmable spectral filtering [38–40]. While chip-scale devices have been used to generate comb-like photon pairs through SFWM [19, 28, 29], the ensuing photon states had not been shown to be in a coherent superposition of multiple frequency-bins prior to experiments reported in this chapter. The difficulty of this measurement stems from the large FSR of conventional microring resonators (on the order of 100 GHz) which results in temporal correlation trains with periods ($<$ 10 ps) much less than the timing resolution of standard single-photon detectors ($\sim$ 100 ps)(Fig. 4.2), as discussed in section 4.2. As a result, direct detection of the comb-like photon pairs is incapable of showing spectral phase sensitivity, a condition required to prove frequency-bin entanglement. In this chapter, using a phase modulation scheme to overlap sidebands from different comb lines– in order to create an indistinguishable superposition of frequency states– we are able to conduct a two-photon interference measurement, proving the high dimensional frequency-bin entanglement and phase coherence of our on-chip BFC [21, 41]. The same technique was independently used in [42], showing up to four dimensional frequency-bin entanglement of a Hydex microring resonator, where the FSR was approximately a factor of 4 larger than our 50 GHz microring . Our small FSR allows us to have more than 40 frequency modes (Fig 3.6b), as opposed to 10 frequency modes in [42] . Demonstration of frequency-

bin entanglement is a major step in qualifying integrated biphoton frequency comb sources for applications in scalable high capacity quantum computation [43] and dense quantum communications [18]. To validate our phase modulation approach, we also conducted these experiments with our SPDC source and measured second order dispersion of a single mode fiber (SMF) with known properties using this method.

5.2 Two-Dimensional Frequency-Bin Entanglement

To show phase coherence between different comb line pairs, we implement the setup depicted in Fig. 5.1. The output of the microring is coupled into pulse shaper 1, where in the first experiment we select only comb line pairs 6 (S_6I_6) and 7 (S_7I_7). Subsequently, we will use this pulse shaper to apply optical spectral phase to the comb lines. We also note that we use the first pulse shaper to equalize the contribution of the modes to coincidence counts. By doing so, we are making sure that $|\alpha_k| = |\alpha_{k+1}|$ in Eq. 2.1 for the rest of the experiments, which optimizes contrast in quantum interference. The selected lines are then coupled into an electro-optic phase modulator, which creates optical sidebands at frequency offsets equal to multiples of the radio frequency (rf) of the driving sinusoidal waveform, which we set to yield sidebands at half the spacing of the BFC (Fig. 5.2). Then, with pulse shaper 2, we pick out the sidebands which overlap midway between S_6-S_7 and I_6-I_7 (solid blue curves in Fig. 5.2), and route them to the SPDs and the TIA.

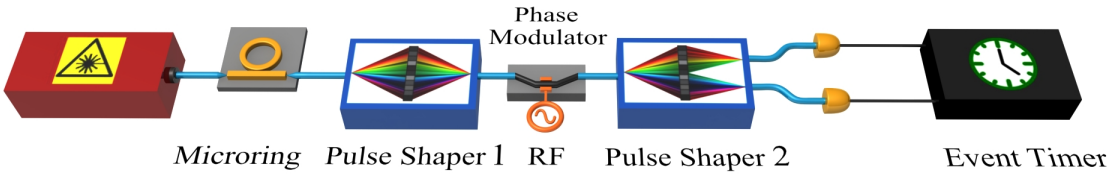

Fig. 5.1. Experimental setup for frequency-bin entanglement.

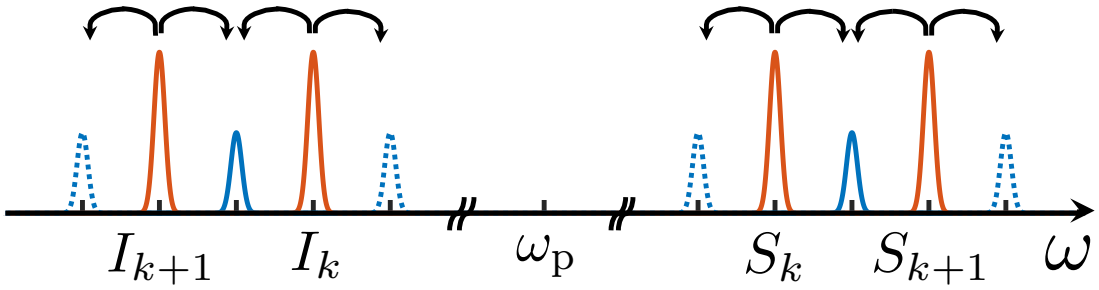

Fig. 5.2. Illustration of biphoton spectrum after phase modulation.

Our frequency-bin entanglement verification scheme is a frequency domain analog of the Franson interferometry approach [25] widely used to verify time-bin entanglement (see Fig. 5.3). As discussed in section 4.2, in Franson interferometry, after an input state in a superposition of two time bins passes through an imbalanced interferometer, results in 3 different states projections $\{|1\rangle, |2\rangle, |S\rangle\}$ at the output, where $|S\rangle$ is the superposition state defined as

$$|S\rangle = \frac{1}{\sqrt{2}}\left(|1\rangle + e^{i\phi}|2\rangle\right) \tag{5.1}$$

and ϕ is a relative phase varied in one of the interferometer arms. In our scheme, we pass a two frequency-bin input state with frequency spacing Δf through the phase modulator, which produces upper and lower sidebands at frequency offsets $\pm\Delta f/2$ from each of the parent signals and idlers. In Fig. 5.3 we label this operation as a "frequency splitter". The upper sideband from one parent signal (idler) frequency overlaps with the lower sideband from the other parent signal (idler) frequency. Accordingly, at the output of the frequency splitter, we will have 3 different state projections $\{|1\rangle, |2\rangle, |S\rangle\}$ where $|S\rangle$ is the superposition state again defined as in Eq. 5.1, but now with ϕ corresponding to a phase imposed onto the biphoton by the first pulse shaper prior to the phase modulator. We can apply different relative phases between the parent frequency bins, and therefore the superposition state $|S\rangle$ can have different representations according to Eq. 5.1. We note that unlike Franson interferometry,

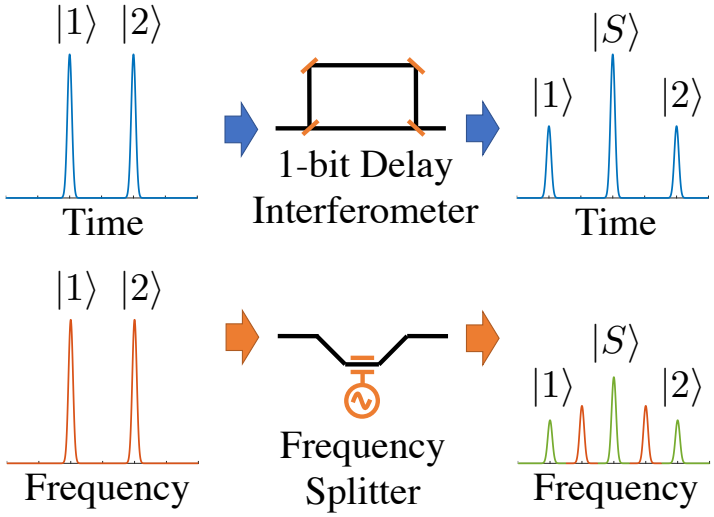

Fig. 5.3. Analogy between a 1-bit delay interferometer for forming projections of time-bin qubits and a frequency splitter for forming projections of a frequency-bin qubit. The green frequency bins after the frequency splitter are phase modulation sidebands from $|1\rangle$ and $|2\rangle$.

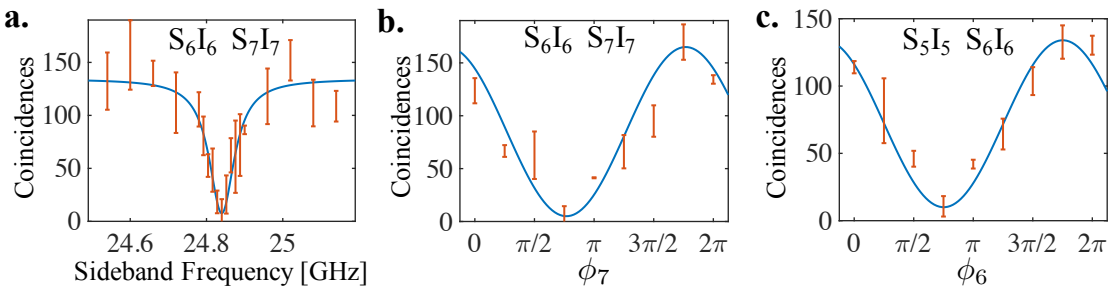

Fig. 5.4. a. Coincidence dip as a function of sideband frequency to maximize the indistinguishability. b. Coincidences of the S_6I_6 and S_7I_7 superposition versus phase applied on S_7I_7. c. Coincidences of the S_5I_5 and S_6I_6 superposition versus phase applied on S_6I_6. The coincidences reported are in a. 20 minutes. and b., c. 10 minutes. and after background subtraction. Each data point was measured three times to obtain the standard deviation indicated by the error bars.

where phase stabilization is needed, here the phases in our frequency interferometry approach are intrinsically stable.

To be able to measure the optimum frequency overlap and maximize the indistinguishability between different phase modulation sidebands, first we apply a relative phase shift of π between S_6I_6 and S_7I_7 using pulse shaper 1—inducing a $\pi/2$ phase on both S_6 and I_6—to create a destructive interference between these two modes. We proceed to measure the coincidences as we sweep the rf frequency to yield a sideband separation from 24.54 to 25.14 GHz. We observe a dip with a maximum visibility of 89% at 24.84 GHz, as shown in Fig. 5.4a. The full width at half maximum of this dip is measured to be $\sim$100 MHz, similar to the resonance linewidth of the microring. We note that background accidentals were subtracted from the plot in Fig. 5.4a and subsequent results in the rest of the chapter, where the coincidence to accidental ratio was about 2:1. This reduction in coincidence to accidental ratio in the phase measurement experiments compared to the JSI measurement in Fig. 3.6b is due to the additional loss that the extra pulse shaper and phase modulator introduce to our biphotons; as a consequence we are forced to use higher pump power and biphoton flux, which reduces the ratio.

Now that we have superposition of the sidebands, we should be able to observe an interference pattern by changing the relative phases of the comb line pairs. Using the first pulse shaper to vary the phases of S_7 and I_7 simultaneously, we obtain a sinusoidal interference pattern in the measured coincidences (Fig. 5.4b). The resulting visibility of $93\% \pm 13\%$ shows strong phase coherence between the comb line pairs S_6I_6 and S_7I_7. Following the same procedure but selecting comb line pairs S_5I_5 and S_6I_6 and sweeping the phases of S_6 and I_6 simultaneously, we obtain a visibility of $86\% \pm 11\%$ (Fig. 5.4c). By assuming a white noise model for the noise introduced to the state, since these visibilities exceed the classical threshold of 71%, the two-dimensional frequency-bin entanglement is proven between these comb line pairs [44].

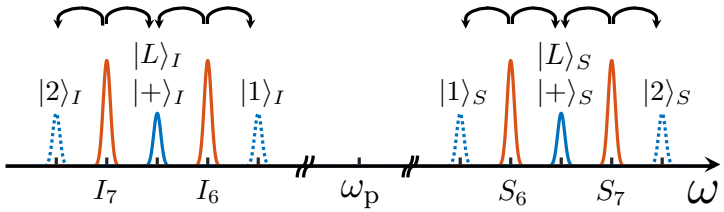

Fig. 5.5. Phase modulation scheme for quantum state tomography. Red peaks represent the input signal and idler, each of which is in one of two frequency bins. Blue curves represent projections of signal and idler after the phase modulator (frequency splitter) into three new frequency positions. Solid blue is a projection of the superposition state; dashed blue peaks represent a projection from a single signal or idler frequency bin.

5.3 Quantum State Tomography

To extract all the information about our entangled state, we perform quantum state tomography by measuring a complete set of 16 projections of the two-qubit entangled state [45, 46] which allows us to estimate the density matrix. We performed coincidence measurements between signal and idler photons in the 16 possible combinations of the states $\{|1\rangle, |2\rangle, |L\rangle, |+\rangle\}$. Here, $|L\rangle$ and $|+\rangle$ are the superposition states in Eq. 5.1 when ϕ is equal to $\pi/2$ and 0, respectively, as shown in Fig. 5.5. Because we can make an exact analogy between our approach for projecting frequency-bin qubits and the Franson interferometry approach for projecting time-bin qubits, we can perform quantum state tomography of two-photon frequency-bin qubit states using an exact transcription of the measurement protocol for two-photon time-bin qubit states detailed in [46].

The measurement protocol and coincidence count data for the quantum state tomography are given in Table 5.1. Table 5.1 may be understood as follows. Since the two-qubit density matrix is 4×4, we require a complete set of 16 projections $|\Psi_\nu\rangle$ $(\nu = 1:16)$, written in terms of its basis coefficients $(\langle 11|\Psi_\nu\rangle, \langle 12|\Psi_\nu\rangle, \langle 21|\Psi_\nu\rangle, \langle 22|\Psi_\nu\rangle)$. We perform these projections by acquiring data in four different phase configurations

$(\phi_S, \phi_I) = \{(0,0),(0,\pi/2),(\pi/2,0),(\pi/2,\pi/2)\}$, columns 5-8. Here, in performing tomography on the S_6I_6-S_7I_7 qubit pair, ϕ_S and ϕ_I are the signal and idler phases applied to the 7^{th} comb line pair via pulse shaper 1 in the experimental setup shown in Fig. 5.1. For each projection columns 2 and 3 specify which signal and idler frequency channel are routed to the respective single photon detectors. Referring to Fig. 5.5, $|1\rangle$ and $|2\rangle$ in columns 2 and 3 correspond to unique frequency channels, whereas $|+\rangle$ and $|L\rangle$ are both sideband superpositions measured when the same physical frequency channel is routed for detection. Therefore, an entry in column 2 of $|+\rangle$ or $|L\rangle$ signifies both routing of the signal superposition frequency channel for detection and application of the appropriate phase to the 7^{th} signal line (0 phase for $|+\rangle$, data reported in column 5 or 6; $\pi/2$ phase for $|L\rangle$, data reported in column 7 or 8). An entry in column 3 of $|+\rangle$ or $|L\rangle$ has similar meaning, but refers to the idler superposition frequency channel (data in column 5 or 7 for $|+\rangle$, column 6 or 8 for $|L\rangle$). As an example, for $|\Psi_8\rangle$ we have $(\phi_S, \phi_I) = (\pi/2, 0)$, column 7, and we obtain:

$$\begin{aligned} |\Psi_8\rangle &= \frac{1}{\sqrt{2}}\left(|1\rangle_S + e^{i\phi_S}|2\rangle_S\right).\frac{1}{\sqrt{2}}\left(|1\rangle_I + e^{i\phi_I}|2\rangle_I\right) \\ &= \frac{1}{2}|1,1\rangle_{SI} + \frac{1}{2}|1,2\rangle_{SI} + \frac{i}{2}|2,1\rangle_{SI} + \frac{i}{2}|2,2\rangle_{SI} \\ &= \left(\frac{1}{2},\frac{1}{2},\frac{i}{2},\frac{i}{2}\right) \end{aligned} \tag{5.2}$$

In this notation $|x,y\rangle_{SI} = |x\rangle_S |y\rangle_I$, in which signal and idler photons are in frequency bins x and y, respectively.

Also, as explained in [46], for each of the signal and idler photons, measurement in a nonsuperposition basis ($|1\rangle$ or $|2\rangle$) involves a factor of two loss relative to measurement in the superposition channel. This is understood in the time-bin case as the loss incurred at the output beam splitter of the interferometer, since for nonsuperposition bases, half of the photons go to the unused output port. For the superposition cases, with constructive interference such loss is avoided. The same argument holds in our frequency-bin approach. These factors of two that arise for each of signal and idler are accounted for by noting for projections such as $|\Psi_1\rangle = |11\rangle$, which incur a factor of

four loss, coincidences may be measured for each of the four phase configurations. The corresponding coincidence counts are listed in columns 5 to 8 and are added to give a total coincidence count (column 9). Likewise, projections such as $|\Psi_6\rangle = |1+\rangle$ incur a factor of two loss but may be measured in two phase configurations, and projections such as $|\Psi_7\rangle = |++\rangle$ incur no extra loss but are measured in only a single-phase configuration. Overall, 36 independent measurements are performed, and the total number of coincidence counts obtained by adding the entries in columns 5-8 (column 9, n_ν) provides the correct normalization across the different projections.

Table 5.1.
Projection measurements for frequency-bin density matrix estimation. For each measurement coincidences were acquired over a 10-minute period. A dash (-) indicates that the phase setting indicated by the respective column is not involved in the projection measurement indicated by the respective row; hence coincidence counts were not obtained.

ν	Signal Photon	Idler Photon	$\lvert\Psi_\nu\rangle$	(ϕ_S, ϕ_I)				n_ν
				$(0,0)$	$\left(0,\frac{\pi}{2}\right)$	$\left(\frac{\pi}{2},0\right)$	$\left(\frac{\pi}{2},\frac{\pi}{2}\right)$	
1	$\lvert 1\rangle$	$\lvert 1\rangle$	$(1,0,0,0)$	36	40	36	41	153
2	$\lvert 1\rangle$	$\lvert 2\rangle$	$(0,1,0,0)$	9	8	0	0	17
3	$\lvert 2\rangle$	$\lvert 1\rangle$	$(0,0,1,0)$	0	0	0	7	7
4	$\lvert 2\rangle$	$\lvert 2\rangle$	$(0,0,0,1)$	47	29	44	31	151
5	$\lvert 2\rangle$	$\lvert +\rangle$	$\left(0,0,\frac{1}{\sqrt{2}},\frac{1}{\sqrt{2}}\right)$	26	-	40	-	66
6	$\lvert 1\rangle$	$\lvert +\rangle$	$\left(\frac{1}{\sqrt{2}},\frac{1}{\sqrt{2}},0,0\right)$	47	-	22	-	69
7	$\lvert +\rangle$	$\lvert +\rangle$	$\left(\frac{1}{2},\frac{1}{2},\frac{1}{2},\frac{1}{2}\right)$	146	-	-	-	146
8	$\lvert L\rangle$	$\lvert +\rangle$	$\left(\frac{1}{2},\frac{1}{2},\frac{i}{2},\frac{i}{2}\right)$	-	-	71	-	71
9	$\lvert L\rangle$	$\lvert 1\rangle$	$\left(\frac{1}{\sqrt{2}},0,\frac{i}{\sqrt{2}},0\right)$	-	-	14	57	71
10	$\lvert L\rangle$	$\lvert 2\rangle$	$\left(0,\frac{1}{\sqrt{2}},0,\frac{i}{\sqrt{2}}\right)$	-	-	26	44	70
11	$\lvert L\rangle$	$\lvert L\rangle$	$\left(\frac{1}{2},\frac{i}{2},\frac{i}{2},\frac{-1}{2}\right)$	-	-	-	4	4
12	$\lvert 1\rangle$	$\lvert L\rangle$	$\left(\frac{1}{\sqrt{2}},\frac{i}{\sqrt{2}},0,0\right)$	-	21	-	29	50
13	$\lvert 2\rangle$	$\lvert L\rangle$	$\left(0,0,\frac{1}{\sqrt{2}},\frac{i}{\sqrt{2}}\right)$	-	44	-	31	75
14	$\lvert +\rangle$	$\lvert L\rangle$	$\left(\frac{1}{2},\frac{i}{2},\frac{1}{2},\frac{i}{2}\right)$	-	62	-	-	62
15	$\lvert +\rangle$	$\lvert 1\rangle$	$\left(\frac{1}{\sqrt{2}},0,\frac{1}{\sqrt{2}},0\right)$	16	29	-	-	45
16	$\lvert +\rangle$	$\lvert 2\rangle$	$\left(0,\frac{1}{\sqrt{2}},0,\frac{1}{\sqrt{2}}\right)$	49	32	-	-	81

As in [45, 46], we perform a maximum likelihood estimate to obtain the density matrix that best fits our projection measurement data (the n_ν) while satisfying the requirement for a physical density matrix that the eigenvalues lie in the interval

[0,1]. The measurement consists of 16 coincidences $\bar{n}_\nu$ whose expected value can be estimated from the density matrix by $\bar{n}_\nu = C \langle \Psi_\nu | \rho | \Psi_\nu \rangle$, where $C = \sum_{\nu=1}^{4} n_\nu$ is the normalization constant. We assume the noise in these measurements to have a Gaussian probability distribution, therefore, the probability of obtaining a set of 16 coincidences $\{n_1, n_2, ..., n_16\}$ is [45]:

$$P(n_1, n_2, ..., n_16) = \frac{1}{N_{norm}} \prod_{\nu=1}^{16} exp\Big[- \frac{(n_\nu - \bar{n}_{nu})^2}{2\sigma_\nu^2} \Big] \tag{5.3}$$

where σ_ν is the standard deviation of the ν^{th} coincidence measurement approximated by $\sqrt{\bar{n}_{nu}}$, and N_{norm} is the normalization constant. Estimating the n_ν values using the density matrix and measured values, this probability can be written down as:

$$P(n_1, n_2, ..., n_16) = \frac{1}{N_{norm}} \prod_{\nu=1}^{16} exp\Big[- \frac{(C \langle \Psi_\nu | \rho | \Psi_\nu \rangle - n_\nu)^2}{2C \langle \Psi_\nu | \rho | \Psi_\nu \rangle} \Big] \tag{5.4}$$

Rather than finding the maximum for $P(n_1, n_2, ..., n_16)$, it is simpler to find the maximum of its logarithm which is mathematically equivalent [47], so in our optimization, we find the minimum of the likelihood function:

$$\mathcal{L} = \sum_{\nu=1}^{16} \frac{\big(C \langle \Psi_\nu | \rho | \Psi_\nu \rangle - n_\nu\big)^2}{2C \langle \Psi_\nu | \rho | \Psi_\nu \rangle} \tag{5.5}$$

As a result of this optimization, we found the following physical density matrix:

$$\rho = \begin{bmatrix} 0.4388 + 0.0000i & -0.0115 - 0.0699i & -0.0721 - 0.0193i & 0.3745 + 0.0166i \\ -0.0115 + 0.0699i & 0.0574 + 0.0000i & 0.0279 - 0.0244i & 0.0084 - 0.0227i \\ -0.0721 + 0.0193i & 0.0279 + 0.0244i & 0.0281 + 0.0000i & -0.0280 - 0.0211i \\ 0.3745 - 0.0166i & 0.0084 + 0.0227i & -0.0280 + 0.0211i & 0.4757 + 0.0000i \end{bmatrix} \tag{5.6}$$

The estimated real and imaginary parts of the density matrix are shown in Figs. 5.6a and 5.6b, respectively.

To evaluate the amount of entanglement in the measured two-qubit state, we use the Peres-Horodecki criterion [48, 49] and calculate a measure of entanglement from the density matrix called negativity. The negativity of a density matrix ρ is defined as: $N(\rho) = \sum_{i=0}^{3} \frac{|\lambda_i| - \lambda_i}{2}$,where λ_i are the eigenvalues of the partial positive transposed version of ρ. A two-qubit density matrix is separable iff $N(\rho) = 0$, and $N(\rho) > 0$ signifies entanglement (see Appendix B). For a maximally entangled state $N(\rho) = 0.5$, and for the experimentally recovered state given in Eq. 5.6 we find $N(\rho) = 0.34$, strongly indicating inseparability.

5.4 Three-dimensional frequency-bin entanglement

The results presented so far have been for two-dimensional quantum states. Our observation of strong interference contrast involving comb line pairs S_5I_5-S_6I_6 and S_6I_6-S_7I_7 individually suggests phase coherence across lines 5, 6 and 7 jointly. For a proof of such high-dimensionality, however, we must examine phase coherence across the selected comb line pairs simultaneously. Here we consider a biphoton state initially made up of three comb line pairs (two entangled qutrits). We use the first pulse shaper to select the comb line pairs S_5I_5, S_6I_6 and S_7I_7; after the phase modulator, we overlap the first sidebands for the 5^{th} and 6^{th} comb line pairs together with the third sideband

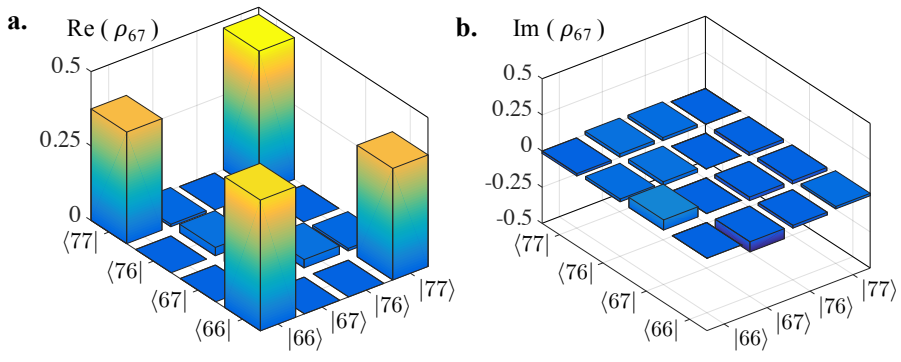

Fig. 5.6. a. Real and b. imaginary parts of the estimated density matrix for comb line pairs S_6I_6 and S_7I_7.

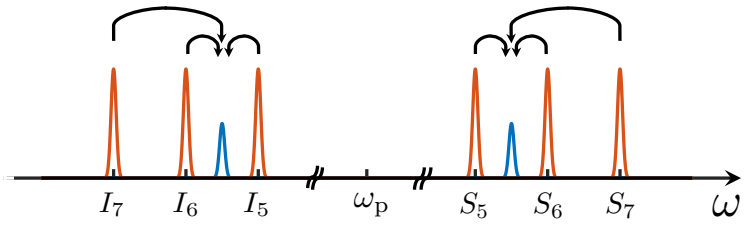

Fig. 5.7. Illustration of overlapped phase modulation sidebands for comb line pairs S_5I_5, S_6I_6 and S_7I_7.

from the 7$^{\text{th}}$ comb line pair. In order to ensure equal mixing weights for all three sidebands, we send a CW test laser through the modulator and adjust the electrical drive power such that the first and third phase modulation sidebands are equalized, as verified with an optical spectrum analyzer. We also use the first pulse shaper to balance the intensities of the biphoton sideband pairs such that individually they each contribute equal coincidence counts (so the three diagonal terms in the JSI are equal), thereby maximizing the potential Bell inequality violation. Additionally, we compensate for the relative phases on the comb line pairs induced by fiber dispersion. Now we use the second pulse shaper to select the overlapping sidebands from the signal and idler triplets (blue curves in Fig. 5.7), which arise from an indistinguishable superposition of contributions from S_5, S_6, S_7 and I_5, I_6, I_7, respectively. Pulse shaper 1 places spectral phases on the signal and idler lines such that the ideal state after the second pulse shaper can be written in the form $|\psi\rangle \propto |5,5\rangle_{SI} + e^{i(\phi_S+\phi_I)}|6,6\rangle_{SI} + e^{i2(\phi_S+\phi_I)}|7,7\rangle_{SI}$. Extensive numerical searches [44] suggest that the largest violation of the 3-dimensional Bell inequality is realized by measurement bases with the property that the phase applied to the 7$^{\text{th}}$ signal and idler should be twice the phase put on the 6$^{\text{th}}$ comb line pair [30]. Now, by setting the phase parameters ϕ_S and ϕ_I to appropriate specific values, we construct a three-dimensional CGLMP inequality ($I_3 \leq 2$) adapted from [44] and described in detail for time-bin and frequency-bin entangled photons in [30, 50], respectively.

We measure coincidences between signal and idler frequency channels selected to represent superpositions from three parent signal and idler frequencies, respectively. Reference [30] evaluated the three-dimensional Bell's inequality for time-bin entangled qutrit states using three-arm interferometers coupled to three different output ports via a 3×3 splitter. They constructed a CGLMP inequality expressed in a form equivalent to the following:

$$\begin{aligned} I_3 = 3\left[P^{11}(0,0) + P^{21}(0,1) + P^{22}(0,0) + P^{12}(0,0)\right] \\ -3\left[P^{11}(0,1) + P^{21}(0,0) + P^{22}(0,1) + P^{12}(1,0)\right] \leq 2 \end{aligned} \tag{5.7}$$

where $P^{xy}(a,b)$ is the probability of getting a coincidence count between detector a on the signal and detector b on the idler side, using the measurement basis A_x and B_y for signal and idler photons, respectively. We note that the original form of the 3-dimensional Bell inequality consists of 24 total measurement probabilities [44]; the reduction to 8 terms (Eq. 5.7), however, is valid under the assumption of an unbiased 3×3 splitter and an input quantum state containing sufficient symmetries. In particular, as we show below, the above reduction holds for a density matrix ρ taken to be the incoherent mixture of a maximally entangled state and white noise in the form of $\rho = \lambda \left|\psi\right\rangle \left\langle\psi\right| + \frac{1-\lambda}{9}\mathbb{I}_9$ with $0 \leq \lambda \leq 1$ [30]. Such an assumption is physically reasonable and common in visibility-based Bell-violation tests. For the time-bin case, the measurement bases correspond to the sets of phases applied to short, medium, and long interferometer arms. The particular sets of phases used are $[A_1 = (0,0,0), A_2 = (0,\pi/3,2\pi/3)]$ for the signal and $[B_1 = (0,\pi/6,\pi/3), B_2 = (0,-\pi/6,-\pi/3)]$ for the idler. These choices of phases have been shown to give the largest violation of the CGLMP inequality for a maximally entangled state [30]. In the classical picture, if the signal and idler are two independent systems, meaning a measurement on the signal does not affect the idler, and vice versa, then $I_3 \leq 2$. However, for an entangled state this classical limit may be violated, and with the set of phases specified, a maximum violation $I_{3\max} = 2.872$ is predicted for a maximally entangled state.

In our frequency bin case, the different measurement bases are constructed by putting different sets of phases on different comb line triplets. For example, for a triplet consisting of comb lines 5-7 as in our experiment, for signal measurement basis A_2 we would place phases $(0, \pi/3, 2\pi/3)$ on signal lines 5, 6, and 7, respectively. However, unlike the 3×3 beam splitter case, we have only a single detector each for signal and idler. This can be accounted for by imposing additional phases on the comb lines according to the equivalent transfer function of the 3×3 beam splitter [51, 52]. Equalizing the power in the ± 1 and ± 3 phase modulation sidebands gives us the ability to perform an unbiased beam splitter in frequency, thereby satisfying one of the key assumptions behind the reduced form (Eq. 5.7). The phases are chosen from $\{0, -2\pi/3, 2\pi/3\}$ according to which "beam splitter output" is involved in the projection that we are mapping from the three-output time-bin case to our one-output frequency-bin case [30, 50]. In this way, we adapt the CGLMP inequality for time-bin entangled photons to our frequency bins by applying different sets of phases to our comb lines [50]. For our experiment involving comb lines 5, 6, and 7, the phases applied to signal and idler lines k are given by:

$$\Phi^x_{S_k}(a) = (k-5)\phi^x_S(a) = \frac{2\pi}{3}(k-5)\,(a + \alpha_x) \tag{5.8}$$

$$\Phi^y_{I_k}(b) = (k-5)\phi^y_I(b) = \frac{2\pi}{3}(k-5)\,(-b + \beta_y) \tag{5.9}$$

Here, $\Phi^x_{S_k}(a)$ and $\Phi^y_{I_k}(b)$ are the phases applied to the k^{th} signal and idler frequency bin, respectively, expressed in terms of fundamental phases $\phi^x_S(a)$ and $\phi^y_I(b)$ for each basis choice x for signal and y for idler; the $a, b = \{0, 1, 2\}$ correspond to the output channel used in the 3×3 splitter version of the projection. The α_x and β_y parameters relate to the measurement bases and are chosen as $\alpha_1 = 0$, $\alpha_2 = 1/2$, $\beta_1 = 1/4$ and $\beta_2 = -1/4$. These correspond to the measurement bases A_x and B_y discussed above and yield phase triplets $A_x = (0, (2\pi/3)\,\alpha_x, (4\pi/3)\,\alpha_x)$ and $B_y = (0, (2\pi/3)\,\beta_y, (4\pi/3)\,\beta_y)$. These are modified by the addition of phase triplets

$(0, (2\pi/3)\,a, (4\pi/3)\,a)$ and $(0, (-2\pi/3)\,b, (-4\pi/3)\,b)$ to signal and idler, respectively, in accord with the a and b parameters.

As our quantum state, we assume a density matrix of the form

$$\rho = \lambda \left|\psi\right\rangle \left\langle\psi\right| + (1-\lambda)\rho_N \tag{5.10}$$

with $0 \leq \lambda \leq 1$, where $\left|\psi\right\rangle$ is the maximally entangled state represented as:

$$\left|\psi\right\rangle = \frac{1}{\sqrt{3}}\big[\left|5,5\right\rangle_{SI} + \left|6,6\right\rangle_{SI} + \left|7,7\right\rangle_{SI}\big] \tag{5.11}$$

and ρ_N is our particular noise model, taken to be symmetric, or white:

$$\begin{aligned}\rho_N = \frac{1}{9}\big[&\left|5,5\right\rangle\left\langle 5,5\right|_{SI} + \left|5,6\right\rangle\left\langle 5,6\right|_{SI} + \left|5,7\right\rangle\left\langle 5,7\right|_{SI} + \left|6,5\right\rangle\left\langle 6,5\right|_{SI} + \left|6,6\right\rangle\left\langle 6,6\right|_{SI} \\ &+ \left|6,7\right\rangle\left\langle 6,7\right|_{SI} + \left|7,5\right\rangle\left\langle 7,5\right|_{SI} + \left|7,6\right\rangle\left\langle 7,6\right|_{SI} + \left|7,7\right\rangle\left\langle 7,7\right|_{SI}\big]\end{aligned} \tag{5.12}$$

In the three-dimensional case, ρ is a 9×9 matrix and ρ_N indicates only noise elements on the diagonal terms with the same amplitude. This is called a white noise model due to the fact that it is considering equal noise elements are added to the ideal density matrix in a non-correlated way. Correlated noise is neglected here, which is when the noise added to one state is related to the noise in other states, causing nonzero elements on the non-diagonal terms of the noise's density matrix. Following the discussion surrounding Eqs. 5.8 and 5.9, the projective measurements done on each photon are:

$$\Pi_S^x(a) = \frac{1}{3}\left[\left|5\right\rangle_S + e^{i\phi_S^x(a)}\left|6\right\rangle_S + e^{i2\phi_S^x(a)}\left|7\right\rangle_S\right]\left[\left\langle 5\right|_S + e^{-i\phi_S^x(a)}\left\langle 6\right|_S + e^{-i2\phi_S^x(a)}\left\langle 7\right|_S\right] \tag{5.13}$$

$$\Pi_I^y(b) = \frac{1}{3}\left[\left|5\right\rangle_I + e^{i\phi_I^y(b)}\left|6\right\rangle_I + e^{i2\phi_I^y(b)}\left|7\right\rangle_I\right]\left[\left\langle 5\right|_I + e^{-i\phi_I^y(b)}\left\langle 6\right|_I + e^{-i2\phi_I^y(b)}\left\langle 7\right|_I\right] \tag{5.14}$$

Therefore, the probabilities measured are given by:

$$\begin{aligned} P^{xy}(a,b) &= \mathrm{Tr}\left\{\rho\,\Pi_S^x(a)\otimes\Pi_I^y(b)\right\} \\ &= \lambda\big\langle\psi\big|\Pi_S^x(a)\otimes\Pi_I^y(b)\big|\psi\big\rangle + \frac{1-\lambda}{9}\sum_{m=5}^{7}\sum_{n=5}^{7}\big\langle mn\big|\Pi_S^x(a)\otimes\Pi_I^y(b)\big|mn\big\rangle_{SI} \end{aligned} \tag{5.15}$$

The noise matrix elements all evaluate to

$$\big\langle mn\big|\Pi_S^x(a)\otimes\Pi_I^y(b)\big|mn\big\rangle_{SI} = \frac{1}{9} \tag{5.16}$$

and the first term in Eq. (5.15) reduces to

$$\big\langle\psi\big|\Pi_S^x(a)\otimes\Pi_I^y(b)\big|\psi\big\rangle = \frac{1}{27}\left|1+e^{i\left[\phi_S^x(a)+\phi_I^y(b)\right]}+e^{i2\left[\phi_S^x(a)+\phi_I^y(b)\right]}\right|^2 \tag{5.17}$$

Combined, Eqs. 5.16 and 5.17 justify the simplification from a full 24-term Bell parameter to the 8-term I_3 in Eq. 5.7, which is based on symmetries in the combinations of outcomes a and b. The noise terms show no dependence on a and b (Eq. 5.16), while the pure state contribution (Eq. 5.17) varies only via the difference $(a-b)$ modulo 3 since $\Phi_{S_k}^x(a)+\Phi_{I_k}^y(b)=\frac{2\pi}{3}(k-5)(a-b+\alpha_k+\beta_k)$. Thus, under our particular noise model, we only need to obtain 8 probability estimates. This model is consistent with the measured JSI, which shows a roughly constant background on the off-diagonal terms within the two-qutrit subspace. (We note that a Bell test with no such symmetry assumptions would be possible by testing all 24 projections separately.)

Table 5.2.
Parameters for evaluations of the CGLMP inequality. The coincidences were measured in 10-minute spans; measurements were done three times to obtain standard deviations. To achieve the maximum and minimum number of coincidences, the phases of $\phi_S^x(a) = \phi_I^y(b) = 0$ and $\phi_S^x(a) = \phi_I^y(b) = \pi/3$ were put on the biphotons, respectively. To calculate each of the probabilities that appear in Eq. (5.7), the corresponding coincidence counts have to be divided by the maximum number of coincidences $P_{\max}(0,0)$.

Term	x	y	a	b	$\phi_S^x(a)$	$\phi_I^y(b)$	Coincidences
$P^{11}(0,0)$	1	1	0	0	0	$\pi/6$	150±10
$P^{21}(0,1)$	2	1	0	1	$\pi/3$	$-\pi/2$	141±23
$P^{22}(0,0)$	2	2	0	0	$\pi/3$	$-\pi/6$	152±21
$P^{12}(0,0)$	1	2	0	0	0	$-\pi/6$	146±16
$P^{11}(0,1)$	1	1	0	1	0	$-\pi/2$	54±4
$P^{21}(0,0)$	2	1	0	0	$\pi/3$	$\pi/6$	33±6
$P^{22}(0,1)$	2	2	0	1	$\pi/3$	$-5\pi/6$	49±12
$P^{12}(1,0)$	1	2	1	0	$2\pi/3$	$-\pi/6$	32±10
$P_{\max}(0,0)$	-	-	0	0	0	0	160±18
$P_{\min}(0,0)$	-	-	0	0	$\pi/3$	$\pi/3$	15±13

In the Table 2, the first column corresponds to the individual terms in Eq. 5.7. Columns 6 and 7 evaluate Eqs. 5.8 and 5.9 to obtain the signal and idler phase parameters $\phi_S^x(a)$ and $\phi_I^y(b)$. Our coincidence data are given in column 8. We calculate $I_3 = 2.63 \pm 0.2$ which is more than three standard deviations away from the classical limit and indicates three-dimensional frequency-bin entanglement.

5.5 Frequency Domain Manipulation With SPDC

To validate our phase modulation scheme, we used the same approach to prove frequency-bin entanglement for our SPDC source [20, 53]. Frequency-bin entanglement for such a source has been previously proven in [39, 40]. Our experimental setup is depicted in Fig. 5.8 and the illustration of the spectrum after each step in the setup is shown in 5.9.

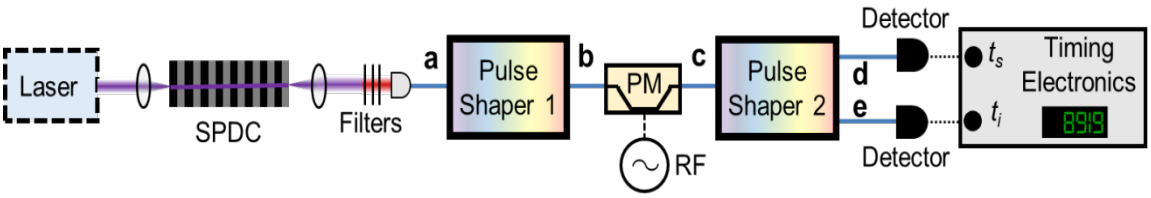

Fig. 5.8. Experimental setup for frequency-bin entanglement with SPDC.

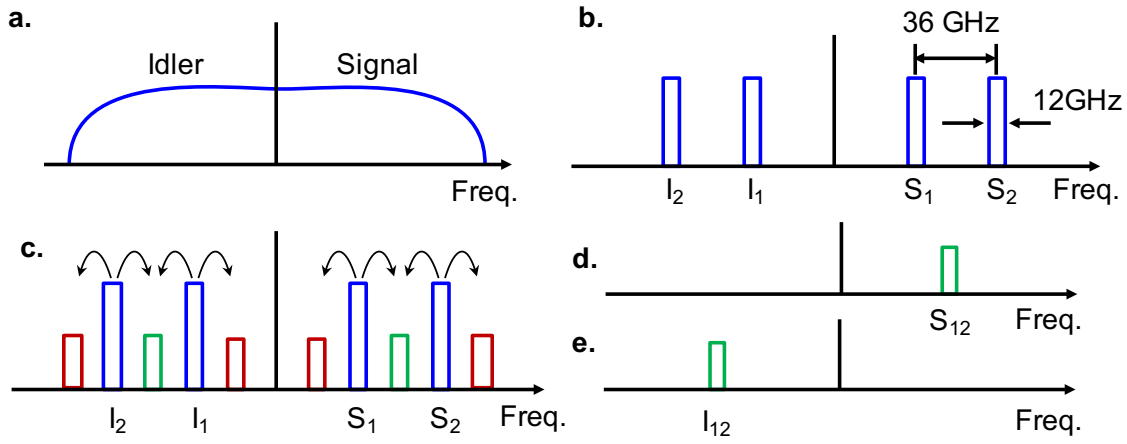

Fig. 5.9. Illustration of the spectrum after each step for Fig. 5.8.

In fact, conducting this experiment using a BFC carved out with a pulse shaper is easier than the microring case because of the wider linewidth of the frequency bins (12 GHz); therefore, it is easier to overlap the frequency bins after phase modulation.

Following the same approach as in Section 6.2, we are able to extract two-dimensional interference patterns for three comb line pairs with high visibilities, proving the phase coherence between them (Fig. 5.10).

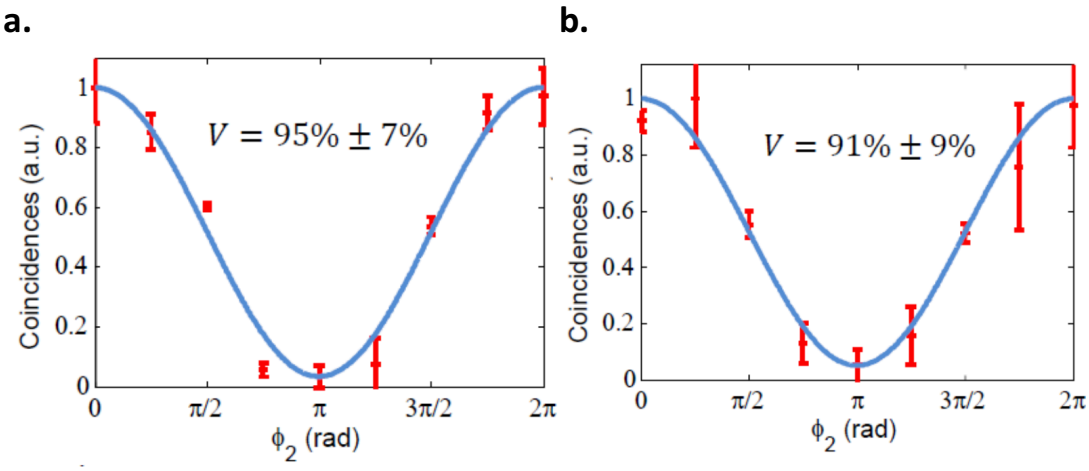

Fig. 5.10. Interference patterns for two-dimensional frequency-bin entanglement between a. comb line pairs 1 and 2 and b. comb line pairs 2 and 3. Here, ϕ_2 is the relative phase of the second comb line pair with respect to a. first and b. third comb line pair.

To prove three-dimensional phase coherence, we take the same approach as in Section 6.4, measuring the interference pattern shown in Fig. 5.11. The agreement of this measurement with theory (blue curve in Fig. 5.11), shows strong phase coherence between these comb line pairs.

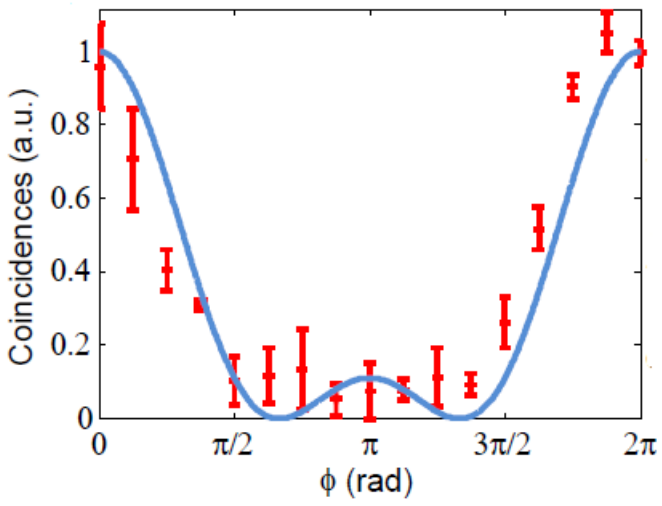

Fig. 5.11. Interference pattern for three-dimensional frequency-bin entanglement.

Moreover, the versatility of our experimental technique facilitates the measurement of dispersion using entangled photons. We insert some SMF-28e fiber before pulse shaper 1 to induce dispersion on the biphotons (Fig. 5.12)–the dispersion of this fiber around 1550 nm (extracted from the datasheet) is $D = 16.2\,\mathrm{ps/(nm\ km)}$ and $\beta_2 = -D\lambda^2/2\pi c = -2.06 \times 10^{-2}\,\mathrm{ps^2/m}$ [54]. Now we revisit the $d = 2$ interference results shown in Figs. 5.10a,b. Fiber dispersion will impart an additional relative phase on the $(k+1)^{th}$ bin with respect to the k^{th}, and this will lead to a phase shift in the interference pattern. The phase shift is given by

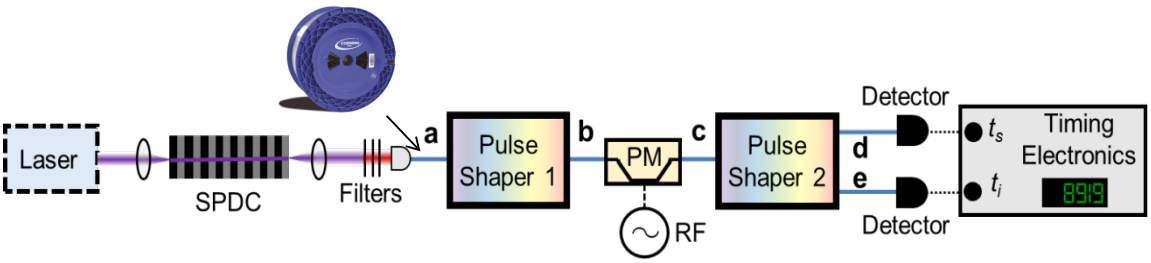

Fig. 5.12. Experimental setup for dispersion shift in the interference pattern.

$$\phi_{\text{shift}} = -(2\pi)^2\beta_2 l[(f_{\text{os}} + \Delta f)^2 - f_{\text{os}}^2] = -(2\pi)^2\beta_2 l\Delta f(2f_{\text{os}} + \Delta f) \tag{5.18}$$

where l is the fiber length, $\Delta f = \Delta\omega/2\pi$ is the FSR in Hz, $f_{\text{os}} = k\Delta f$ is the frequency difference between the k^{th} frequency bin and the center frequency, and we have assumed the dominant dispersion is the quadratic spectral phase term. Unlike the classical term, a factor of 1/2 is dropped in Eq. 5.18 since the total phase shift is sum of relative phase shifts in the signal and idler comb lines. As an initial experimental test, we use a fiber length of 200 m and select comb line pairs S_5I_5 and S_6I_6. Similar to previous measurements, after phase modulation, we pick out the sidebands S_{56} between S_5 and S_6, and I_{56} between I_5 and I_6, and then record the coincidence counts as we sweep ϕ_5 from 0 to 2π. The result, given in Fig. 5.13b, shows a sinusoidal interference pattern albeit shifted by a phase of 0.74π, in excellent agreement with theory (using Eq. 5.18 with $k = 5$ and $\Delta f = 36$ GHz).

For a complete frequency-dependent phase shift measurement, we replace the 200-m-long fiber with another fiber, 1.1 km long. However, rather than sweep ϕ_k for each f_{os}, we set it to zero and only register the coincidence counts as a function of f_{os} (Fig. 5.14a). We can then compute the phase shift for each f_{os} by comparing its corresponding coincidence counts, $C(f_{\text{os}})$, to the expected maximum number of coincidences C_{max}. By measuring the same single photon count rates in the selected frequency bins, we ensure that C_{max} is constant as a function of f_{os}. The phase shift

will be given by $C(f_{\text{os}}) = \frac{C_{\text{max}}}{2}[1 + cos(\phi_{\text{shift}})]$, which we can unwrap to obtain the linear plot in Fig. 5.14b. From Fig. 5.14b, β_2 can be retrieved by calculating the slope of the curve (derivative of ϕ_{shift} with respect to f_{os} in Eq. 5.18). We obtain a value of $\beta_2 = (-2.030 \pm 0.013) \times 10^{-2}\,\text{ps}^2/\text{m}$, not far off the $-2.06 \times 10^{-2}\,\text{ps}^2/\text{m}$ expected for SMF-28e fiber.

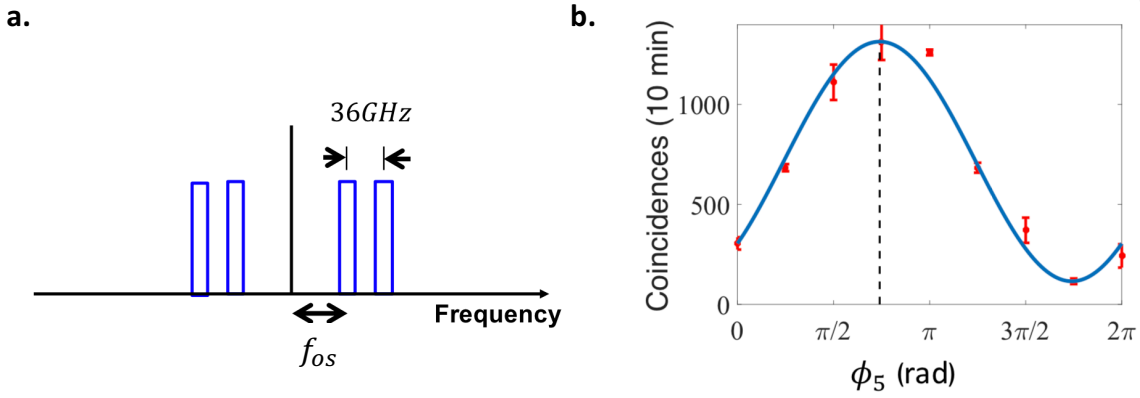

Fig. 5.13. a. Illustration of the comb line pairs. b. Dispersion shift in the interference pattern; the dashed vertical line shows $\phi_5 = 0.74\pi$

.

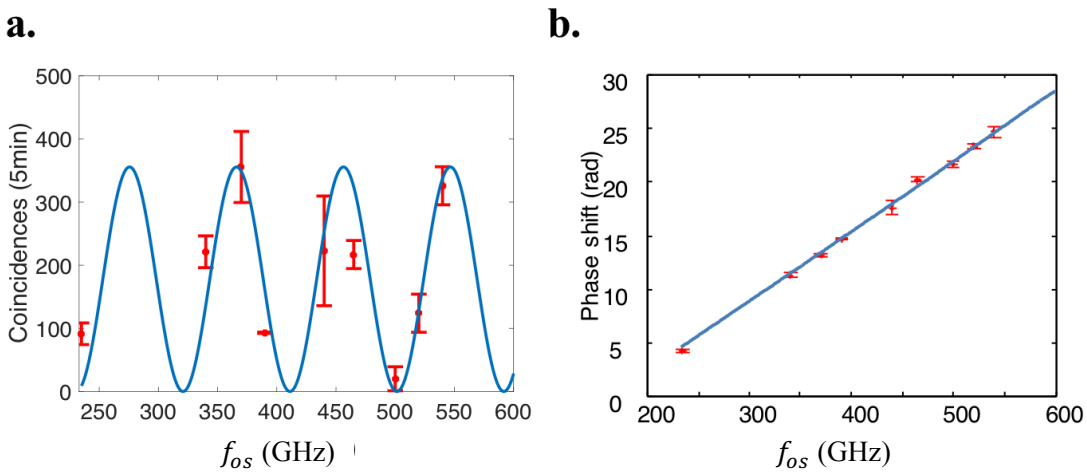

Fig. 5.14. a. Coincidences as a function of f_{os}. b. Phase shift of the interference pattern as a function of f_{os}.

.

5.6 Conclusion

In conclusion, we have demonstrated a technique for verifying phase coherence in BFCs. The attributes of this approach, in which we mix adjacent frequency bins, are analogous to those of Franson interferometry, which mixes entangled photon time bins. Equivalently, our approach provides a straightforward path to prove frequency-bin entanglement; we presented interference patterns with visibilities higher than the classical threshold for entangled qubit and qutrit states. We note that modulating the pump beam and multi-line pumping of these sources can give rise to more complex entangled states which can be coherently controlled in both time and frequency domain [55, 56]. These results reinforce the potential of biphoton frequency combs as high-dimensional entangled states. Last, our dispersion measurements suggest the potential of low-light dispersion measurement with biphotons.

6. FREQUENCY-DOMAIN HONG-OU-MANDEL INTERFERENCE WITH LINEAR OPTICS

6.1 Introduction

Having a source of time-frequency entangled photons in hand, we show the potential of the frequency degree of freedom of our source for quantum information processing by carrying out one of the most fundamental quantum-mechanical experiments– namely the Hong-Ou-Mandel (HOM) effect. The HOM experiment can be used as a measure of indistinguishability between two bosonic states, which leads to a non-classical interference effect between them [57, 58]. When two identical photons simultaneously arrive at the input ports of a 50/50 beam splitter—simultaneous to within the inverse of the single-photon bandwidth—four outcomes are possible: **(Outcome I)** both photons get transmitted, **(Outcome II)** both photons get reflected, **(Outcome III)** the photon incident on input 1 of the beam splitter is transmitted while the photon in input 2 is reflected, and **(Outcome IV)** the photon in input 1 gets reflected while the photon in input 2 gets transmitted. For an unbiased beam splitter, the probability of observing both photons at two different outputs of the beam splitter (**Outcomes I** and **II**) disappears due to destructive interference between probability amplitudes of the photons both getting transmitted or reflected. This leads to photon bunching, meaning that the two photons always exit the beam splitter from the same port. The original work by Hong *et al.* [57] examined this phenomena using incident photons emanating from different spatial modes, while other properties of the photons, such as polarization, temporal and spectral modes, were identical; therefore, the concept of photon bunching in their example occurred in the spatial domain. Demonstration of the HOM interference has not been limited to photons, and has been shown with other bosonic particles such as atoms [59], phonons in trapped

ions [60] and plasmons [61]. The analogue of the HOM effect in fermions leads to anti-bunching as opposed to bunching in bosons, and it has been demonstrated using electrons [62] and massless Dirac fermions [63].

HOM interference is at the heart of a number of applications in quantum information processing. These applications span works such as the demonstration of fundamental optical quantum gates [8,64] necessary for quantum computation protocols [2], quantum communications [65,66], optimal quantum cloning [67] and quantum repeaters [68–70].

In this chapter, we demonstrate the photon bunching effect in a different degree of freedom, the frequency domain, where two photons in different spectral modes enter an unbiased frequency beam splitter, and at the output, they both wind up in one of the two possible output frequency modes, first proposed in [71] using strong pump beams and nonlinear interactions. Unlike prior demonstrations of frequency-domain HOM that relied on nonlinear processes to play the role of a frequency beam splitter [72, 73], in our experiment, we use an electro-optic phase modulator as a frequency beam splitter, which is a linear device in the sense that its characteristics are independent of the photon flux. Consequently, our approach, compared to the use of nonlinear media, does not produce noise photons, thereby giving us a potential for better signal-to-noise ratio in our measurements.

6.2 Theory

We employ an electro-optic phase modulator as the frequency-domain analogue to a spatial beam splitter. By driving the phase modulator with an rf signal of the form $e^{i\delta \sin \omega_m t}$, where ω_m is the modulation frequency and δ is the modulation depth, each frequency bin projects into sidebands offset from the original center frequency by integer multiples of ω_m [74, 75]. Recently, electro-optic phase modulators have grown increasingly popular for frequency shifting and manipulation of single photons

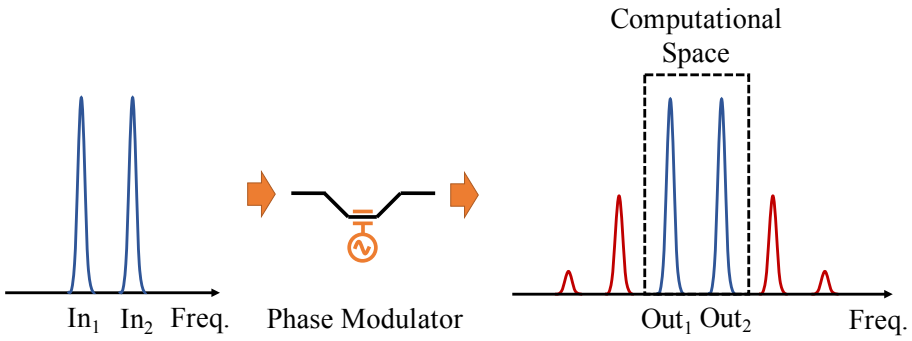

Fig. 6.1. Illustration of a phase modulator as a frequency beam splitter. In_1 and In_2 are the two input spectral modes to the beam splitter, and Out_1 and Out_2 are the two output modes. The red frequency bins at the output illustrate the undesired phase modulation sidebands that cause this scheme to be probabilistic.

[21, 42, 76–79]. After phase modulation, the complex amplitude of the n^{th} comb line with respect to the original frequency bin can be expressed as a Bessel function

$$C_n = J_n(\delta) \tag{6.1}$$

where $J_n(\delta)$ is the Bessel function of the first kind and $J_{-n}(\delta) = (-1)^n J_n(\delta)$. The scattering matrix representing the coupling coefficients between the two input and output modes can now be written in the form

$$S = \alpha \begin{pmatrix} \frac{1}{\sqrt{2}} & \frac{1}{\sqrt{2}} \\ \frac{1}{\sqrt{2}} & -\frac{1}{\sqrt{2}} \end{pmatrix} \tag{6.2}$$

Here, we assume the modulation index is chosen so that the values of $|J_n(\delta)|$ are equal for $n = -1, 0, 1$ and α accounts for transfer to other frequency modes outside of our computational space. We use two frequency-bins that are spaced from each other by the phase modulation frequency—these two spectral modes represent the inputs to our frequency beam splitter, as illustrated in Fig. 6.1. We are using the zero phase modulation sideband as the transmission and the ± 1 sidebands as the reflection ports

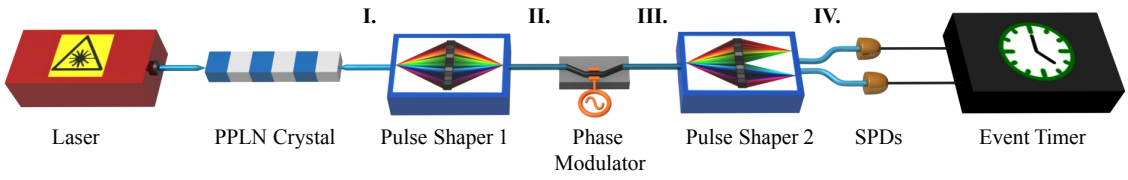

Fig. 6.2. Experimental setup. The Roman numerals are in reference to Fig. 6.3a.

of our frequency beam splitter. Looking at the same output spectral modes as the input modes shown as the computational space in Fig. 6.1, based on Eq. (6.1) we obtain that if the two input photons both get transmitted or reflected on our beam splitter, the relative phase between these two processes is π, very much like a spatial beam splitter. This proves that a phase modulator with these specified parameters can operate as a beam splitter in the frequency domain. The red frequency bins are the phase modulation sidebands that fall outside of our computational space, making this process probabilistic.

6.3 Experimental results

The experimental setup used for this experiment is the same as the setup used for the frequency-bin entanglement experiment with a PPLN crystal in section 6.5.The setup is depicted in Fig. 6.2 and an illustration of the spectrum at each step is provided in Fig. 6.3a. After generation of broadband time-frequency entangled photons, the biphoton spectrum is then carved with a commercial pulse shaper to select a pair of energy-correlated signal and idler frequency bins with a 10-GHz full width at half maximum. The line-shape of these frequency bins are the convolution of a rectangular band with a Gaussian resolution function ($\sim$10 GHz width). The center-to-center spacing between the two frequency bins is initially set to 22 GHz. The biphotons then pass through a phase modulator driven at a radio frequency of 22 GHz. We set the rf power such that the ± 1 phase modulation sidebands have the same power as the zero

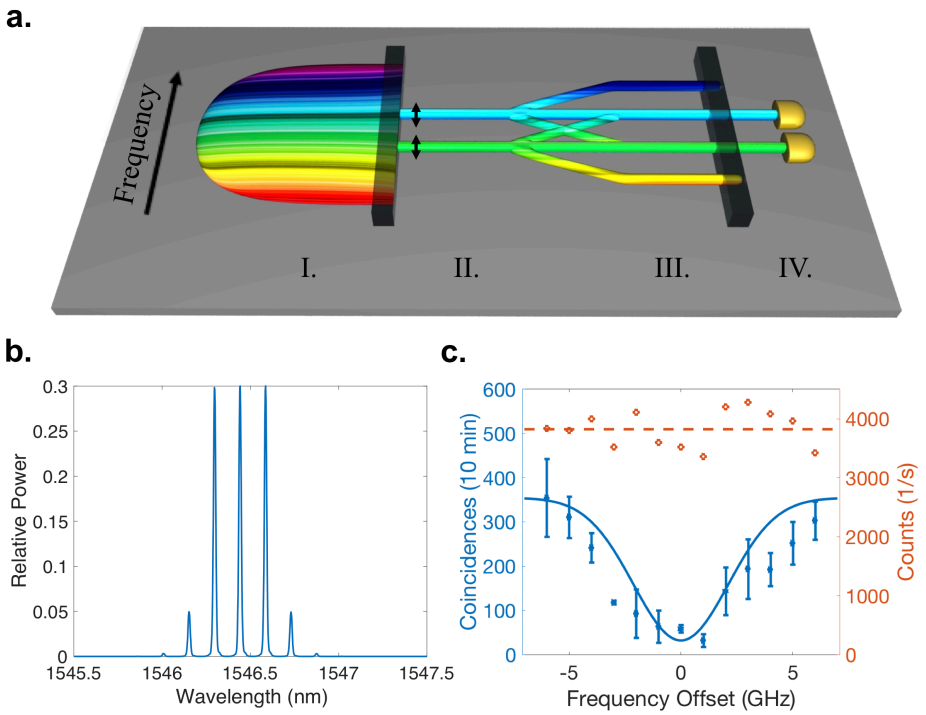

Fig. 6.3. a. Illustration of the spectrum at each stage of the experiment. b. The phase modulation spectrum of a single frequency mode. c. The HOM interference pattern in the frequency domain. The coincidences are shown in blue and the count rates on one of the single photon detectors are shown in orange. The blue error bars are the measured coincidences after accidentals subtraction. The subtracted accidentals were ∼700 in a 10 minute span. Each coincidence data point was measured three times to obtain the standard deviation indicated by the error bars. The blue curve is the theoretical HOM trace taking into account the 10 GHz wide signal and idler spectra of approximately Gaussian shape and the experimental visibility. The orange dashed line shows the average count rate.

sideband, making the projection probability of the photons onto these three sidebands equal; Fig. 6.3b is a trace of the resulting phase modulation spectrum tested with a CW test laser and an optical spectrum analyzer. This causes a projection of the signal photons on the idler frequency and vice versa. Another pulse shaper routes the signal and idler frequency bins to the SPDs.

Whenever a coincidence click appears, it must have come from a coherent superposition in which the signal and idler photons both stayed in their frequency bins during the phase modulation process (zero sideband) or they both swapped their frequency bins (± 1 sidebands). These two processes have a π phase shift with respect to each other due to the joint phase of the first sidebands with respect to the zero sideband. The terms in the two-photon state that contribute to detection of coincidences can now be written as

$$|\psi\rangle = |\text{stay, stay}\rangle_{SI} - |\text{swap, swap}\rangle_{SI} \tag{6.3}$$

The state is written in this way due to frequency indistinguishability between the $|(stay)\rangle$ and $|\text{swap}\rangle$ photons for both the signal and idler; therefore, if the amplitude of the two processes are the same (which we make sure of by equalizing the 0 and ± 1 phase modulation sidebands), no coincidences should be registered. Now, we repeat the measurement but with the first pulse shaper reprogrammed such that the spacings of both signal and idler frequency bins from the center of the spectrum vary from 5 GHz to 17 GHz in 1 GHz intervals. At all times, we send the signal frequency bin and $+1$ sideband of the idler frequency bin to one detector and the idler frequency bin along with the -1 sideband from the signal frequency bin to the other detector. As the frequency spacing differs from the modulation frequency (22 GHz), the sidebands are no longer indistinguishable, hence the coincidences start to rise. This dip in the HOM interference is observed in Fig. 6.3c in blue, with a visibility of $84\% \pm 2\%$ after accidentals subtraction, which is above the classical limit of 50% [57]. The frequency offset shown in Fig. 6.3c corresponds to the distance of the signal (idler) frequency bin from the center of the spectrum minus half of the phase modulation frequency. The count rates on one of the SPDs is also shown in Fig. 6.3c in orange, revealing the absence of single-photon interference in our measurement. The coincidence-to-accidental ratio was about 1:2, which is poor due to the insertion loss of the components.

6.4 Discussion

We note that the imperfection in the measured visibility is due to the low coincidence-to-accidental ratio in our experimental setup, which can be improved by utilizing a lower pump power albeit with a longer acquisition time. Unlike the nonlinear approaches proposed in [72] and [73] which use a pump to trigger frequency conversion, our frequency beam splitter does not contain a noise source and its performance does not suffer from multiphoton components. Therefore, our HOM interference visibility does not have a theoretical imperfect limit. We also note that the frequency beam splitter used in our setup is a probabilistic splitter, in the sense that there is a probability that photons get shifted to undesired sidebands (yellow and dark blue frequency bins in stage III. of Fig. 6.3a). This indicates that after phase modulation, there is a possibility that the photons end up outside of our computational basis. As can be seen in Fig. 6.3b, the transmission and reflectivity of our frequency beam splitter is 0.3 for the used phase modulator setting, so for a single photon, 0.6 of power goes into desired two frequency bins. Therefore, for two photons, we have a $(0.6)^2 = 0.36$ probability of both photons staying within computational space. In principle, this can be addressed by employing a more sophisticated frequency beam splitter design which retains photons within the computational space with almost 100% success probability. As proposed in [76] and demonstrated in [77, 79], instead of our single phase modulator probabilistic frequency beam splitter, a phase modulator–pulse shaper–phase modulator sequence can be used to achieve a nearly deterministic frequency beam splitter. However, from a practical perspective, using a single phase modulator has the advantage of lower insertion loss (by $\sim$7.5 dB) compared to the reported implementation of the deterministic splitter using discrete components. If the insertion loss is taken into account, the coincidence counts achieved with our single phase modulator frequency beam splitter should be roughly an order of magnitude higher than would be achieved with the deterministic beam splitter. On the other hand, photonic integration offers prospects for significantly reduced loss [21, 77]; if such im-

provements in implementation can be realized, the deterministic frequency splitter approach offers better generality to support scaling to more advanced operations.

Furthermore, the resolution of our data points is limited due to the 1 GHz addressability of the pulse shaper. An alternative is to sweep the phase modulation frequency instead of the spacing between the signal and idler frequency bins. The drawback of this method is that the phase modulation depth (δ) varies with the phase modulation frequency in such a broad span (12 GHz). To ensure a constant modulation depth for each frequency value, the phase modulation spectrum will have to be adjusted by tweaking the rf power.

6.5 Conclusion

In summary, we used a probabilistic frequency beam splitter to demonstrate the Hong-Ou-Mandel interference between single-photons of different colors, using linear optical components. This experiment could contribute to frequency processing of biphoton frequency combs [21, 42], enabling optical quantum frequency gates and linear optical quantum computing protocols [7, 80] in the frequency domain [76].

7. DETERMINISTIC HIGH-DIMENSIONAL OPTICAL QUANTUM LOGIC USING MULTIPLE DEGREES OF FREEDOM IN A SINGLE PHOTON

7.1 Introduction

In this chapter, we show the potential of our quantum source for quantum computation by demonstrating quantum gates necessary for universal quantum computation– one of the most important applications of coherent quantum sources. Amongst the myriad quantum systems suitable for information processing, photons have the critical advantage of extremely low decoherence, with minimal interaction with their surrounding environment [81]. This isolation, however, has the downside of also making photon-photon interactions for two-qubit gates difficult and, with linear optics, inherently probabilistic. Such a situation poses a formidable roadblock for photonics in scaling up quantum computing. An intriguing answer to this problem is to encode multiple qubits in a single photon, by making use of different degrees of freedom [82, 83]. While this solution ultimately suffers from exponential resource scaling [84], it enables deterministic two-qubit gates and thus offers significant encoding potential in the current generation of quantum circuits. So far, though, experiments in this paradigm have utilized two-dimensional encoding per each degree of freedom, thus failing to exploit the full information capacity of single photons. By using high-dimensional states, qudits can be encoded in photonic time and frequency degrees of freedom using on-chip sources like microresonators, which can easily expand the Hilbert space in a scalable way. Here, we demonstrate the first high-dimensional, single-photon two-qudit gates in time and frequency bins. By exploiting fast optical switching, we realize the cyclic shift operation (generalized X gate) for three time bins and confirming coherence through an interference measurement. By incorporating the

frequency-bin degree of freedom as well, via heralded single photons from an on-chip microring resonator, we build on this X gate and implement the two-qudit controlled increment (CINC) and modulo sum (SUM) gates–either of which are sufficient, along with single-qudit operations, for universal quantum computing [85]. Our scheme thus shows the potential of deterministic optical quantum computing in high-dimensional Hilbert spaces for practical and compact quantum information processing.

7.2 Background

Quantum algorithms such as Deutsch-Jozsa [14], Shor's factoring [86] and Grover's search [15] show the power of quantum computation by solving these crucial problems considerably faster than any classical computer. Moreover, quantum computation promises to enable the simulation of complex quantum mechanical systems which are impossible to realize with our current computing infrastructure [16]. Quantum gates have been demonstrated in multiple platforms such as superconductors [87], ion traps [88], and different degrees of freedom in photons such as polarization [89], orbital angular momentum [9], time [90], and frequency [77]. Compared to other platforms, optical states have the advantages of low decoherence and suitability for long-distance communications, but two-qubit gates are probabilistic with standard linear optics and photon counting [7](Fig. 1b). To overcome this issue, encoding qubits in different degrees of freedom (DoFs) in a single photon has been demonstrated, where each DoF carries one qubit and, now, interactions between different qubits can be made deterministic [82, 83]. Even though in this case two and three-qubit operations can be executed with unity success probability, each DoF contains only one qubit, and the number of a photon's DoFs are limited; thus the size of the Hilbert space in which these deterministic transformations can happen is fairly moderate (e.g., an eight-dimensional Hilbert space has been demonstrated by encoding three qubits in three different DoFs of a single photon [83]).

In this chapter, we take advantage of the high dimensionality in two particular DoFs of a single photon–namely, time and frequency, which are both compatible with fiber optical transmission–to encode one qudit in each DoF. We consider multiple time bins and frequency bins; as long as the frequency spacing between different modes (Δf) and the time-bin spacing (Δt) are chosen such that they far exceed the Fourier transform limit (i.e., $\Delta f \Delta t \gg 1$) , we are able to manipulate the time and frequency DoFs independently in a hyper-encoding fashion, using concepts developed in time-division and wavelength-division multiplexing, respectively [91, 92]. In other words, each time-frequency mode pair constitutes a well-defined entity, or plaquette [91, 92], which is sufficiently separated from its neighbors to provide stable encoding (Fig. 7.1a). An analogous process is at work in the advanced optical modulation formats gaining adoption in modern digital communications, where many bits are encoded in a single symbol via modulation of canonically conjugate quadratures [93]. Since our single photons can potentially be generated in a superposition of many time and frequency bins, multiple qubits can be encoded in each DoF, making our proposed scheme a favorable platform for deterministic optical quantum computing algorithms on large Hilbert spaces.

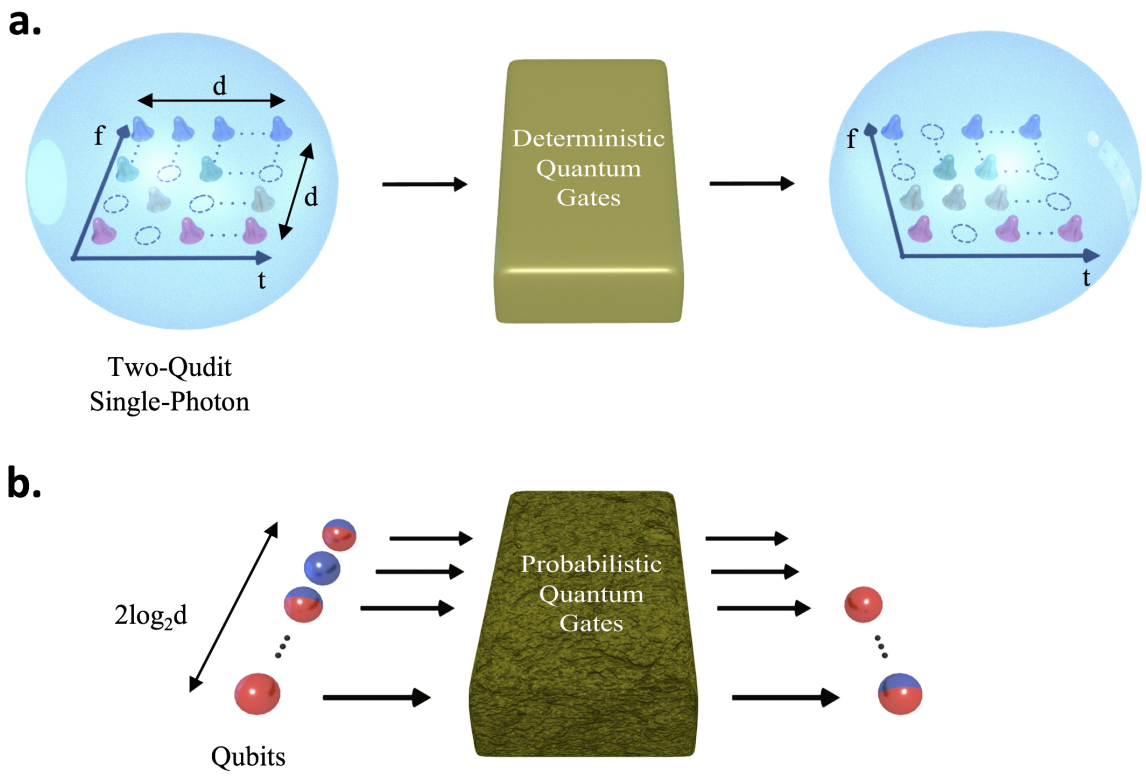

Fig. 7.1. Illustration of the scheme. a. Two qudits encoded in d time bins and frequency bins in a single photon, going through a deterministic quantum process. The single-photon can be encoded in an arbitrary superposition of different time and frequency bins; the unused time-frequency slots are shown with dashed circles. After the deterministic quantum process operates on the two-qudit state, the orientation of the time-frequency superpositions change to a new two-qudit state. b. 2log2d photons holding one qubit each (shown in blue and red colors) go through a probabilistic quantum process, which make the same Hilbert space size as the single photon in a. The input/output qubits can be in the states red, blue or a superposition of the two. In b. there is a possibility that the photons do not come out through the desired outputs, hence the first two output qubits are not shown (signifying gate failure).

7.3 Single-Qudit Cyclic Shift Gate

To show the capability of performing all single-qudit operations, it is sufficient to demonstrate the generalized Pauli gates X (cyclic shift) and Z (state-dependent

phase), which are universal for single-qudit operations [9], and from which all d-dimensional Weyl operators can be constructed [94]. The Z gate applies a unique phase shift to each of the basis states, which can be easily executed with a phase modulator and a pulse shaper in the time domain and frequency domain, respectively. Specifically, for the basis state $|n\rangle$ $(n = 0, 1, ..., d-1)$, we have $Z|n\rangle = exp(2\pi in/d)|n\rangle$. Here, we demonstrate the much more challenging X gate, which realizes the transformation $X|n\rangle = |n \oplus 1\rangle$, where $\oplus$ denotes addition modulo d. Our version, presented in Fig. 7.2a, operates on time bins in three dimensions, a process which corresponds to state-dependent delay. Because the gate operates on each photon individually, we can fully characterize its performance with coherent states; the statistics of the input field have no impact on the principle of operation. Accordingly, we use a CW laser and prepare the desired weak coherent state by carving out three time bins $\{|0\rangle_t, |1\rangle_t, |2\rangle_t\}$ using an intensity modulator and manipulating their relative phases with a phase modulator. The time bins are 3 ns wide and 6 ns apart from each other. To perform the X operation, we need to separate the time bins $|0\rangle$ and $|1\rangle$ from $|2\rangle$ and delay the route for time bins $|0\rangle$ and $|1\rangle$ by 3 bins (18 ns). We realize the necessary spatial separation between the time bins with an integrated Mach-Zehnder modulator (MZM) switch. We emphasize that while most MZM designs are one-port devices, with one of the two output paths terminated, this 1×2 version permits access to both interferometer outputs, and accordingly it is in principle lossless–as required for a unitary operation. (In practice, of course, insertion loss reduces throughput, but this is of a technical nature and not fundamental to the method.) After the path-dependent delay, another 1×2 MZM, but operated in reverse, can be used to recombine the time bins deterministically as well. However, due to lack of equipment availability, in this proof-of-principle experiment we employ a 2×2 fiber coupler for recombination, which introduces an additional 3 dB power penalty. For our measurement scheme, we synchronize a single photon detector and time interval analyzer with the generated time bins. The transformation matrix performed by the X gate when probed by single time bins is shown in Fig. 7.2b.

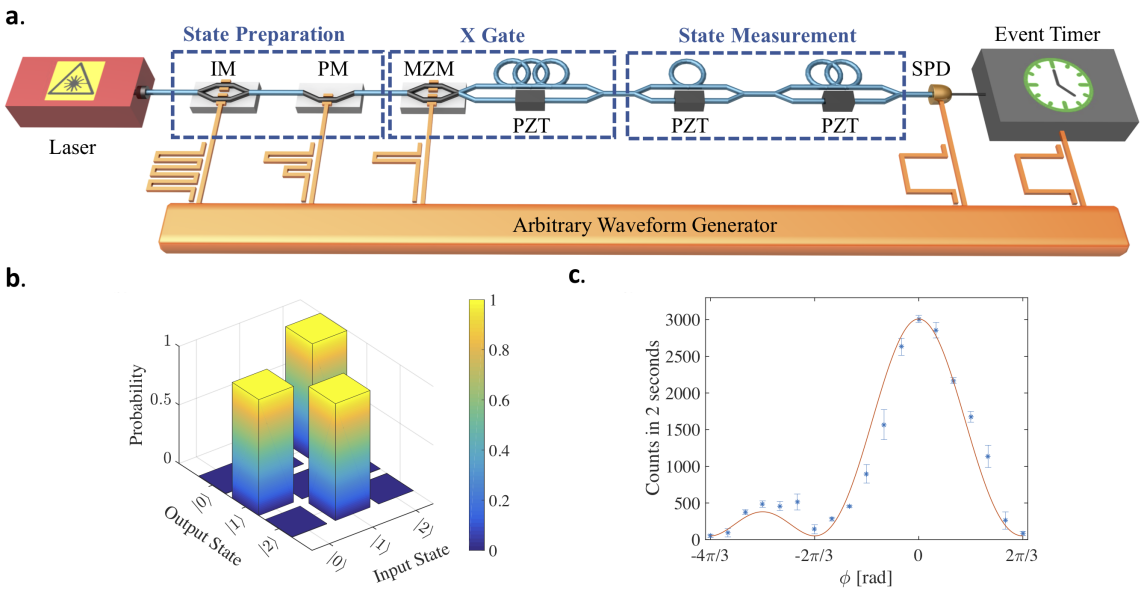

Fig. 7.2. a. Experimental setup of the state preparation, the X gate, and the state measurement. IM: intensity modulator. PM: phase modulator. MZM: Mach-Zehnder modulator PZT: piezo-electric phase shifter. The circle-shaped fibers indicate the delay; each circle is equivalent to one time-bin delay (6 ns). b. The transformation matrix. c. Counts measured after overlapping all three output time bins, for a time-bin superposition state input into the X gate. The blue errorbars are obtained from 5 measurements for each phase. The subtracted background was 200 about per 2 seconds.

To assess the performance of our quantum gate, we first focus on the computational-basis fidelity–one example of a so-called "classical" fidelity in the literature [95]. Defining $|n\rangle$ $(n = 0, 1, ..., N-1)$ as the set of all computational basis states and $|u_n\rangle$ as the corresponding output states for a perfect operation, we have the fidelity

$$\mathcal{F}_{\mathcal{C}} = \frac{1}{N}\sum_{n=0}^{N-1} p(u_n|n) \tag{7.1}$$

where $p(u_n|n)$ is the probability of measuring the output state $|u_n\rangle$ given an input of $|n\rangle$. In the operations considered here, the ideal output states $|u_n\rangle$ are members of the computational basis as well, so there is no need to measure temporal or spectral super-

positions in determination of $\mathcal{F}_{\mathcal{C}}$. Given the measured counts, we retrieve the N conditional probability distributions via Bayesian mean estimation (BME) [96,97],where our model assumes that each set of count outcomes (after accidentals subtraction) follows a multinomial distribution with to-be-determined probabilities; for simplicity, we take the prior distributions as uniform (equal weights for all outcomes). We then compute the mean and standard deviation of each value $p(u_n|n)$ and sum them to arrive at $\mathcal{F}_{\mathcal{C}}$. Specifically, if $C_{u_n|n}$ signifies the counts measured for outcome u_n, and $C_{tot|n}$ the total counts over all outcomes (both for a given input state $|n\rangle$), BME predicts (see Appendix C):

$$p(u_n|n) = \frac{1 + C_{u_n|n}}{N + C_{tot|n}} \pm \sqrt{\frac{1 + C_{u_n|n}}{(N + C_{tot|n})^2} \frac{N + C_{tot|n} - C_{u_n|n} - 1}{N + C_{tot|n} + 1}} \tag{7.2}$$

where the standard deviation in the estimate is used for the error. Since the probabilities here each actually come from N *different* distributions, we estimate the total error in $\mathcal{F}_{\mathcal{C}}$ by adding these constituent errors in quadrature. Using Eqs. 7.1 and 7.2, we obtain a computational-space fidelity of $\mathcal{F}_{\mathcal{C}} = 0.996 \pm 0.001$ for our X gate.

As such computational-basis-only measurements do not reflect the phase coherence of the operation, we next prepare superposition states as input and interfere the transformed time bins after the gate with a cascade of 1-bin and 2-bin delay unbalanced interferometers. In order to combat environmentally induced phase fluctuations, we stabilize both these interferometers and the X gate by sending a CW laser in the backwards direction and using a feedback phase control loop. We apply a phase of 0, ϕ and 2ϕ to the time-bins $|0\rangle_t$, $|1\rangle_t$ and $|2\rangle_t$, respectively, with the phase modulator in the state preparation stage and sweep from 0 to 2π, obtaining the interference pattern shown in Fig. 7.2c. After subtraction of the background, we calculate a visibility of 0.94 ± 0.01 from the maximum and minimum points, showing strong phase coherence (the ability to preserve and utilize coherent superpositions) between the time bins after the gate. If for concreteness we assume a channel model consisting of pure depolarizing (white) noise [94], we can use this visibility to esti-

mate the process fidelity $\mathcal{F}_P$ of our gate. To do so, we choose a test which–while limited–nonetheless offers strong evidence for the coherence of our time-bin X gate.

To begin with, note that all three-dimensional quantum process can be expressed in terms of the nine Weyl operations [98]:

$$U_0 = I = \begin{bmatrix} 1 & 0 & 0 \\ 0 & 1 & 0 \\ 0 & 0 & 1 \end{bmatrix} \quad U_1 = X = \begin{bmatrix} 0 & 0 & 1 \\ 1 & 0 & 0 \\ 0 & 1 & 0 \end{bmatrix} \quad U_2 = X^2 = \begin{bmatrix} 0 & 1 & 0 \\ 0 & 0 & 1 \\ 1 & 0 & 0 \end{bmatrix}$$

$$U_3 = Z = \begin{bmatrix} 1 & 0 & 0 \\ 0 & e^{i\frac{2\pi}{3}} & 0 \\ 0 & 0 & e^{-i\frac{2\pi}{3}} \end{bmatrix} \quad U_4 = ZX = \begin{bmatrix} 0 & 0 & 1 \\ e^{i\frac{2\pi}{3}} & 0 & 0 \\ 0 & e^{-i\frac{2\pi}{3}} & 0 \end{bmatrix} \quad U_5 = ZX^2 = \begin{bmatrix} 0 & 1 & 0 \\ 0 & 0 & e^{i\frac{2\pi}{3}} \\ e^{-i\frac{2\pi}{3}} & 0 & 0 \end{bmatrix}$$

$$U_6 = Z^2 = \begin{bmatrix} 1 & 0 & 0 \\ 0 & e^{-i\frac{2\pi}{3}} & 0 \\ 0 & 0 & e^{i\frac{2\pi}{3}} \end{bmatrix} \quad U_7 = Z^2X = \begin{bmatrix} 0 & 0 & 1 \\ e^{-i\frac{2\pi}{3}} & 0 & 0 \\ 0 & e^{i\frac{2\pi}{3}} & 0 \end{bmatrix} \quad U_8 = Z^2X^2 = \begin{bmatrix} 0 & 1 & 0 \\ 0 & 0 & e^{-i\frac{2\pi}{3}} \\ e^{i\frac{2\pi}{3}} & 0 & 0 \end{bmatrix} \tag{7.3}$$

The quantum process itself is a completely positive map $\mathcal{E}$ [99], meaning it sends positive elements to positive elements. It has been shown that maps between Hilbert spaces are completely positive [100]. For a given input density matrix $\hat{\rho_{in}}$, the quantum process outputs the state

$$\rho_{out} = \mathcal{E}(\rho_{in}) = \sum_{m,n=0}^{8} \chi_{mn} U_m \rho_{in} U_n^\dagger \tag{7.4}$$

The process matrix with elements χ_{mn} uniquely describes the operation. The ideal three-bin X gate with process matrix χ_X has only one nonzero value, $[\chi_X]_{11} = 1$. To compare to this ideal, we assume the actual operation consists of a perfect X gate plus depolarizing (white) noise [94]. In this case we have a total operation modeled as

$$\rho_{out} = \lambda U_1 \rho_{in} U_1^\dagger + \frac{(1-\lambda)}{3} \mathbb{I}_3 \tag{7.5}$$

whose process matrix we take to be $\chi_N = \lambda\chi_X + \frac{1-\lambda}{9}\mathbb{I}_9$. If we then assume a pure input superposition state $\rho_{in} = |\psi_{in}\rangle\langle\psi_{in}|$, where $\psi_{in} \propto |0\rangle_t + e^{i\phi}|1\rangle_t + e^{i2\phi}|2\rangle_t$, and measure the projection onto the output (as in Fig. 7.2c), λ can be estimated from the interference visibility as [30]

$$\lambda = \frac{2V}{3-V} \tag{7.6}$$

and the process fidelity can be estimated as:

$$\mathcal{F}_P = Tr\{\chi_X\chi_N\} = [\chi_N]_{11} = \frac{1+8\lambda}{9} = \frac{1+5V}{9-3V} = 0.92 \pm 0.01 \tag{7.7}$$

7.4 Two-Qudit Controlled-Gates

With this high-performance time-bin X gate in hand, we are then in a position to incorporate it into a frequency network to realize deterministic two-qudit gates, where the frequency DoF acts as the control and the time DoF is the target qudit. For this demonstration, instead of a weak coherent state, we utilize true single photons, heralded by detecting the partner photon of a frequency-bin entangled pair generated through spontaneous four-wave mixing in an on-chip silicon nitride microresonator. The time bins, defined by intensity modulation of the pump, couple into a microring with an FSR of 380 GHz, generating a biphoton frequency comb with mode spacing equal to this FSR. As our time-bin and frequency-bin spacings vastly exceed the Fourier transform limit ($\Delta f \Delta t = 2280 \gg 1$), our time-frequency entangled photons can be considered hyper-entangled–that is, entangled in two fully separable DoFs. The signal and idler photons from the first three comb line pairs are then selected and separated with a commercial pulse shaper, as shown in Fig. 7.4a. Now that the time bins and frequency bins are all generated in the state preparation stage, the idler photons are sent to a single photon detector to be used as heralding photons, and the signal photons are what carry the two-qudits in the three time bins $\{|0\rangle_t, |1\rangle_t, |2\rangle_t\}$ and frequency bins $\{|0\rangle_f, |1\rangle_f, |2\rangle_f\}$. This procedure lets us pre-

pare any time-bin/frequency-bin product state $|m\rangle_t |n\rangle_f$ $(m, n = 0, 1, 2)$ of the full computational basis set. In principle, we could also herald arbitrary time-frequency superposition states in this setup, by first sending the idler photon through a combination of time- or frequency-bin interferometers prior to detection in the temporal and spectral eigenbases. This more general case would permit the preparation of any two-qudit state and is an important area for further research.

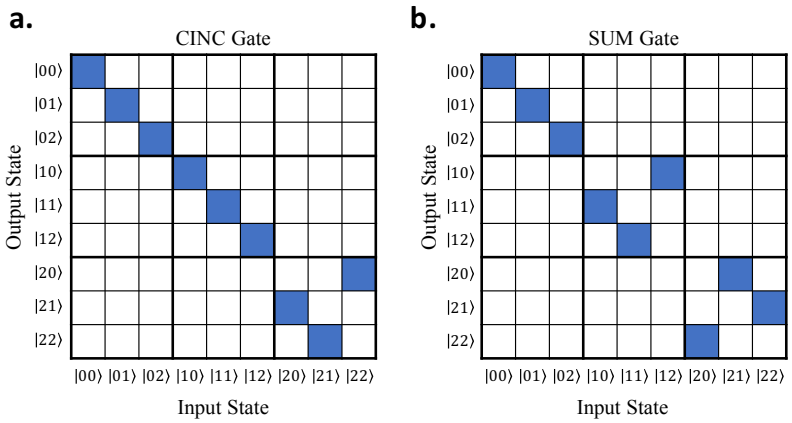

Fig. 7.3. Ideal transformation matrices for the two-qutrit a. CINC and b. SUM quantum gates. The first qutrit is the frequency-bin qutrit and the second qutrit is the time-bin qutrit. The blue squares show the ones and the white squares show the zeros in the transformation matrices.

As the first two-qudit gate, we demonstrate the controlled-increment (CINC) operation (Fig. 7.3a), where an X gate is applied to the time-bin qudit only when the frequency qudit is in the state $|2\rangle_f$. This two-qudit gate along with single qudit gates X and Z form a universal set of gates required for any quantum computing algorithm [85]. To implement this gate, we separate from the other two frequency bins with a DWDM filter and route it to a time-bin X gate (Fig. 7.4a); no operation happens on the route of the other two frequency bins. The frequency bins are then brought back together with another DWDM with zero relative delay to complete the two-qudit gate operation. To measure the transformation matrix of this gate in the

computational basis, we prepare the input state in each of the 9 combinations of single time bins and frequency bins, using the first intensity modulator and the pulse shaper, respectively. We then record the signal counts in all possible output time-bin/frequency-bin pairs, conditioned on detection of a particular idler time-frequency mode, by inserting three different DWDMs in the path of the signal photons to pick different frequency bins. The measured transformation matrix is shown in Fig. 7.4b, with accidental-subtracted fidelity $\mathcal{F}_{\mathcal{C}} = 0.90 \pm 0.01$, calculated using Eq. 7.1.

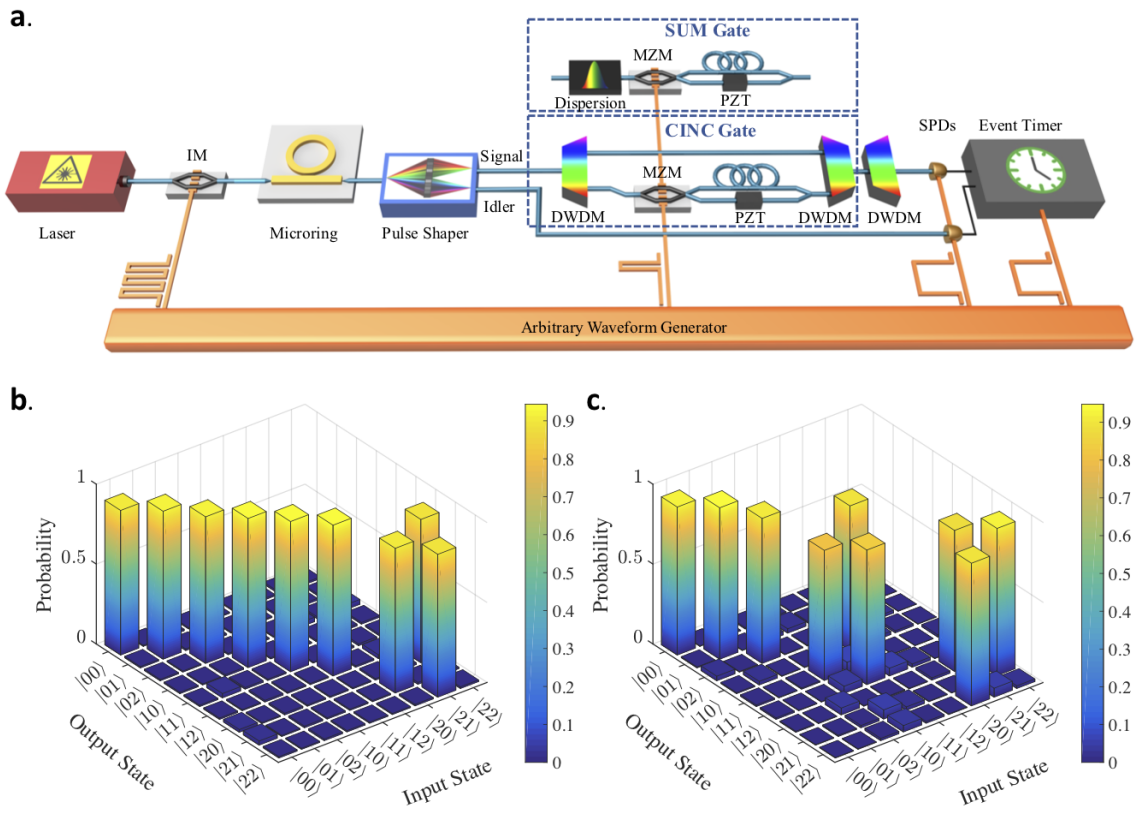

Fig. 7.4. a. Experimental setup for the CINC and SUM gate. The MZM for the CINC gate is driven such that it separates the time bin $|2\rangle_t$ from time bins $|0\rangle_t$ and $|1\rangle_t$. For the SUM gate, the MZM separates the time bins that fall outside of the computational space ($|3\rangle_t$ and $|4\rangle_t$) from the computational space time bins ($|0\rangle_t$, $|1\rangle_t$ and $|2\rangle_t$). DWDM: dense wavelength-division multiplexer. b. and c. The experimental transformation matrix of the CINC and SUM gate, respectively. The accidentals were subtracted in the transformation matrices, and the coincidence to accidentals ratio was ~ 3.7 in the CINC and ~ 3 in the SUM case.

For the next step, we implement an even more complex operation, the SUM gate–a generalized controlled-NOT gate [101]–which adds the value of the control qudit to the value of the target qudit, modulo 3 (Fig. 7.3b). In this gate, the time bins associated with $|0\rangle_f$ are not delayed, the time bins associated with $|1\rangle_f$ experience a cyclic shift by 1 slot, and the time bins corresponding to $|2\rangle_f$ go through a cyclic shift of 2 slots. To delay the time bins dependent of their frequencies, we induce

a dispersion of -2 ns/nm on the photons using a CFBG; this imparts 6-ns (1-bin) and 12-ns (2-bin) delays for the temporal modes of $|1\rangle_f$ and $|2\rangle_f$, respectively, as required for the SUM operation. However, this delay is linear–not cyclic–so that some of the time bins are pushed outside of the computational space, to modes $|3\rangle_f$ and $|4\rangle_f$. Returning these bins to overlap with the necessary $|0\rangle_f$ and $|1\rangle_f$ slots can be achieved using principles identical to the time-bin X gate with a relative delay of three bins. The experimental setup is shown in Fig. 7.4a, where we use the same techniques as for the CINC gate to measure the transfer matrix shown in Fig. 7.4c, with $\mathcal{F}_{\mathcal{C}} = 0.92 \pm 0.01$. The fact that this SUM gate is implemented with qudits in a single step potentially reduces the complexity and depth of quantum circuits in all the algorithms that require an addition operation [102]. We note that to enhance computational capabilities, it would be valuable to also develop two-qudit operations where instead time bins are the control qudit and frequency bins the target qudit which would then require active frequency shifting conditioned on time bins.

7.5 Discussion

Hyper-entangled time-frequency entangled states, as opposed to other high-dimensional optical degrees of freedom like orbital angular momentum, can be generated in integrated on-chip sources, which have gained tremendous attention in recent years due to their low cost, room temperature operation, compatibility with CMOS foundries and the ability to be integrated with other optical components. These two degrees of freedom can be extended to much higher dimensions as well; in the frequency domain, a 50 GHz spaced biphoton frequency comb has been demonstrated with more than 40 frequency mode pairs [21]. For such a frequency spacing, independent time bins can be placed as close as ∼20 ps to each other based on Heisenbergs limit, implying ∼50 modes available for encoding within a single nanosecond, limited only by detector timing resolution. Manipulating the frequency bins in both phase and delay should become possible with an on-chip pulse shaper [103], removing the need for

large dispersion modules like a CFBG. In addition, demonstration of balanced and unbalanced interferometers on-chip eliminates the need for active stabilization, which is of considerable profit for the scalability of the scheme [104]. These contributions can potentially lead to combining these sources with on-chip phase modulators, switches and pulse shapers to create the whole quantum computing process on an integrated circuit.

7.6 Conclusion

High-dimensional optical states [21, 42, 104–106] can open the door to deterministically carry out various quantum computing algorithms in large Hilbert spaces [107]. We have demonstrated deterministic single and two-qudit gates using the time and frequency degrees of freedom of a single photon to encode the qudits, and carried out theses gates with a high computational space fidelity. Such demonstrations of deterministic quantum gates [108] add significant value to the photonic platform for near-term quantum computing.

8. CONCLUSION

Entangled photons are the heart of many applications in the field of quantum information processing [109]. I this thesis, we utilized both bulk and on-chip sources to generate time-frequency entangled photons, exhibiting the shape of a comb in the frequency domain. We then manipulated these high-dimensional entangled states in both the time and frequency domain. We provided proof-of-principle experiments in the time domain such as Franson interferometry to show time-bin entanglement between our photon pairs and nonlocal dispersion cancellation to show the potential of our source for secure quantum communications [19]. We then presented a frequency-domain manipulation scheme–analogous to Franson interferometry in the time domain–using pulse shapers and electro-optic modulators to show the high-dimensional frequency-bin entanglement of our source [20,21]. We then showed the potential of the frequency degree of freedom for encoding and manipulating information coherently by showing a fundamental quantum mechanical effect, the Hong-Ou-Mandel interference in the frequency domain [22]. Having an on-chip time-frequency entangled source in hand, we then showed the potential of of scheme for universal quantum computation by showing elementary high-dimensional controlled-gates utilizing two degrees of freedom in a single photon–namely the time and frequency degrees of freedom [17]. Our quantum sources can be used in quantum communication protocols such as quantum key distribution [18] and high-dimensional quantum teleportation [110, 111]. As the frequency degree of freedom of light is robust and more immune to noise in standard fiber-optical communication links, we are presenting a favorable platform for communication proposes. In addition, by integrating our quantum state manipulation techniques on a chip, our scheme paves the way for high-dimensional quantum computation, which can help with solving crucial problems exponentially faster than classical computers [86] and simulate complex quantum-mechanical systems [16].

REFERENCES

REFERENCES

[1] M. A. Nielsen and I. L. Chuang, *Quantum computation and quantum information*. Cambridge University Press, 2010.

[2] A. Steane, "Quantum computing," *Reports on Progress in Physics*, vol. 61, no. 2, p. 117, 1998.

[3] P. Walther, K. J. Resch, T. Rudolph, E. Schenck, H. Weinfurter, V. Vedral, M. Aspelmeyer, and A. Zeilinger, "Experimental one-way quantum computing," *Nature*, vol. 434, no. 7030, pp. 169–176, 2005.

[4] P. W. Shor and J. Preskill, "Simple proof of security of the bb84 quantum key distribution protocol," *Physical review letters*, vol. 85, no. 2, p. 441, 2000.

[5] J. T. Barreiro, T.-C. Wei, and P. G. Kwiat, "Beating the channel capacity limit for linear photonic superdense coding," *Nature physics*, vol. 4, no. 4, pp. 282–286, 2008.

[6] V. Giovannetti, S. Lloyd, and L. Maccone, "Quantum metrology," *Physical review letters*, vol. 96, no. 1, p. 010401, 2006.

[7] E. Knill, R. Laflamme, and G. J. Milburn, "A scheme for efficient quantum computation with linear optics," *Nature*, vol. 409, no. 6816, pp. 46–52, 2001.

[8] J. L. O'Brien, G. J. Pryde, A. G. White, T. C. Ralph, and D. Branning, "Demonstration of an all-optical quantum controlled-not gate," *Nature*, vol. 426, no. 6964, pp. 264–267, 2003.

[9] A. Babazadeh, M. Erhard, F. Wang, M. Malik, R. Nouroozi, M. Krenn, and A. Zeilinger, "High-dimensional single-photon quantum gates: Concepts and experiments," *Phys. Rev. Lett.*, vol. 119, no. 18, p. 180510, 2017.

[10] B. P. Lanyon, M. Barbieri, M. P. Almeida, T. Jennewein, T. C. Ralph, K. J. Resch, G. J. Pryde, J. L. Obrien, A. Gilchrist, and A. G. White, "Simplifying quantum logic using higher-dimensional hilbert spaces," *Nature Physics*, vol. 5, no. 2, pp. 134–140, 2009.

[11] Z. Xie, T. Zhong, S. Shrestha, X. Xu, J. Liang, Y.-X. Gong, J. C. Bienfang, A. Restelli, J. H. Shapiro, W. N. C., and C. Wei Wong, "Harnessing high-dimensional hyperentanglement through a biphoton frequency comb," *Nature Photonics*, vol. 9, no. 8, pp. 536–542, 08 2015.

[12] L. Sheridan and V. Scarani, "Security proof for quantum key distribution using qudit systems," *Physical Review A*, vol. 82, no. 3, p. 030301, 2010.

[13] P. W. Shor, "Algorithms for quantum computation: Discrete logarithms and factoring," in *Foundations of Computer Science, 1994 Proceedings., 35th Annual Symposium on*. Ieee, 1994, pp. 124–134.

[14] D. Deutsch and R. Jozsa, "Rapid solution of problems by quantum computation," *Proc. R. Soc. Lond. A*, vol. 439, no. 1907, pp. 553–558, 1992.

[15] L. K. Grover, "Quantum mechanics helps in searching for a needle in a haystack," *Physical review letters*, vol. 79, no. 2, p. 325, 1997.

[16] S. Somaroo, C. Tseng, T. Havel, R. Laflamme, and D. G. Cory, "Quantum simulations on a quantum computer," *Physical review letters*, vol. 82, no. 26, p. 5381, 1999.

[17] P. Imany, J. A. Jaramillo-Villegas, J. M. Lukens, O. D. Odele, D. E. Leaird, M. Qi, and A. M. Weiner, "Deterministic optical quantum logic with multiple high-dimensional degrees of freedom in a single photon," *arXiv preprint arXiv:1805.04410*, 2018.

[18] J. Mower, Z. Zhang, P. Desjardins, C. Lee, J. H. Shapiro, and D. Englund, "High-dimensional quantum key distribution using dispersive optics," *Physical Review A*, vol. 87, no. 6, p. 062322, 2013.

[19] J. A. Jaramillo-Villegas, P. Imany, O. D. Odele, D. E. Leaird, Z.-Y. Ou, M. Qi, and A. M. Weiner, "Persistent energy–time entanglement covering multiple resonances of an on-chip biphoton frequency comb," *Optica*, vol. 4, no. 6, pp. 655–658, 2017.

[20] P. Imany, O. D. Odele, J. A. Jaramillo-Villegas, D. E. Leaird, and A. M. Weiner, "Characterization of coherent quantum frequency combs using electro-optic phase modulation," *Physical Review A*, vol. 97, no. 1, p. 013813, 2018.

[21] P. Imany, J. A. Jaramillo-Villegas, O. D. Odele, K. Han, D. E. Leaird, J. M. Lukens, P. Lougovski, M. Qi, and A. M. Weiner, "50-GHz-spaced comb of high-dimensional frequency-bin entangled photons from an on-chip silicon nitride microresonator," *Optics Express*, vol. 26, no. 2, pp. 1825–1840, 2018.

[22] P. Imany, O. D. Odele, M. S. Alshaykh, H.-H. Lu, D. E. Leaird, and A. M. Weiner, "Frequency-domain hong–ou–mandel interference with linear optics," *Optics letters*, vol. 43, no. 12, pp. 2760–2763, 2018.

[23] L. G. Helt, M. Liscidini, and J. E. Sipe, "How does it scale? comparing quantum and classical nonlinear optical processes in integrated devices," *JOSA B*, vol. 29, no. 8, pp. 2199–2212, 2012.

[24] A. M. Weiner, "Femtosecond pulse shaping using spatial light modulators," *Review of Scientific Instruments*, vol. 71, no. 5, pp. 1929–1960, 2000.

[25] J. D. Franson, "Bell inequality for position and time," *Physical Review Letters*, vol. 62, no. 19, p. 2205, 1989.

[26] R. J. Glauber, "The quantum theory of optical coherence," *Physical Review*, vol. 130, no. 6, p. 2529, 1963.

[27] S. Ramelow, A. Farsi, S. Clemmen, D. Orquiza, K. Luke, M. Lipson, and A. L. Gaeta, "Silicon-nitride platform for narrowband entangled photon generation," *arXiv preprint arXiv:1508.04358*, 2015.

[28] C. Reimer, M. Kues, P. Roztocki, B. Wetzel, F. Grazioso, B. E. Little, S. T. Chu, T. Johnston, Y. Bromberg, L. Caspani, D. J. Moss, and R. Morandotti, "Generation of multiphoton entangled quantum states by means of integrated frequency combs," vol. 351, no. 6278, pp. 1176–1180, 2016.

[29] F. Mazeas, M. Traetta, M. Bentivegna, F. Kaiser, D. Aktas, W. Zhang, C. A. Ramos, L. A. Ngah, T. Lunghi, E. Picholle, N. Belabas-Plougonven, X. L. Roux, E. Cassan, D. Marris-Morini, L. Vivien, G. Sauder, L. Labonté, and S. Tanzilli, "High-quality photonic entanglement for wavelength-multiplexed quantum communication based on a silicon chip," *Optics Express*, vol. 24, no. 25, pp. 28 731–28 738, Dec 2016.

[30] R. T. Thew, A. Acin, H. Zbinden, and N. Gisin, "Bell-type test of energy-time entangled qutrits," *Physical Review Letters*, vol. 93, no. 1, p. 010503, 2004.

[31] A. Eckstein, G. Boucher, A. Lemaître, P. Filloux, I. Favero, G. Leo, J. E. Sipe, M. Liscidini, and S. Ducci, "High-resolution spectral characterization of two photon states via classical measurements," *Laser & Photonics Reviews*, vol. 8, no. 5, pp. L76–L80, 2014.

[32] I. Jizan, A. Clark, L. Helt, M. Collins, E. Mägi, C. Xiong, M. Steel, and B. Eggleton, "High-resolution measurement of spectral quantum correlations in the telecommunication band," *Optics Communications*, vol. 327, pp. 45–48, 2014.

[33] C. Law and J. Eberly, "Analysis and interpretation of high transverse entanglement in optical parametric down conversion," *Physical review letters*, vol. 92, no. 12, p. 127903, 2004.

[34] J. D. Franson, "Nonlocal cancellation of dispersion," *Physical Review A*, vol. 45, no. 5, p. 3126, 1992.

[35] C. Lee, Z. Zhang, G. R. Steinbrecher, H. Zhou, J. Mower, T. Zhong, L. Wang, X. Hu, R. D. Horansky, V. B. Verma, A. E. Lita, R. P. Mirin, F. Marsili, M. D. Shaw, S. W. Nam, G. W. Wornell, F. N. C. Wong, J. H. Shapiro, and D. Englund, "Entanglement-based quantum communication secured by nonlocal dispersion cancellation," *Physical Review A*, vol. 90, p. 062331, Dec 2014.

[36] A. Valencia, M. V. Chekhova, A. Trifonov, and Y. Shih, "Entangled two-photon wave packet in a dispersive medium," *Physical Review Letters*, vol. 88, no. 18, p. 183601, 2002.

[37] M. Krenn, M. Huber, R. Fickler, R. Lapkiewicz, S. Ramelow, and A. Zeilinger, "Generation and confirmation of a (100× 100)-dimensional entangled quantum system," *Proceedings of the National Academy of Sciences*, vol. 111, no. 17, pp. 6243–6247, 2014.

[38] Y. J. Lu, R. L. Campbell, and Z. Y. Ou, "Mode-locked two-photon states," *Physical Review Letters*, vol. 91, p. 163602, Oct 2003.

[39] L. Olislager, J. Cussey, A. T. Nguyen, P. Emplit, S. Massar, J.-M. Merolla, and K. P. Huy, "Frequency-bin entangled photons," *Physical Review A*, vol. 82, no. 1, p. 013804, 2010.

[40] C. Bernhard, B. Bessire, T. Feurer, and A. Stefanov, "Shaping frequency-entangled qudits," *Physical Review A*, vol. 88, no. 3, p. 032322, 2013.

[41] P. Imany, J. A. Jaramillo-Villegas, O. D. Odele, K. Han, M. Qi, D. E. Leaird, and A. Weiner, "Demonstration of frequency-bin entanglement in an integrated optical microresonator," in *CLEO: Science and Innovations*. Optical Society of America, 2017, pp. JTh5B–3.

[42] M. Kues, C. Reimer, P. Roztocki, L. R. Cortés, S. Sciara, B. Wetzel, Y. Zhang, A. Cino, S. T. Chu, B. E. Little *et al.*, "On-chip generation of high-dimensional entangled quantum states and their coherent control," *Nature*, vol. 546, no. 7660, pp. 622–626, 2017.

[43] J. M. Lukens and P. Lougovski, "Frequency-encoded photonic qubits for scalable quantum information processing," *Optica*, vol. 4, no. 1, pp. 8–16, Jan 2017.

[44] D. Collins, N. Gisin, N. Linden, S. Massar, and S. Popescu, "Bell inequalities for arbitrarily high-dimensional systems," *Physical review letters*, vol. 88, no. 4, p. 040404, 2002.

[45] D. F. James, P. G. Kwiat, W. J. Munro, and A. G. White, "Measurement of qubits," *Physical Review A*, vol. 64, no. 5, p. 052312, 2001.

[46] H. Takesue and Y. Noguchi, "Implementation of quantum state tomography for time-bin entangled photon pairs," *Optics express*, vol. 17, no. 13, pp. 10 976–10 989, 2009.

[47] Z. Hradil, "Quantum-state estimation," *Physical Review A*, vol. 55, no. 3, p. R1561, 1997.

[48] A. Peres, "Separability criterion for density matrices," *Phys. Rev. Lett.*, vol. 77, no. 8, p. 1413, 1996.

[49] M. Horodecki, P. Horodecki, and R. Horodecki, "Separability of mixed states: necessary and sufficient conditions," *Phys. Lett. A*, vol. 223, no. 1, pp. 1–8, 1996.

[50] C. Bernhard, B. Bessire, A. Montina, M. Pfaffhauser, A. Stefanov, and S. Wolf, "Non-locality of experimental qutrit pairs," *Journal of Physics A: Mathematical and Theoretical*, vol. 47, no. 42, p. 424013, 2014.

[51] M. Żukowski, A. Zeilinger, and M. A. Horne, "Realizable higher-dimensional two-particle entanglements via multiport beam splitters," *Phys. Rev. A*, vol. 55, pp. 2564–2579, Apr 1997. [Online]. Available: https://link.aps.org/doi/10.1103/PhysRevA.55.2564

[52] D. Kaszlikowski, L. C. Kwek, J.-L. Chen, M. Żukowski, and C. H. Oh, "Clauser-horne inequality for three-state systems," *Physical Review A*, vol. 65, no. 3, p. 032118, 2002.

[53] P. Imany, O. D. Odele, J. Jaramillo-Villegas, D. Leaird, and A. Weiner, "Two-photon interference with frequency-bin entangled photons," in *CLEO: QELS_Fundamental Science*. Optical Society of America, 2017, pp. FW1F–6.

[54] A. Weiner, *Ultrafast Optics*, 1st ed. Wiley, 6 2009.

[55] O. D. Odele, J. M. Lukens, **J. A. Jaramillo-Villegas**, P. Imany, C. Langrock, M. M. Fejer, D. E. Leaird, and A. M. Weiner, "High-speed switching of biphoton delays through electro-optic pump frequency modulation," *APL Photonics*, vol. 2, no. 1, p. 011301, 2017.

[56] P. Imany, O. D. Odele, J. A. Jaramillo-Villegas, M. Qi, D. E. Leaird, and A. M. Weiner, "Coherent quantum control of on-chip time-frequency entangled photons," in *CLEO: Science and Innovations*. Optical Society of America, 2017, pp. JW2A–25.

[57] C. Hong, Z.-Y. Ou, and L. Mandel, "Measurement of subpicosecond time intervals between two photons by interference," *Physical Review Letters*, vol. 59, no. 18, p. 2044, 1987.

[58] J.-W. Pan, Z.-B. Chen, C.-Y. Lu, H. Weinfurter, A. Zeilinger, and M. Żukowski, "Multiphoton entanglement and interferometry," *Reviews of Modern Physics*, vol. 84, no. 2, p. 777, 2012.

[59] R. Lopes, A. Imanaliev, A. Aspect, M. Cheneau, D. Boiron, and C. I. Westbrook, "Atomic hong–ou–mandel experiment," *Nature*, vol. 520, no. 7545, p. 66, 2015.

[60] K. Toyoda, R. Hiji, A. Noguchi, and S. Urabe, "Hong–ou–mandel interference of two phonons in trapped ions," *Nature*, vol. 527, no. 7576, p. 74, 2015.

[61] J. S. Fakonas, H. Lee, Y. A. Kelaita, and H. A. Atwater, "Two-plasmon quantum interference," *Nature Photonics*, vol. 8, no. 4, p. 317, 2014.

[62] T. Jonckheere, J. Rech, C. Wahl, and T. Martin, "Electron and hole hong-ou-mandel interferometry," *Physical Review B*, vol. 86, no. 12, p. 125425, 2012.

[63] M. Khan and M. N. Leuenberger, "Two-dimensional fermionic hong-ou-mandel interference with massless dirac fermions," *Physical Review B*, vol. 90, no. 7, p. 075439, 2014.

[64] T. C. Ralph, N. K. Langford, T. Bell, and A. White, "Linear optical controlled-not gate in the coincidence basis," *Physical Review A*, vol. 65, no. 6, p. 062324, 2002.

[65] H.-K. Lo, M. Curty, and B. Qi, "Measurement-device-independent quantum key distribution," *Physical review letters*, vol. 108, no. 13, p. 130503, 2012.

[66] N. Gisin, S. Pironio, and N. Sangouard, "Proposal for implementing device-independent quantum key distribution based on a heralded qubit amplifier," *Physical review letters*, vol. 105, no. 7, p. 070501, 2010.

[67] E. Nagali, L. Sansoni, F. Sciarrino, F. De Martini, L. Marrucci, B. Piccirillo, E. Karimi, and E. Santamato, "Optimal quantum cloning of orbital angular momentum photon qubits through hong–ou–mandel coalescence," *Nature Photonics*, vol. 3, no. 12, p. 720, 2009.

[68] N. Sangouard, C. Simon, H. De Riedmatten, and N. Gisin, "Quantum repeaters based on atomic ensembles and linear optics," *Reviews of Modern Physics*, vol. 83, no. 1, p. 33, 2011.

[69] J. Hofmann, M. Krug, N. Ortegel, L. Gérard, M. Weber, W. Rosenfeld, and H. Weinfurter, "Heralded entanglement between widely separated atoms," *Science*, vol. 337, no. 6090, pp. 72–75, 2012.

[70] Z.-B. Chen, B. Zhao, Y.-A. Chen, J. Schmiedmayer, and J.-W. Pan, "Fault-tolerant quantum repeater with atomic ensembles and linear optics," *Physical Review A*, vol. 76, no. 2, p. 022329, 2007.

[71] M. Raymer, S. Van Enk, C. McKinstrie, and H. McGuinness, "Interference of two photons of different color," *Optics Communications*, vol. 283, no. 5, pp. 747–752, 2010.

[72] T. Kobayashi, R. Ikuta, S. Yasui, S. Miki, T. Yamashita, H. Terai, T. Yamamoto, M. Koashi, and N. Imoto, "Frequency-domain hong–ou–mandel interference," *Nature Photonics*, vol. 10, no. 7, pp. 441–444, 2016.

[73] C. Joshi, A. Farsi, and A. Gaeta, "Hong-ou-mandel interference in the frequency domain," in *CLEO: QELS_Fundamental Science*. Optical Society of America, 2017, pp. FF2E–3.

[74] S. E. Harris, "Nonlocal modulation of entangled photons," *Phys. Rev. A*, vol. 78, p. 021807, Aug 2008. [Online]. Available: https://link.aps.org/doi/10.1103/PhysRevA.78.021807

[75] J. Capmany and C. R. Fernández-Pousa, "Quantum model for electro-optical phase modulation," *JOSA B*, vol. 27, no. 6, pp. A119–A129, 2010.

[76] J. M. Lukens and P. Lougovski, "Frequency-encoded photonic qubits for scalable quantum information processing," *Optica*, vol. 4, no. 1, pp. 8–16, 2017.

[77] H.-H. Lu, J. M. Lukens, N. A. Peters, O. D. Odele, D. E. Leaird, A. M. Weiner, and P. Lougovski, "Electro-optic frequency beam splitters and tritters for high-fidelity photonic quantum information processing," *Physical Review Letters*, vol. 120, no. 3, p. 030502, 2018.

[78] L. J. Wright, M. Karpiński, C. Söller, and B. J. Smith, "Spectral shearing of quantum light pulses by electro-optic phase modulation," *Physical review letters*, vol. 118, no. 2, p. 023601, 2017.

[79] H.-H. Lu, J. M. Lukens, N. A. Peters, B. P. Williams, A. M. Weiner, and P. Lougovski, "Controllable two-photon interference with versatile quantum frequency processor," *arXiv preprint arXiv:1803.10712*, 2018.

[80] H.-H. Lu, J. M. Lukens, B. P. Williams, P. Imany, N. A. Peters, A. M. Weiner, and P. Lougovski, "A controlled-not gate for frequency-bin qubits," *arXiv preprint arXiv:1809.05072*, 2018.

[81] J. L. O'brien, "Optical quantum computing," *Science*, vol. 318, no. 5856, pp. 1567–1570, 2007.

[82] M. Fiorentino and F. N. Wong, "Deterministic controlled-not gate for single-photon two-qubit quantum logic," *Physical review letters*, vol. 93, no. 7, p. 070502, 2004.

[83] K. H. Kagalwala, G. Giuseppe, A. F. Abouraddy, and B. E. Saleh, "Single-photon three-qubit quantum logic using spatial light modulators," *Nature Communications*, vol. 8, no. 1, p. 739, 2017.

[84] N. J. Cerf, C. Adami, and P. G. Kwiat, "Optical simulation of quantum logic," *Physical Review A*, vol. 57, no. 3, p. R1477, 1998.

[85] G. K. Brennen, S. S. Bullock, and D. P. O'Leary, "Efficient circuits for exact-universal computations with qudits," *arXiv preprint quant-ph/0509161*, 2005.

[86] P. W. Shor, "Polynomial-time algorithms for prime factorization and discrete logarithms on a quantum computer," *SIAM review*, vol. 41, no. 2, pp. 303–332, 1999.

[87] M. H. Devoret and R. J. Schoelkopf, "Superconducting circuits for quantum information: an outlook," *Science*, vol. 339, no. 6124, pp. 1169–1174, 2013.

[88] J. I. Cirac and P. Zoller, "Quantum computations with cold trapped ions," *Physical review letters*, vol. 74, no. 20, p. 4091, 1995.

[89] A. Crespi, R. Ramponi, R. Osellame, L. Sansoni, I. Bongioanni, F. Sciarrino, G. Vallone, and P. Mataloni, "Integrated photonic quantum gates for polarization qubits," *Nature communications*, vol. 2, p. 566, 2011.

[90] P. C. Humphreys, B. J. Metcalf, J. B. Spring, M. Moore, X.-M. Jin, M. Barbieri, W. S. Kolthammer, and I. A. Walmsley, "Linear optical quantum computing in a single spatial mode," *Physical review letters*, vol. 111, no. 15, p. 150501, 2013.

[91] W.-T. Fang, Y.-H. Li, Z.-Y. Zhou, L.-X. Xu, G.-C. Guo, and B.-S. Shi, "On-chip generation of time-and wavelength-division multiplexed multiple time-bin entanglement," *Optics express*, vol. 26, no. 10, pp. 12 912–12 921, 2018.

[92] P. C. Humphreys, W. S. Kolthammer, J. Nunn, M. Barbieri, A. Datta, and I. A. Walmsley, "Continuous-variable quantum computing in optical time-frequency modes using quantum memories," *Physical review letters*, vol. 113, no. 13, p. 130502, 2014.

[93] P. Marin-Palomo, J. N. Kemal, M. Karpov, A. Kordts, J. Pfeifle, M. H. Pfeiffer, P. Trocha, S. Wolf, V. Brasch, M. H. Anderson *et al.*, "Microresonator-based solitons for massively parallel coherent optical communications," *Nature*, vol. 546, no. 7657, pp. 274–279, 2017.

[94] M. M. Wilde, *Quantum information theory*. Cambridge University Press, 2013.

[95] K. De Greve, P. L. McMahon, L. Yu, J. S. Pelc, C. Jones, C. M. Natarajan, N. Y. Kim, E. Abe, S. Maier, C. Schneider *et al.*, "Complete tomography of a high-fidelity solid-state entangled spin–photon qubit pair," *Nature communications*, vol. 4, 2013.

[96] R. Blume-Kohout, "Optimal, reliable estimation of quantum states," *New Journal of Physics*, vol. 12, no. 4, p. 043034, 2010.

[97] B. P. Williams and P. Lougovski, "Quantum state estimation when qubits are lost: a no-data-left-behind approach," *New Journal of Physics*, vol. 19, no. 4, p. 043003, 2017.

[98] R. A. Bertlmann and P. Krammer, "Bloch vectors for qudits," *Journal of Physics A: Mathematical and Theoretical*, vol. 41, no. 23, p. 235303, 2008.

[99] J. L. O'Brien, G. Pryde, A. Gilchrist, D. James, N. K. Langford, T. Ralph, and A. White, "Quantum process tomography of a controlled-not gate," *Physical review letters*, vol. 93, no. 8, p. 080502, 2004.

[100] M.-D. Choi, "Completely positive linear maps on complex matrices," *Linear algebra and its applications*, vol. 10, no. 3, pp. 285–290, 1975.

[101] X. Wang, B. C. Sanders, and D. W. Berry, "Entangling power and operator entanglement in qudit systems," *Physical Review A*, vol. 67, no. 4, p. 042323, 2003.

[102] T. G. Draper, S. A. Kutin, E. M. Rains, and K. M. Svore, "A logarithmic-depth quantum carry-lookahead adder," *arXiv preprint quant-ph/0406142*, 2004.

[103] J. Wang, H. Shen, L. Fan, R. Wu, B. Niu, L. T. Varghese, Y. Xuan, D. E. Leaird, X. Wang, F. Gan *et al.*, "Reconfigurable radio-frequency arbitrary waveforms synthesized in a silicon photonic chip," *Nature communications*, vol. 6, p. 5957, 2015.

[104] J. Wang, S. Paesani, Y. Ding, R. Santagati, P. Skrzypczyk, A. Salavrakos, J. Tura, R. Augusiak, L. Mančinska, D. Bacco *et al.*, "Multidimensional quantum entanglement with large-scale integrated optics," *Science*, p. eaar7053, 2018.

[105] T. Ikuta and H. Takesue, "Four-dimensional entanglement distribution over 100 km," *Scientific reports*, vol. 8, no. 1, p. 817, 2018.

[106] M. Malik, M. Erhard, M. Huber, M. Krenn, R. Fickler, and A. Zeilinger, "Multi-photon entanglement in high dimensions," *Nature Photonics*, vol. 10, no. 4, p. 248, 2016.

[107] M. Erhard, R. Fickler, M. Krenn, and A. Zeilinger, "Twisted photons: new quantum perspectives in high dimensions," *Light: Science & Applications*, vol. 7, no. 3, p. 17146, 2018.

[108] B. Hacker, S. Welte, G. Rempe, and S. Ritter, "A photon–photon quantum gate based on a single atom in an optical resonator," *Nature*, vol. 536, no. 7615, p. 193, 2016.

[109] M. A. Nielsen and I. Chuang, "Quantum computation and quantum information," 2002.

[110] D. Bouwmeester, J.-W. Pan, K. Mattle, M. Eibl, H. Weinfurter, and A. Zeilinger, "Experimental quantum teleportation," *Nature*, vol. 390, no. 6660, p. 575, 1997.

[111] D. Boschi, S. Branca, F. De Martini, L. Hardy, and S. Popescu, "Experimental realization of teleporting an unknown pure quantum state via dual classical and einstein-podolsky-rosen channels," *Physical Review Letters*, vol. 80, no. 6, p. 1121, 1998.

[112] J. G. Skellam, "The frequency distribution of the difference between two poisson variates belonging to different populations." *Journal of the Royal Statistical Society. Series A (General)*, vol. 109, no. Pt 3, pp. 296–296, 1946.

[113] G. Vidal and R. F. Werner, "Computable measure of entanglement," *Physical Review A*, vol. 65, no. 3, p. 032314, 2002.

[114] M. Reed and B. Simon, *IV: Analysis of Operators*. Elsevier, 1978, vol. 4.

APPENDICES

A. VISIBILITY WITH ACCIDENTALS SUBRTACTED

For a given CAR and accidentals level, we calculate the visibility of an interference pattern, based on the its maximum and minimum points for accidental-subtracted data. Since a gate-based detection scheme is used, we register the coincidence peak at zero delay between the two detectors as the coincidences plus accidentals, and the peak delayed by one period between the signal and idler gates as the accidentals (Fig. A.1a). We assume the second peak in Fig. A.1a to be the accidentals, and subtract that from the first peak to obtain the coincidences. When no coincidences are present (at the minimum of the interference pattern), if the subtraction of our experimental data is negative, we set the value to zero, as the number of coincidences have to be non-negative. This will result in the minimum to not have a zero average, and this average depends on the number of coincidences and accidentals. We assume a Poissonian distribution for both the coincidences and accidentals:

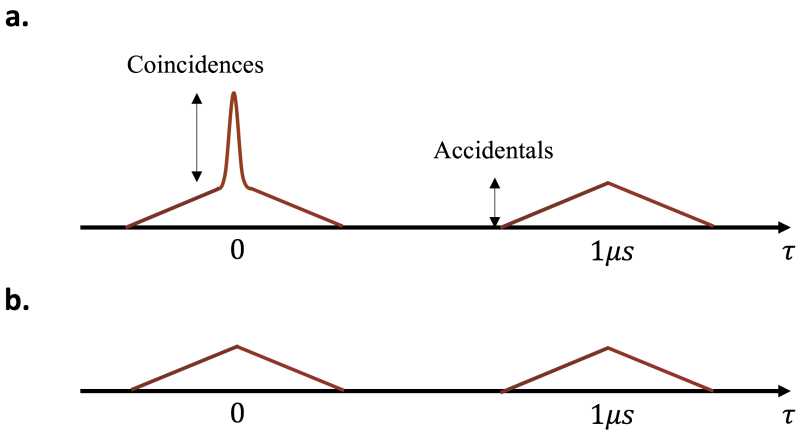

Fig. A.1. Gated detection scheme at a. maximum and b. minimum of the interference pattern. The gate repetition rate is assumed to be 1 MHz, so the accidentals triangles are 1 μs apart.

$$p\{k;\mu\} = \frac{\mu^k}{k!}e^{-\mu} \tag{A.1}$$

where $p\{k;\mu\}$ is the probability of registering k counts, if we have a mean of μ. In our accidental-subtracted scheme, we are subtracting two values with Poissonian distributions with means μ_1 and μ_2 from each other, resulting in a Skellam distribution [112]:

$$p\{k;\mu_1,\mu_2\} = e^{-(\mu_1+\mu_2)}\left(\frac{\mu_1}{\mu_2}\right)^{\frac{k}{2}} I_k(2\sqrt{\mu_1\mu_2}) \tag{A.2}$$

where $I_\alpha(x) = i^{-\alpha}J_\alpha(ix)$ is the modified Bessel function. The mean of the Skellam distribution is simply $(\mu_1 - \mu_2)$, which we assume is the case if we have the number of the coincidences mean much bigger than zero.

In the destructive interference case however, we are subtracting two Poissonian distributions with the same mean of μ. Since the result is supposed to give us coincidences, if the subtraction results ends up being negative, we replace it with zero. The mean of this distribution as a function of μ can be calculated using the moments of the distribution:

$$E(\mu) = \mu e^{-2\mu}[I_0(2\mu) + I_1(2\mu)] \tag{A.3}$$

This will be the mean of the minimum of the interference pattern, shown as a function of the mean of accidentals in Fig. A.2. If $\mu \gg 1$, $I_k(x)$ can be expressed as an exponential function independent of k, so Eq. A.3 can be estimated with:

$$\mu \gg 1 \rightarrow I_k(x) \simeq \frac{1}{2\pi x}e^x \rightarrow E(\mu \gg 1) = \sqrt{\frac{\mu}{\pi}} \tag{A.4}$$

We calculate the visibility of an interference pattern based on its maximum and minimum point:

$$V(C,\mu) = \frac{C_{max} - C_{min}}{C_{max} + C_{min}} = \frac{C - E(\mu)}{C + E(\mu)} \simeq \frac{C - \sqrt{\frac{\mu}{\pi}}}{C + \sqrt{\frac{\mu}{\pi}}} \tag{A.5}$$

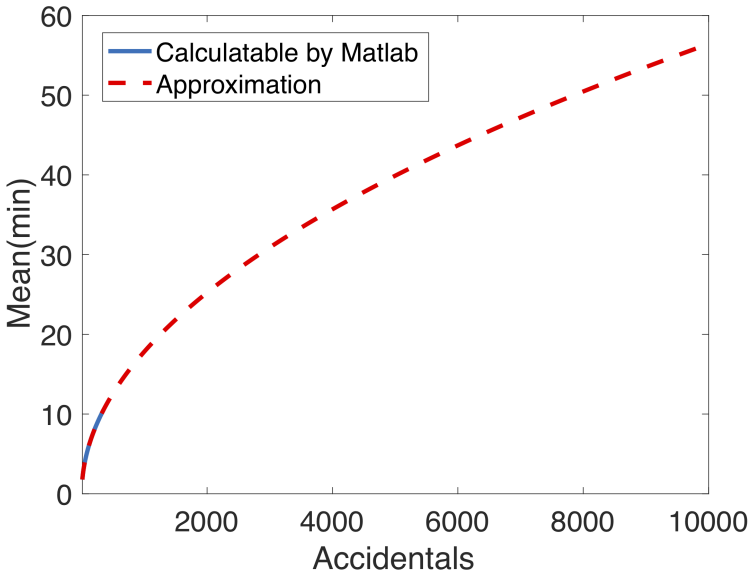

Fig. A.2. Mean of the subtraction of two Poissonian distributions with the same mean with negative values set to zero. As the mean grows, MATLAB cannot calculate the exact mean, therefore, the mean is calculated using Eq. A.4 for large means.

where C is the maximum of the interference pattern, which is the maximum number of coincidences. Eq. A.6 can also be written as a function of CAR and mean of accidentals:

$$CAR = \frac{C}{\mu} \rightarrow V(CAR, \mu) = \frac{\sqrt{\pi\mu}CAR - 1}{\sqrt{\pi\mu}CAR + 1} \tag{A.6}$$

which is shown in Fig. A.3.

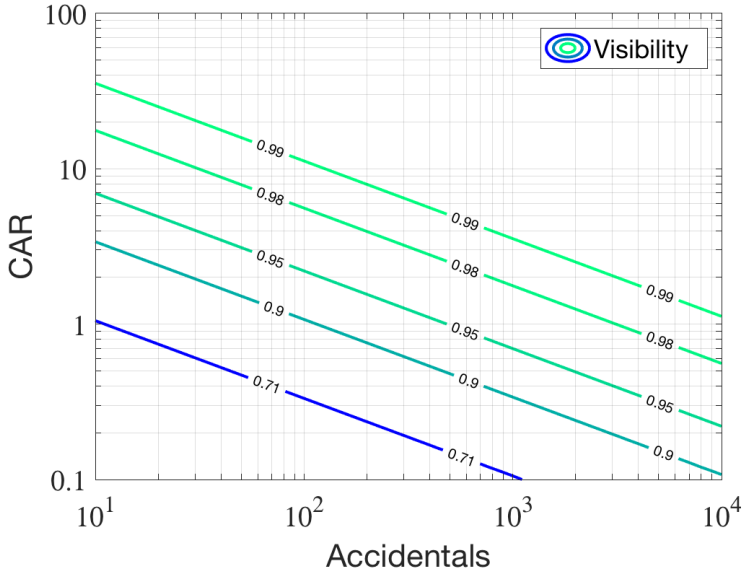

Fig. A.3. Visibility as a function of CAR and mean of accidentals.

B. SEPARABILITY OF DENSITY MATRICES

We explain the Peres-Horodocki criterion [48, 49] to calculate the negativity of a density matrix [113], which is a measure of whether it is separable into two density matrices or not. A quantum system consisting two separable systems is separable if its density matrix can be written as:

$$\rho = \Sigma_A w_A \rho'_A \otimes \rho''_A \tag{B.1}$$

where ρ'_A and ρ''_A are density matrices of the two subsystems, and the positive weights w_A satisfy $\Sigma_A w_A = 1$. If ρ is not separable, some of the w_A values are negative [48,49]. This was used by Vidal and Werner [113] to calculate a measurement of entanglement based on the density matrix of the system. The trace norm of any Hermitian operator A is $\|A\|_1 = \sqrt{A^T A}$ [114], which is equal to the sum of the absolute values of eigenvalues of A. For density matrices, all eigenvalues are positive and therefore, $\|\rho\|_1 = Tr(\rho) = 1$ [113]. The partial transpose of ρ, ρ^{T_A}, also satisfies $Tr(\rho^{T_A}) = 1$, but if ρ is not separable, ρ^{T_A} will also have negative eigenvalues, therefore, the sum of these negative eigenvalues can be used as a measurement of separability called negativity and is related to the trace norm of ρ^{T_A}:

$$\mathcal{N}(\rho^{T_A}) = \frac{\|\rho^{T_A}\|_1 - 1}{2} \tag{B.2}$$

If $\mathcal{N}(\rho^{T_A}) > 0$ is a witness of inseparability or entanglement.

C. BAYESIAN ESTIMATION

We have an N-outcome experiment and perform C_Σ trials resulting in one of the N outcomes each time, i.e., obtain C_Σ total counts, where each outcome n is observed C_n times:

$$C_\Sigma = \Sigma_{n=0}^{N-1} C_n \tag{C.1}$$

Let $\mathcal{D} = \{C_0, C_1, ..., C_{N-1}\}$ be shorthand for the set of all results–it is the experimental "data" underlying probabilities for each outcome. In this simple model, we let $a = \{p_0, p_1, ..., p_{N-1}\}$ be the set of all probabilities, so that our data should have occurred with probabilities:

$$\mathcal{P}(\mathcal{D}|a) = \frac{C_\Sigma!}{C_0!C_1!...C_{N-1}!} p_0^{C_0} p_1^{C_1} ... p_{N-1}^{C_{N-1}} \tag{C.2}$$

This likelihood $\mathcal{P}(\mathcal{D}|a)$ is the basis for both maximum likelihood estimation (MLE) and Bayesian mean estimation (BME). In our case, we use the BME approach [97], since the MLE does not calculate the uncertainty of the estimated values. In the BME approach, we supplement the likelihood $\mathcal{P}(\mathcal{D}|a)$ with a prior distribution $q(a)$, a probability density over probability sets $a = \{p_0, p_1, ..., p_{N-1}\}$. With this, we form the posterior distribution of a given that we now have data $\mathcal{D}$. From Bayes' theorem [97]:

$$\mathcal{P}(a|\mathcal{D}) = \frac{\mathcal{P}(\mathcal{D}|a)q(a)}{\mathcal{P}(\mathcal{D})} = \frac{\mathcal{P}(a|\mathcal{D})q(a)}{\int da' \mathcal{P}(\mathcal{D}|a')q(a')} \tag{C.3}$$

In most cases, one chooses an uninformative prior which treats all or most distributions as equally likely. It often makes sense to choose the fully uniform prior:

$$q(a) = \begin{cases} 1 & ; \forall a = \{p_0, p_1, ..., p_{N-1}\}\ s.t.\ p_n \geq 0,\ \Sigma_n p_n = 1 \\ 0 & ; otherwise \end{cases} \tag{C.4}$$

Let us apply this to our case:

$$\int da' \mathcal{P}(\mathcal{D}|a') q(a') = K \int_0^1 dp_0 \int_0^{1-p_0} dp_1 ... \int_0^{1-p_0-p_1-...-p_{n-3}} dp_{N-2} \times p_0^{C_0} p_1^{C_1} ... p_{N-2}^{C_{N-2}} \left(1 - \Sigma_{n=0}^{N-2} p_n\right)^{C_{N-1}} \tag{C.5}$$

where K is the factorial coefficients. To calculate this integral, a known method is used, where Eq. C.5 can be written using a delta function:

$$K \int_0^\infty dp_0 \int_0^\infty dp_1 ... \int_0^\infty dp_{N-2} \int_0^\infty dp_{N-1} \times p_0^{C_0} p_1^{C_1} ... p_{N-2}^{C_{N-2}} p_{N-1}^{C_{N-1}} \delta\left(1 - \sum_{n=0}^{N-1} p_n\right) \tag{C.6}$$

The delta function can be written in an integral form:

$$\delta(x) = \frac{1}{2\pi} \int_{-\infty}^{\infty} e^{-ikx} dk \tag{C.7}$$

Using this in Eq. C.6 gives us:

$$\frac{1}{2\pi} K \int_{-\infty}^{\infty} dk e^{-ik} \int_0^\infty dp_0 p_0^{C_0} e^{ikp_0} \int_0^\infty dp_1 p_1^{C_1} e^{ikp_1} ... \int_0^\infty dp_{N-1} p_{N-1}^{C_{N-1}} e^{ikp_{N-1}} \tag{C.8}$$

Using the definition of Gamma function $\Gamma(z) = \int_0^\infty x^{z-1} e^{-x} dx$ and using the substitution $\kappa = -ik$, Eq. C.8 will be:

$$\begin{aligned} &\frac{1}{2\pi i} K \int_{-i\infty}^{i\infty} d\kappa e^{\kappa} \frac{\Gamma(C_0+1)}{\kappa^{C_0+1}} \frac{\Gamma(C_1+1)}{\kappa^{C_1+1}} ... \frac{\Gamma(C_{N-1}+1)}{\kappa^{C_{N-1}+1}} \\ =&\frac{1}{2\pi i} K \times \Gamma(C_0+1)\Gamma(C_1+1)...\Gamma(C_{N-1}+1) \int_{-i\infty}^{i\infty} \frac{d\kappa e^{\kappa}}{\kappa^{C_\Sigma+N}} \end{aligned} \tag{C.9}$$

Using the Laplace transform, the integral can be calculated as $\frac{2\pi i}{\Gamma(C_\Sigma+N)}$, therefore, Eq. C.5 can be written as:

$$\int da' \mathcal{P}(\mathcal{D}|a') q(a') = K \frac{\Gamma(1+C_0)\Gamma(1+C_1)...\Gamma(1+C_{N-1})}{\Gamma(C_\Sigma+N)} \tag{C.10}$$

Therefore, Eq. C.3 will be:

$$\mathcal{P}(a|\mathcal{D}) = \frac{\Gamma(N+C_\Sigma)}{\Gamma(1+C_0)\Gamma(1+C_1)...\Gamma(1+C_{N-1})} p_0^{C_0} p_1^{C_1} ... p_{N-2}^{C_{N-2}} \left(1 - \Sigma_{j=0}^{N-2} p_j\right)^{C_{N-1}} \tag{C.11}$$

From this distribution, one can calculate the expectation and variance of any quantity that is a function of a. In particular, note that the moments of any probability p_n are:

$$\begin{aligned}\langle p_n^k \rangle &= \frac{\Gamma(N+C_\Sigma)}{\Gamma(1+C_0)\Gamma(1+C_1)...\Gamma(1+C_{N-1})} \int_0^1 dp_0 \int_0^{1-p_0} dp_1 ... \int_0^{1-p_0-p_1-...-p_{n-3}} dp_{N-2} \\ &\quad \times p_0^{C_0} p_1^{C_1} ... p_n^{C_n+k} ... p_{N-2}^{C_{N-2}} \left(1 - \Sigma_{j=0}^{N-2} p_j\right)^{C_{N-1}} \\ &= \frac{\Gamma(1+C_n+k)}{\Gamma(1+C_n)} \frac{\Gamma(N+C_\Sigma)}{\Gamma(N+C_\Sigma+k)} = \frac{(C_n+k)!}{C_n!} \frac{(N+C_\Sigma-1)!}{(N+C_\Sigma+k-1)!}\end{aligned} \tag{C.12}$$

From Eq. C.12, the mean and variance of p_n can be calculated by deriving the equation for $k = 1$ and $k = 2$:

$$\begin{aligned} k = 1: &\qquad \langle p_n \rangle = \frac{1+C_n}{N+C_\Sigma} \\ k = 2: &\qquad \langle p_n^2 \rangle = \frac{(1+C_n)(2+C_n)}{(N+C_\Sigma)(1+N+C_\Sigma)} \end{aligned} \tag{C.13}$$

Thus, we can estimate:

$$\tilde{p}_n = \frac{1+C_n}{N+C_\Sigma(1+N+C_\Sigma)} \tag{C.14}$$

and:

$$\Delta\tilde{p}_n = \sqrt{\frac{1+C_n}{(N+C_\Sigma)^2} \frac{N+C_\Sigma-C_n-1}{N+C_\Sigma+1}} \tag{C.15}$$